Imperial College of London
Department of Aeronautics

Design of Compliant Structures for Aerial-Aquatic Robots

Crystal Winston

Submitted in part fulfilment of the requirements for the degree of
Master of Philosophy
September 2021

Copyright Statement

Statement of Originality

The work presented hereafter is based on research carried out by the author at the Department of Aeronautics at Imperial College London and it is all the author's own work except where otherwise acknowledged. No part of the present work has been submitted elsewhere for another degree or qualification.

Crystal Winston

Acknowledgements

I would like to express my sincere gratitude to my supervisor, Prof. Mirko Kovac, for his support, guidance throughout this research project.

I would like to acknowledge the funding from the Marshall Scholarship for supporting my research and the several professional and personal development seminars received during my MPhil.

A particular thanks to some of the technical staff of the Department of Aeronautics: Roland, Ian, Jordan, Mark, Joseph, and Keith, who have greatly contributed with their expertise in manufacturing, wind tunnel, and instron testing to the work discussed in this thesis.

Finally, I would like to thank my closest collaborators: Raphael Zufferey, Sophie Armanini, Andre Farinha, Fabian Wiesemüller, Julien Di Tria, and Diego Debruyn.

Dedication

To my parents Mary and Chris Winston.

Abstract

Currently, tasks like water quality sampling and underwater surveying utilize copious amounts of manual labor because they either require people to deploy aquatic sensors or coordinate actions between aerial and aquatic devices. However, the development of an aerial-aquatic robot that can fly to an aquatic location, collect data, and then fly back to land could dramatically reduce the need for such costly and potentially dangerous manual labor. Unfortunately, most aerial-aquatic robots that have been developed thus far us inefficient aquatic propulsion systems that limit mission times or are unable to successfully demonstrate a full mission cycle. For this reason, improving aerial-aquatic locomotion is still an area of active research. Most aerial-aquatic robots have been inspired by nature, as there are several animals that perform aerial-aquatic maneuvers. However, current robots are limited in how well they can emulate these animals because animals have naturally soft bodies, but their robotic counterparts are made from stiff materials and structures. The focus of my research is the design and modeling of lightweight flexible structures that will ultimately enable aerial-aquatic robots to better mimic the locomotion strategies we observe in nature. Both honeycomb and kirigami structures present a promising solution to this problem as they can be used to dramatically reduce the stiffness of a stiff and lightweight material. Here, I present two projects which demonstrate how both honeycomb and kirigami structures can be used for lightweight, flexible components of aerial-aquatic robots. Both projects present work towards the development of a camber morphing airfoil which can be used for aerial locomotion by allowing for more efficient flight and aquatic motion, by acting as a morphing sail that allows the vehicle to travel at the water's surface. Both of these serve as bio-inspired locomotion strategies, as wing morphing has been observed in many birds, and camber morphing sails have been observed in Portuguese Man-o-War jellyfish. I start by deriving 1D analytical models for honeycomb and kirigami structures and then demonstrate how those structures can be used as flexible aerial-aquatic robot building blocks in a self-sensing structure intended for a camber morphing wing. I then develop 3D models for diamond celled honeycombs and then use those models to design a shape-locking camber morphing wing. Ultimately, this research demonstrates how both honeycomb and kirigami structures can be used to build flexible components of aerial-aquatic robots that enable bio-inspired designs which more accurately imitate nature.

Contents

Acknowledgements **v**

Abstract **ix**

List of tables **xv**

List of figures **xxi**

Glossary **xxiii**

Acronyms **xxvii**

1 Introduction **1**

1.1 Motivation and Objectives 1

1.1.1 Thesis statement 1

1.1.2 Motivation for Developing Aerial-Aquatic Robots 1

1.1.3 Current Challenges and Work Towards Bio-Inspired Solutions 2

1.1.4 Motivation for Developing Flexible Structures for Aerial-Aquatic Robots . . 4

1.1.5 Research Objectives 5

1.2 Contributions 6

2 Background **8**

2.1 Motivation for Camber Morphing Wings in Aerial-Aquatic Robots 8

2.2 Honeycomb and Kirigami Structures For Flexible Robots 9

2.2.1 Flexible Honeycomb and Horizontal Slit Kirigami Structures in Robotics . . 10

2.2.2 Mechanics of Honeycomb Structures 11

2.3 Methods of Controlled Stiffening: Laminar and Particle Jamming 12

3 1D Modeling of Honeycomb and Kirigami Structures **14**

3.1 Motivation and Contributions 14

3.2 Diamond Celled Honeycomb vs. Horizontal Slit Kirigami 15

3.3 Mechanical Modeling 18

3.3.1 Diamond Celled Honeycomb Homogenization 18

3.3.2 Extension of Diamond Celled Honeycomb Homogenization 21

3.3.3 Horizontal Slit Kirigami Homogenization 22

3.3.4 Unified Model 23

3.4 Results and Discussion 24

3.5 Kirigami vs Honeycomb Comparison 26

3.5.1 Conclusion 28

3.5.2 Future Work 28

4 Shape-locking, Bidirectional, Bending, Structures with Diamond Celled Honeycombs **29**

4.1 Introduction 29

4.2 Design, Analysis, and Manufacturing 30

4.2.1 Structure Geometry and Components 31

4.2.2 3D Diamond Cell Honeycomb Homogenization 34

4.2.3 Laminar Jamming Modeling 38
4.2.4 Static Composite Model 38
4.2.5 Dynamic Modeling and Control 44
4.2.6 Manufacturing 46
4.3 Results and Discussion 47
4.3.1 Validation of Mechanical Model 47
4.3.2 Wind Tunnel Testing 48
4.3.3 Use of Shape Locking Bidirectional Bending Structures for Hydrofoils . . . 50
4.4 Conclusion 54
4.4.1 Future Work 55

5 Conclusion **56**
5.1 Summary of Achievements 56
5.2 Applications 56
5.3 Future Work 57

Bibliography **57**

A Hyperelastic Materials in Aerial-Aquatic Robots **69**
A.1 Motivation and Contributions 69
A.2 Hyperelastic Materials in Soft Robotics 70
A.2.1 A Review of Hyperelastic Materials In Soft Robotic Actuators 70
A.3 Hyperelastic Actuators for Aerial-Aquatic Morphing Wings 72
A.3.1 Constraint Enclosed Morphing Wing 73
A.3.2 Constraint Embedded Morphing Wing 75
A.3.3 Conclusion 77

A.4 MEDUSA: A Demonstration of Hyperelastic Materials in Aerial-Aquatic Robots . . 78

A.4.1 Modeling of Hyperelastic Membrane 79

A.4.2 Results and Discussion 81

A.4.3 Conclusion 81

B Permission to Reproduce Content **83**

B.1 Permission to Reproduce Content from Robotics and Automation Letters 83

B.2 Permission to Reproduce Content from Nature Communications 84

List of Tables

1.1 Summary of Contributions 7

3.1 Mechanical properties of the investigated MFC specimens. 24

4.1 Morphing Wing Properties 33

4.2 Analytical and FEM model stiffnesses 41

4.3 SLBBS Properties 44

4.4 Bending test data from Instron experiments. **a)** bending test conducted under no vacuum with no latex skin. **b)** bending test conducted under no vacuum with latex skin. **c)** bending test conducted under 60KPa vacuum pressure with no latex. 49

A.1 Model parameter values. 81

List of Figures

2.1 An illustration demonstrating the use cases for a camber morphing wing in both aerial and aerial-aquatic locomotion. Such a wing could be used for aerial locomotion, by allowing the vehicle to both fly efficiently and control it's orientation. It can also be used for aquatic locomotion, as a morphing sail, allowing an aerial-aquatic vehicle to move on the water's surface. 10

3.1 **a)** Confocal image of a hydro-actuated seed capsule of an ice seed plant in an opened state taken from [49] ©2021 Springer Nature. **b)** Macro-image of the manufactured compliant cellulose honeycomb structure taken from [37] ©2021 IEEE. **c)** Confocal image of a hydro-actuated seed capsule of an ice seed plant in a closed state taken from [49] ©2021 Springer Nature. **d)** Macro-image of the manufactured compliant cellulose horizontal slit kirigami structure. 16

3.2 Comparison of stiffness between kirigami and a diamond celled honeycomb under a 200 g tensile load. Left column showing the structure unloaded, right column showing the structure loaded taken from [37] ©2021 IEEE. **a)** Kirigami structure with a total displacement of 11 mm. **b)** Honeycomb structure (θ = 15.0 °) with a total displacement of 2 mm. 17

3.3 Loading condition and geometric constants for derivation of (Eq. (3.4)) taken from [37] ©2021 IEEE. **a)** a single cell loaded with far field stress σ_∞. **b)** Free body diagram of a single cell wall. 19

3.4 FEM simulation mesh and comparison of FEM results with (Eq. (3.4)). **a)** FEM simulation mesh. Each cell wall is modeled with shell elements and has 20 elements along its length and 10 along its depth. **b)** Plot showing both the stiffness ratios of the honeycomb model described in (Eq. (3.4)) and the FEM simulations. 20

3.5 FEM used to extend preliminary model and geometry that corresponds to that model. **a)** FEM simulation run in Fusion 360 using a dense 3D element adaptive mesh refinement that converged on a value of maximum displacement after three iterations. The blue regions represent regions with the lowest amounts of stress while the green/yellow represent regions with the highest amounts of stress. **b)** Geometry corresponding to (Eq. (3.5)) taken from [37] ©2021 IEEE. The black lines represent the diamond with lines of length l, the gray represents the actual structure with thickness t, where the darker gray sections are where the cell walls overlap. The dashed red line is the midline of the beam of length Λ. 21

3.6 Loading condition and geometric constants for derivation of (Eq. (3.6)) taken from [37] ©2021 IEEE. **a)** a single cell loaded with far field stress σ_∞. **b)** Free body diagram of a single cell wall. 23

3.7 Plot of the ratios determined using FEM on honeycomb structures with various angles of θ, the actual measured ratios and their 95% confidence intervals, which are denoted as uncertainties, the initial honeycomb model shown in (3.4), the modified honeycomb model shown in Eq. (3.5), and the unified model shown in (3.7) taken from [37] ©2021 IEEE. 25

3.8 The measured bridge voltage during step-wise and cyclic loading and unloading taken from [37] ©2021 IEEE. **a)** Bridge voltage response during ten cycles. **b)** Bridge voltage response and applied displacement. **c)** Bridge voltage response during step wise increase of applied displacement. **d)** Bridge voltage response during step wise decrease of applied displacement. 26

3.9 Plots showing values for Ms for diamond celled honeycombs and horizontal slit kirigami structures. The axes for θ and t/l are linear while the axes for the Ms are on a log scale.**a)** Values of $M_{uniaxial}$ for different values of θ and t/l. **b)**Values of $M_{bending}$ for different values of θ and t/l. 27

4.1 SLBBS design methodology. The blue and gray blocks outline the three high-level design phases. The black titles within the yellow boxes outline the sub-steps of those high-level design phases. The red text explains how the SLBBS used in the morphing wing described in this chapter was designed, built, and tested using this methodology. 31

4.2 SLBBS component diagram. 32

4.3 Camber morphing component diagram. The portions of the SLBBS are labeled in green. The remaining parts of the wing are labeled in black. 33

4.4 Modified version of Fig. 3.3. Here the diamond-cell is outlined in black, with beams of length Λ superimposed on top of that in red adapted from [37] ©2021 IEEE. The far field stress σ_∞ is now replaced with σ_2 per the coordinate system also shown in the figure. **a)** Loading condition. **b)** A single cell wall of length Λ under internal loads caused by far field stress σ_2. 35

4.5 Laminar jamming working principle 39

4.6 Composite model geometry, loading condition, and coordinate system. **a)** labeled geometry. **b)** loading condition and coordinate system. 40

4.7 Mesh used for FEM model of SLBBS structure. The diamond celled honeycombs were modeled with Standard hex elements of quadratic order. That mesh had 301 elements along the the SLBBS dimension L and 18 elements along W and 10 elements along $t(x_3)$. The laminar jamming layer was modeled with shell elements. It was a midsurface with thickness $0.512\,mm$ that has 101 elements along it L and 172 elements along W. 42

4.8 plate theory model plot with fem 42

4.9 A predicted airfoil shape under a distributed load of $2N$ with no laminar jamming vacuum and a corresponding deflection of $4.5\,mm$. 43

4.10 System identification example plot. 45

4.11 Instron test experimental setup design. **a)** Instron test setup schematic. The load P is applied by the Instron machine. An isotropic image of the setup is in the upper left corner. **b)** Photo of the actual SLBBS being tested in the Instron. 48

4.12 Instron test data compared to analytical and FEM models 49

4.13 Wind tunnel experiment setup diagram. **a)** Wind tunnel setup schematic. The image in the upper right corner is an isotropic view of the entire setup. **b)** Photo of the actual wing being tested in the wind tunnel. 50

4.14 Morphing wing performance plots. **a)** Lift coefficient vs. AoA. **b)** Drag coefficient vs. AoA. **c)** Aerodynamic Efficiency (Lift/Drag coefficients vs. AoA). 51

4.15 Computational Fluid Dynamics (CFD) run for a NACA 0009 airfoil traveling at $7\,m/s$ in both air and water showing the fluid pressure around the wing. The values for pressure reported are relative to atmospheric pressure. **a)** CFD in air. The dashed red lines represent the beginning and end of the SLBBS. The relative pressures range from 30 Pa to -22 Pa. **b)** CFD in water. The dashed red lines represent the beginning and end of the SLBBS. The relative pressures range from 22 kPa to -19 kPa.The dashed red lines represent the beginning and end of the SLBBS. **c)** a duplicate of the study shown in b with a new suggested region for the SLBBS denoted with yellow dashed lines. 53

A.1 constraint enclosed actuator based morphing wing concept. 74

A.2 Cut-out pattern for a knit textile bending actuator based morphing wing. The black lines are the pattern cut from the TPU sheet. The red lines delineate seams created by a heat gun which separate the airfoil shape from the tabs that are bonded together to form the seams.The blue line is a folded seam. 75

A.3 constraint embedded actuator based morphing wing concept. **a)** 3/4 and side views of the entire wing. **b)** A cross-section of the wing with labeled sections 76

A.4 Schematic of the operation principle of the dual system adapted from [80]. **A.** The quadrotor carries the submersible pod (yellow) to an aquatic location. **B1.** The quadrotor lands and floats on the water's surface. **B2.** The coiling mechanism (blue) releases a tether and the submersible pod moves vertically, through buoyancy control, and horizontally, using its jets, to reach the target underwater location. Live video is transmitted. A real image of the robot in this state is boxed in red. **C.** The tether is coiled again and the drone flies back to the user. 79

A.5 Membrane volume versus pressure: model-predicted and tracking data-reconstructed results taken from [80] ©2020 IEEE. 82

Glossary

* Honeycomb or kirigami material property. If accompanied by $_k$ it refers to a kirigami material property. If accompanied by a $_h$ or a subscript with a sequence of numbers it refers to a honeycomb material property. If there is no subscript, then it is a general term referring to both honeycomb and kirigami structures. xxiv, 12, 23, 24

$_h$ Honeycomb material property. xxiii, 19, 22

$_k$ Kirigami material property. xxiii, 22

$_s$ Material property for the solid material from which a honeycomb or kirigami structure is made. xxiv, 19, 21, 22, 23, 24, 36, 37, 38, 44

$_l$ Property for the material used in the laminar jamming layer. 38, 44

$_{lj}$ Laminar jamming layer material property. 38, 41

$_t$ Transverse. 80

$_n$ Normal. 80

Re Reynolds Number. The ratio of inertial forces and viscous forces. 3, 49, 50, 52

free variable An aspect of a structure's design (i.e. a length, width, material property, etc.) which is within the control of the designer. 26

constraint enclosed actuator A soft robotic actuator consisting of an elastomeric body that is then covered in some form of mesh or textile. That mesh or textile acts as a constraint which forces the actuator to take on a specific shape. xx, 70, 71, 73, 74, 77

knit textile bending actuator A soft robotic actuator made from two components: an inflatable elastic bladder and a fabric sheath. The sheath consists of two different textiles: one isotropic woven textile and another anisotropic knit textile. In its most compliant direction, the knit textile is far less stiff than the woven textile. The two textiles are stitched together in such a way that they are on opposite sides of the sheath. When the bladder is inflated, the actuator bends towards the woven textile side, as the knit textile stretches more under the same applied pressure due to its lower stiffness. xx, 71, 73, 75, 77, 81

constraint embedded actuator A soft robotic actuator made from a molded elastomeric body. These actuators have some form of constraining material or structure embedded within them that forces them to take on a specific shape when actuated. xxi, 70, 71, 72, 73, 75, 76, 77, 78

diamond celled honeycomb A honeycomb structure where each cell is in the shape of a diamond. Refer to 3.1 for an image of this. xvii, xix, xxv, 6, 11, 14, 15, 16, 17, 18, 19, 20, 22, 23, 24, 25, 27, 28, 29, 30, 31, 39, 41, 42, 44, 46, 54, 56, 57

horizontal slit kirigami structure A compliant kirigami structure made from cutting a pattern of horizontal slits into a sheet of material. Refer to 3.1 for an image of this. xvii, xix, 6, 11, 12, 14, 15, 16, 18, 20, 22, 27, 28, 29, 56, 57

λ Stretch Ratio. New length over initial length. 80

E Young's Modulus. xxiv, 12, 18, 19, 21, 22, 23, 24, 34, 35, 36, 37, 38, 41, 44

G Shear Modulus. 12, 34, 37, 38

$\bar{E}$ $\frac{E^*}{E_s}$. 19, 21, 22, 23, 24, 27

$\bar{\rho}$ ratio of the honeycomb or kirigami density over the density of the bulk material. ($\frac{\rho^*}{\rho_s}$). 17, 22, 27, 37

l Honeycomb or Kirigami cell-wall length. xviii, xix, 18, 19, 21, 22, 23, 27, 37, 38, 44

t Honeycomb or Kirigami cell-wall thickness. xviii, xix, xxv, 19, 21, 22, 23, 27, 36, 37, 38, 44

Λ Length of the beam that deforms within a diamond-celled honeycomb cell-wall. xviii, xix, 21, 23, 35, 36

b Honeycomb or Kirigami cell-wall depth. xxv, 18, 19, 22

I beam area moment of inertia. $\frac{bt^3}{12}$. 19, 22

T Internal stress. 80

C_1 Material Constant used in Mooney-Rivlin constitutive relation. xxv, 80, 81

C_2 Material Constant used in Mooney-Rivlin constitutive relation. This constant is different from C_1. xxv

α Material Constant used in Mooney-Rivlin constitutive relation. C_1/C_2. 80, 81

h membrane height. 80, 81

a half of the membrane base width. 81

V membrane volume. 81

θ Half of the angle between two cell walls in a diamond celled honeycomb. xvii, xix, 16, 17, 18, 19, 20, 21, 22, 23, 24, 25, 27, 35, 36, 37, 38, 44

P A force applied to a single cell wall as a result of far-field stress σ_∞. 18, 19, 22, 35, 80

σ_∞ Far-field stress. xvii, xviii, xix, xxv, 18, 19, 22, 23, 35

M Material selection index. xix, 26, 27

ε True strain. 19, 22, 34, 36

δ Cell wall beam deflection. 19, 22, 35, 36

ν Poisson's Ratio. 12, 34, 35, 36, 37

σ True stress. xix, 34, 35

n Number of sheets of laminar jamming material. 36, 38, 44

$\mathbb{C}$ Material compliance matrix. 34, 35, 41

$\mathbb{S}$ Material stiffness matrix. 34, 35

W SLBBS width. 37, 44

L SLBBS length. 37, 44

K curvature. 80

ρ material or composite density. 44

$\mathcal{K}$ cantilever bending stiffness. 44, 45

Acronyms

uC micro-controller. 47

AoA Angle of Attack. xx, 49, 50, 51, 55, 72

CFD Computational Fluid Dynamics. xx, 52, 53

FEA Fluidic Elastomer Actuator (not to be confused with Finite Element Analysis, which will instead be referred to as FEM). 71, 72, 75, 76, 77, 81, 82

FEM Finite Element Methods. xv, xviii, xix, xx, xxvii, 6, 7, 11, 15, 18, 20, 21, 30, 39, 40, 41, 42, 48, 49, 54, 56

MAV Micro Aerial Vehicle. 2, 3, 4, 28, 32, 50, 55, 57, 72, 77

MEDUSA a Multi-Environment Dual-robot for Underwater Sample Acquisition. 70, 78, 79, 82

MFC Microfibrillated Cellulose. 14, 23, 24, 25, 26, 28

ODE Ordinary Differential Equation. 41, 43, 80

PID Proportional Integral Derivative Control. 45, 47

PMW Portuguese Man-O-War Jellyfish. 72, 73

PTFE Polytetrafluoroethylene. 46, 74

RMSE root mean square error. 25

SLBBS Shape-locking Bi-directional Bending Structure(s). xv, xix, xx, xxvi, 6, 7, 29, 30, 31, 32, 33, 38, 39, 41, 42, 43, 44, 45, 46, 47, 48, 50, 52, 53, 54, 55, 56, 57

SMA Shape Memory Alloy. 70, 72

TPU Thermoplastic polyurethane. A hyperelastic thermoplastic that is used in vacuum bags and flexible 3D printer filament. xx, 74, 75, 78

XFOIL A command-line based program for subsonic airfoil analysis. 41, 43

Chapter 1

Introduction

1.1 Motivation and Objectives

1.1.1 Thesis statement

The focus of my research is design and modeling of honeycomb and kirigami based structures for camber morphing wings used in aerial-aquatic robots. Throughout the thesis, I present models for these structures and then use those models to design, build, and test components of camber-morphing airfoils that can be used for both sailing and efficient flight. In the subsequent sections, I motivate my work by explaining what aerial-aquatic robots are used for and why design of flexible structures for these robots is a relevant area of research. I then summarize the details of the work covered in the rest of the thesis and highlight the scientific and technical contributions.

1.1.2 Motivation for Developing Aerial-Aquatic Robots

With current technology, tasks like water sampling and underwater surveying require lots of manual labor because they require people to either deploy aquatic sensors or coordinate actions between a team of aerial and aquatic devices [1]. Development of a single robot for such tasks could allow them to eventually be completed autonomously which would lead to more efficient data collection, improved safety, and reduced costs. For these reasons, development of aerial-aquatic robots has

become a new and exciting area of research. Aerial-Aquatic robots are robots that can travel through air and water as well as transition between the two media. This makes it possible for a single robot to travel long distances and fly over obstacles, like an aerial robot, and move underwater or at the water's surface for long periods of time, like an aquatic robot. By combining the capabilities of both and aerial and aquatic robots, a single system can fly to a remote aquatic location, collect a water sample or survey an aquatic environment, and then fly back to a land-based location.

1.1.3 Current Challenges and Work Towards Bio-Inspired Solutions

Many of aerial-aquatic robots are quadrotors that operate in both media. These systems typically fly to an aquatic location, sink beneath the water's surface, use their propellers to move through the water, rise to the water's surface using some form of buoyancy control, and then transition back to flight once the propellers have left the water [2–4]. While these systems have demonstrated the ability to travel to and from an aquatic location as well as travel beneath the water's surface, they do so using the same propulsion system for both aerial and aquatic locomotion. This makes them efficient in flight, but inefficient underwater, leading to time-limited and short-range missions that can only last on the order of minutes [1].

Consequently, several researchers have started developing robots that use propulsion systems intended to operate efficiently in both media. A few examples of these include the RoboBee, AquaMAV, Aquatic Jump-Glider, and SailMAV. All of these robots demonstrate significant strides towards efficient aerial-aquatic locomotion but are currently incapable of performing a full mission. The RoboBee is an insect-scale robot that breaks the water's surface and flies by flapping its wings. However, while this system has demonstrated successful aquatic escape, it has yet to complete a controlled flight and also relies on an external power source that it cannot carry[5]. The AquaMAV is a fixed wing robot capable of escaping the water through the release of high-pressure CO_2 [6]. Ultimately, this robot is intended to fly to an aquatic location, plunge dive into the water, collect a sample, escape the water, and then deliver the sample to a land-based location. Currently, this system has demonstrated aquatic escape and plunge diving capabilities, but it has yet to fly to and from a remote aquatic location or demonstrate a full mission cycle in a single system. This system can also only perform a single dive and aquatic exit, which greatly limits the kinds of missions it can be used for. Following the develop-

ment of the AquaMAV, was the Aquatic Jump-Glider, a fixed-wing vehicle that uses water-reactive fuel to perform several successive jumps into and out of the water [7]. While this robot is capable of performing multiple successive aquatic jumps, and therefore collecting multiple samples or data from different locations. It also cannot fly to or from an aquatic location. The SailMAV is a fixed-wing robot, similar to a seaplane, that is able to change the orientation of its wings and also use them as sails [8]. In its first iteration, the vehicle demonstrated sailing capabilities as well as a successful take-off from the water's surface. However, demonstrating a controlled flight and landing on the water's surface, followed by a successful take-off and flight to a land-based location, is still an area of ongoing research. While all four of these robots have demonstrated critical portions of an aerial-aquatic mission cycle, none of them are currently capable of completing a full mission.

The purpose of citing these various projects is not to diminish the achievements of their research, but rather to highlight that the field of aerial-aquatic robotics is still in its infancy and that the robots developed thus far currently face at least one of two major challenges. These challenges are: inefficient propulsion systems that dramatically limit mission range and duration, or an inability to complete a full mission cycle by flying to and from an aquatic location as well as collecting data at or beneath the water's surface. These challenges arise as a result of physical constraints unique to aerial-aquatic robots. The first major constraint is that these robots must operate at a large range of Reynold's numbers (Re), which may increase by more than $10x$ between air and water [1]. This means that, in order to operate efficiently in both mediums, these vehicles must use propulsion systems that work well within a range of Re that is much larger than either aerial or aquatic propulsion systems are typically designed for. Furthermore, large lifting surfaces, like wings, only serve to increase drag and energy expenditure underwater as lift forces are not required for aquatic locomotion. Finally, transitioning between the two media presents its own set of unique challenges as it is naturally a very energy-intensive process that either requires high energy-density fuel to escape from underwater or very controlled transition between hydroplaning and flight to escape the water's surface [9, 10].

In order to overcome these constraints, researchers often look to biological systems for design principles that may be applied to aerial-aquatic robots. In the case of aquatic escape, the squid has served as a source of inspiration for both the AquaMAV and Aquatic Jump-Glider. The squid uses an aquatic jet to jump from beneath the water, which inspired the use of jets in both the AquaMAV and Aquatic

Jump-Glider [11, 12]. In terms of water entry, the AquaMAV also folds its wings in order to initiate a plunge dive. This strategy is similar to the behavior observed in diving birds [11]. Furthermore, the strategies for sailing at the water's surface were inspired by sailing strategies observed in mute swans and spiders for the development of SailMAV [1]. Both mute swans and spiders use adaptive morphology to change the shape and orientation of their sails in order to control aerodynamic forces and move in a particular direction [13, 14]. A similar strategy has also been observed in the Portuguese Man-o-War jellyfish. It is believed that these animals use a camber morphing sail to control aerodynamic forces while traveling at the water's surface [15]. Finally, quadrotor-based aerial-aquatic robots typically use some sort of air tank for buoyancy control in order to reach the water's surface. This has often been inspired by the way that fish change their buoyancy in order to reach different underwater depths [16].

1.1.4 Motivation for Developing Flexible Structures for Aerial-Aquatic Robots

One major difference between each of these robots and their biological counterparts is that biological systems are made from inherently soft materials while each of these robots are built from much stiffer ones. In the case of the squid, the jet is produced through muscular contraction of an internal membrane rather than a chemical reaction [6]. Similarly, fish change their buoyancy through inflating and deflating a soft membrane, not by pumping air in and out of a tank [16]. In the sailing case, swans, spiders, and Portuguese Man-o-War jellyfish use the flexibility of their muscles to change the shape of their respective airfoils rather than using rigid mechanisms to rotate those airfoils and change their orientations [1, 17]. In looking at these examples, one can see that almost all aerial-aquatic robots have some form of biological inspiration. However, the lack of flexible structures that can be used for these robots greatly limits the degree to which they can imitate animals. As such, the primary focus of my research is the design of flexible structures that will allow bio-inspired aerial-aquatic robots to better emulate nature. I do this, by developing components of camber morphing airfoils that can be used for both flying and sailing.

1.1.5 Research Objectives

As stated in Section 1.1.1 the goal of my research is design and modeling of honeycomb and kirigami based structures for camber morphing wings used in aerial-aquatic robots. I do this by developing 1D and 3D models of honeycomb and kirigami structures and then use those models to design components of camber morphing airfoils.

In Chapter 2, I review some of the design strategies used in morphing wing and soft robotics research and highlight specific gaps that must be filled before such strategies can be used for aerial-aquatic locomotion. These include, design of flexible honeycomb and kirigami structures and controlled stiffening of these structures through laminar and particle jamming. Then, in Chapter 3, I demonstrate how honeycomb and kirigami structures can be used as building-blocks for flexible aerial-aquatic robots. In this chapter, I detail the development of a flexible strain-sensing structure made from a rigid material and explain a novel analytical model for these structures that has never before been presented. This structure is intended to be used as part of a camber-morphing wing, where it's self-sensing capabilities could be used for real-time feedback for control of the wing's camber. Subsequently, in Chapter 4, I demonstrate how the same structures explored in Chapter 3 can be used in conjunction with laminar jamming to build a camber-morphing wing that can be used for both flying and sailing. This wing can not only change camber, but can also lock itself into a specific shape for a long period of time, which allows it to maintain a desired wing shape without the use of additional actuation. Finally, in Chapter 5, I summarize my findings from the previous chapters and highlight the new research questions that my findings raise.

The use of hyperelastic materials in soft robotics is an area of research that has become increasingly popular in the last decade. However, little to no work has been done to assess whether or not the materials and structures commonly used in soft robotics are appropriate for aerial-aquatic robots. This is of particular importance because, as highlighted earlier in Section 1.1.3, aerial-aquatic robots face a unique set of physical constraints that are not common to other areas of robotics. At the start of my MPhil, one of my primary goals was to evaluate the usefulness of such materials in aerial-aquatic robots as their material properties are much more similar to those found in biological systems than the rigid materials used in aerial-aquatic robots today. Unfortunately, this work, which was primar-

ily experimental in nature, was cut short due to the COVID-19 pandemic. The details of this work are described in Appendix A. There, I begin to evaluate the feasibility of using current soft-robotic actuators in aerial-aquatic robots and conclude with modeling of a successful demonstration of hyperelastic materials in a membrane used for buoyancy control on an aerial-aquatic robot. In Appendix A, I demonstrate the challenges of using hyperelastic materials for large portions of aerial-aquatic robots through prototyping and testing of a hyperelastic camber morphing wing. I then conclude the appendix with a successful example of using hyperelastic materials in an aerial-aquatic robot, MEDUSA, and draw preliminary conclusions on when use of hyperelastic materials is and is not appropriate for this particular application.

1.2 Contributions

Here, I will highlight the scientific and technical contributions of my work which are detailed in chapters 3 and 4. In Chapter 3, I discuss the modeling techniques involved in developing self-sensing, biodegradable structures using either a honeycomb or kirigami pattern. In doing this I develop 1D analytical models for diamond celled honeycomb and horizontal slit kirigami structures structures and validate these models with either FEM, experiments, or both. I then explain how such models can be used not only to design a specific self-sensing structure but also to choose between either a kirigami or honeycomb pattern depending on the application. In Chapter 4, I demonstrate how these structures can be used in conjunction with laminar jamming to design a shape-locking, bidirectional, bending structure (SLBBS) which I use in a morphing wing intended for both flying and sailing. In doing this, I extend the model presented in Chapter 3 for diamond celled honeycombs to a full 3D analytical model of the structure and then present a composite analytical model for the entire SLBBS. I then validate that model with both FEM and mechanical testing, and demonstrate that these SLBBS can be used to build components of aerial-aquatic robots by using one in a morphing airfoil which I test in a wind tunnel. A condensed summary of these contributions can be found in Table 1.1

Table 1.1: Summary of Contributions

Chapter 3 Appendix A	Chapter 4
Scientific	
1D analytical modeling of in-plane diamond-celled honeycomb mechanics and validation of that model through FEM and experiments 1D analytical modeling of in-plane horizontal slit kirigami mechanics and validation of that model through experiments	3D homogenization of diamond-celled honeycombs and validation of that model through experiments and FEM
Technical	
A demonstration of how such analytical models can be used to aid in design of a flexible, bio-degradable, strain and force sensing structure.	Design of honeycomb and laminar jamming structures for a SLBBS Analytical and FEM composite models that demonstrate the mechanics of stacked honeycomb and laminar jamming structures Manufacturing methods for SLBBS

Chapter 2

Background

This chapter provides the background information needed to understand the scientific contributions of Chapter 3 and Chapter 4. Both Chapter 3 and Chapter 4 discuss the development of structures used in a camber-morphing wing, so Section 2.1 explains why camber morphing wings are of particular interest for both aerial and aquatic locomotion. Following that, Section 2.2 provides an overview of how honeycomb and kirigami structures have been used in morphing wings and more generally within robotics in order to highlight some of the research gaps that my work fills. It then discusses the modeling techniques used for homogenizing these structures, which is critical for understanding the models developed in Chapter 3 and Chapter 4. Finally, the chapter concludes with an overview of different methods of controlled stiffening of flexible structures, which is relevant for understanding my use of laminar jamming structures in Chapter 4.

2.1 Motivation for Camber Morphing Wings in Aerial-Aquatic Robots

The development of camber morphing wings has been of particular interest in the design of aerial vehicles as it can enable more efficient flight [18]. Today, most fixed wing aerial vehicles change the camber of their wings through the use of control surfaces such as flaps, ailerons, rudders, or elevators. Changing the camber of the wing with these control surfaces allows the vehicle to take-off, land, and

control its orientation during flight as adjusting a wing's camber allows it to redirect the flow around the airfoil, thus changing the magnitude and direction of the forces acting on the wing. These control surfaces are typically attached to the wing with hinges, and when actuated, cause the shape of the wing to become discontinuous. This causes a change in the pressure distribution over the corner created at the hinge, and results in increased drag [19]. In a camber morphing wing, this is not the case. Rather than having a hinge that creates this discontinuity in the wing's surface, the entire structure of the wing bends, allowing the wing's surface to remain smooth. Without the discontinuity in the wing's surface, there is not sharp pressure change along the surface of the wing and less drag is produced for the same amount of lift [19]. This leads to more efficient flight because the propulsion system generating the thrust that pushes the vehicle forward has less drag to fight against, and ultimately this allows the vehicle to fly and maneuver using less fuel.

In addition to that, camber morphing wings can also be used for sailing. In the same way that changing the camber of a wing in flight is useful for maneuvering an aerial vehicle because it changes the magnitude and direction of forces acting on the wing, changing the camber of a wing used for sailing can also be used to maneuver a vehicle at the water's surface by changing the forces acting on that sail. In fact, it is believed that the Portuguese Man-of-War jellyfish sails in precisely this way [15]. Fig. 2.1 serves to illustrate how camber morphing wings can be used for both aerial-and aerial-aquatic locomotion.

Consequently, Chapter 3 and Chapter 4 focus on the development of a camber morphing airfoil because it can be used to produce more efficient flight than traditional wings, and that same morphing wing can also be used as a sail.

2.2 Honeycomb and Kirigami Structures For Flexible Robots

The following section provides the necessary background information for Chapter 3 and Chapter 4. Those chapters discuss the use of kirigami and honeycomb structures for aerial-aquatic robots. Section 2.2.1 presents a review of current honeycomb and kirigami research, which highlights the research gaps that Chapter 3 and Chapter 4 fill. Section 2.2.2 provides background information on honeycomb mechanics which is necessary to understand the analysis in Chapter 3 and Chapter 4.

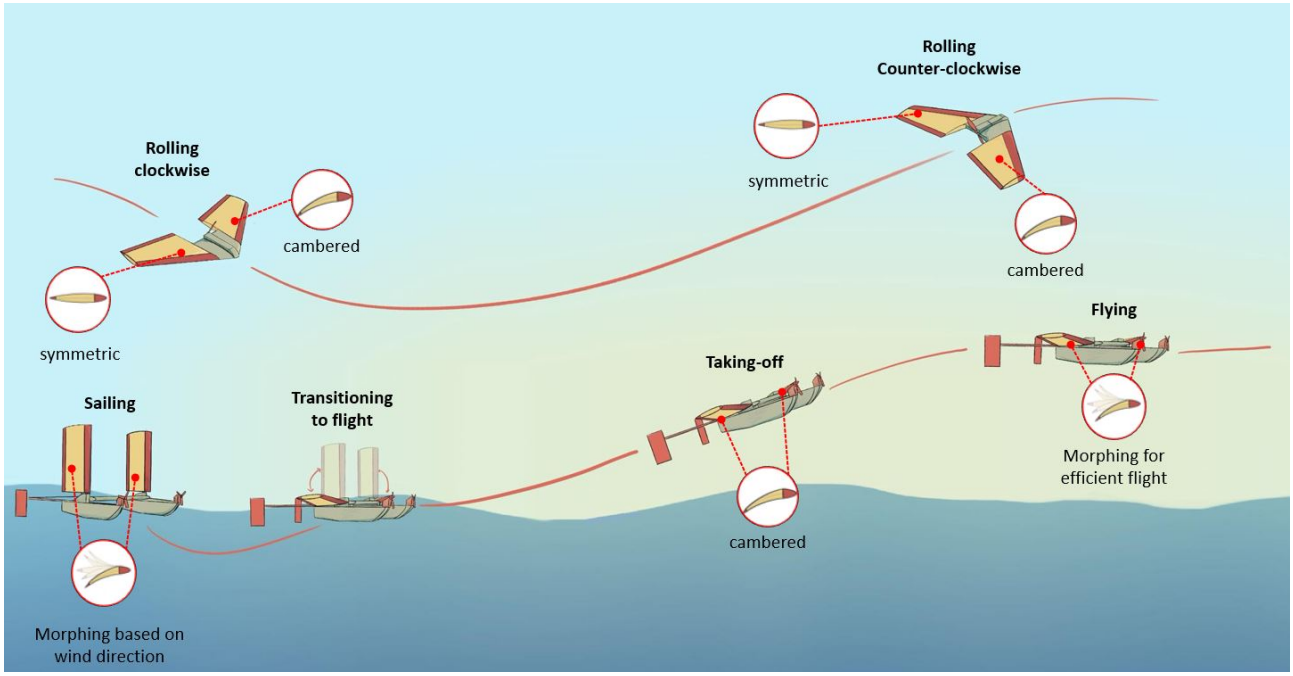

Figure 2.1: An illustration demonstrating the use cases for a camber morphing wing in both aerial and aerial-aquatic locomotion. Such a wing could be used for aerial locomotion, by allowing the vehicle to both fly efficiently and control it's orientation. It can also be used for aquatic locomotion, as a morphing sail, allowing an aerial-aquatic vehicle to move on the water's surface.

2.2.1 Flexible Honeycomb and Horizontal Slit Kirigami Structures in Robotics

A honeycomb is a repeating pattern of prismatic unit cells where each cell wall is made from a solid material [20]. Honeycombs are common in aerospace applications because they are much lighter than the solids they are made from. Typically, they are used in the middle of a composite sandwich to create a stiff and light-weight structure rather than a compliant one [21]. However, design of honeycomb structures for morphing wings has become a new and interesting area of research where aerospace engineers are taking advantage of the natural compliance found in honeycombs [18, 22–26]. In addition to that, honeycomb structures have also been used for other actuators in soft robotics. For example, [27, 28] use honeycomb structures to build tendon driven and hydro-active flexible actuators.

Kirigami involves cutting a pattern of slits into a material in order to modify its mechanical properties. There are a wide variety of kirigami patterns that have been used in soft robotics [29–34], but one of the most common consists of a series of horizontal slits cut across a sheet of material [33, 35, 36]. When the sheet is stretched, these slits open in such a way that the kirigami pattern appears very

similar to a diamond celled honeycomb. In this thesis, this particular kirigami pattern is referred to as "horizontal slit kirigami". Both honeycomb structures and horizontal slit kirigami can be modeled using honeycomb theory and both allow for the use of stiff materials in designing compliant structures [37]. Kirigami structures have also become popular for actuation and sensing tasks in soft robotics over the past decade [33, 34, 38–41].

There are a few major gaps in current honeycomb and kirigami research that my work addresses. Currently, there are 1D analytical models for diamond celled honeycombs [42]. While these models do use the traditional honeycomb theory methods explained in Section 2.2.2, they have never been validated by either FEM or experiments. Chapter 3 validates the existing model using FEM. It also describes mechanical testing on these diamond celled honeycombs and presents a new analytical model that is in better agreement with these experimental results. Furthermore, while honeycomb theory can also be used to describe horizontal slit kirigami structures, such a model has also never been presented. Chapter 3 presents a honeycomb theory based mechanical model and also validates that model with experiments. Finally, no one has ever evaluated whether or not these diamond celled honeycombs are a viable option for flexible structures in aerial-aquatic robots. Chapter 4 addresses this through the design, manufacturing, and testing of diamond celled honeycombs for a camber-morphing airfoil that can function as both a wing and a sail. Furthermore, a 3D analytical mechanical model for diamond celled honeycombs has never been presented. Such a model is also presented in Chapter 4 and is validated with both FEM and experiments.

2.2.2 Mechanics of Honeycomb Structures

Both honeycombs and horizontal slit kirigami structures can be modeled using honeycomb theory [37]. This theory was first described by Gibson et. al. in this paper [20] and a more detailed overview of the theory can be found in a Chapter four of their textbook, *Cellular Solids: Structure and Properties* [21]. The overall goal of this section is not to show a detailed example or derivation of this theory. It is merely to familiarize the reader with the concept of honeycomb mechanics at a high-level. Detailed examples of applications of this theory can be found in the previously cited paper and text book as well as in chapters Chapter 3 and Chapter 4.

This theory allows an engineer to homogenize a large honeycomb or horizontal slit kirigami structure such that it can be treated as a new linear-elastic material with properties E^*, ν^*, and G^*. The basic methodology of this theory is as follows: one analyzes a unit-cell of the repeating honeycomb or kirigami pattern, applies a far-field stress to that cell in a particular direction, uses beam theory to calculate the resulting change in length of the cell, and then uses that resulting deformation to calculate material constants E^*, ν^*, and G^*. In some applications, defining these constitutive relations in a single direction is sufficient, while in others a full three-dimensional description of the homogenized material is required. Chapter 3 will demonstrate an example of the former while Chapter 4 will show the latter.

2.3 Methods of Controlled Stiffening: Laminar and Particle Jamming

While there are many safety and functional advantages to using soft robots, there are specific cases where a stiffer structure may be desirable [43]. Consequently, researchers have also investigated ways of temporarily rigidizing portions of soft robots [43–48]. This allows soft robots to hold specific shapes under large loads, or temporarily stiffen in order to complete task that requires rigid interaction. Both laminar (or layer) and particle jamming are methods of stiffness control utilized in soft robots. They allow soft robots to be compliant in certain cases and stiff in others by applying pressure to a jamming material. In particle jamming, granular particles are allowed to flow freely within a confined space allowing the robot to remain soft, but when some form of pressure is applied, the particles pack tightly together to stiffen the entire system [47]. Laminar jamming has a very similar working principle, but instead of using granular particles, thin layers or sheets of material are stacked on top of each other and when pressure is applied these sheets are forced together and behave as a block of the material, thus stiffening the section of the robot [44].

As a method of stiffness control, there are both passive, and active particle jamming mechanisms. Passive particle jamming mechanisms, like the one used in this gripper [47], do not require any additional actuators. As the fingers in the gripper move, the compartments holding the particles expand

and contract, so the stiffness of each finger is directly dependent upon the gripper's configuration. Conversely, active particle jamming decouples the stiffness of the system from its configuration by using a separate actuator to jam the particles. This ball-and-socket joint spine [48], for example, uses a vacuum pump to force the particles together and stiffen the spine in any configuration it is put in.

Comparatively, laminar jamming has been used in a variety of applications such as shape locking of soft actuators [44], quadrotor landing gear [45], and robotic kangaroo tails [46]. One of the great advantages of this type of jamming method is that it is much easier to model than its particle jamming counterpart. Particle jamming has lots of different models that vary based on the particle size, the space the particles are enclosed in, and the particles themselves [43, 47] while most laminar jamming models only require knowledge of the layering material properties [44]. Essentially, when the structure is unjammed, it can be modelled as a series of thin sheets that each have their own stiffness, but when the structure is jammed, it can be modelled as a single block of that same material. Thus, the stiffness of the material increases by n^2 where n is the number of layers of material [44]. In many cases, laminar jamming systems use a vacuum pump to apply pressure to the individual layers, like in the case of the landing gear, and shape locking actuators mentioned previously, but almost any form of pressure application can be used, such as an actuated mesh that is constricted around the layers, as seen in the kangaroo tail [46]. In addition to being used for stiffness control, laminar jamming structures have also been used to modify the dynamic response of certain structures, which again makes them of particular interest, because the modeling of this behavior is also fairly well understood when compared to particle jamming structures [45].

Chapter 3

1D Modeling of Honeycomb and Kirigami Structures

3.1 Motivation and Contributions

This chapter will discuss 1D analytical modeling and mechanical testing of diamond celled honeycomb and horizontal slit kirigami structures made from microfibrillated cellulose (MFC) through the lens of a larger research project focused on design, manufacturing, modeling, and testing of compliant, bio-degradable, self-sensing structures. The primary goal of this larger research project was to develop compliant structures that could be used as building blocks for soft aerial eco-robots. These robots are intended to be biodegradable such that they can perform sensing tasks in natural and vulnerable environments without producing hazardous eco-waste if they become damaged or break. As part of this project, we developed a flexible, biodegradable strain-sensing structure that will eventually be integrated into a camber morphing wing. Using a flexible internal structure, like the one investigated here, may allow for more efficient roll control of the vehicle. Functionalizing it with self-sensing capabilities can provide feedback for controlling the wing's camber. Cellulose was an obvious choice for a base material as it is one of the most abundant and biodegradable materials on Earth. Unfortunately, it is naturally very stiff, which is why we investigated using diamond celled honeycomb and horizontal slit kirigami structures as a way to build soft structures from this naturally stiff material.

For the purposes of my larger research goal, this project served as an opportunity to develop analytical

models for diamond celled honeycomb and horizontal slit kirigami structures in order to compare and contrast the benefits of each structure for use in aerial-aquatic robots. The manufacturing, mechanical testing, and self-sensing characterization of these structures was completed by Fabian Wiesemuller, so those aspects of this project will not be discussed here. A discussion of that work, as well as my own, can be found in our publication [37]. Unlike the work described in Chapter 4, which has a heavy design focus, this work does not aim describe the process of designing a specific self-sensing structure with a geometry that is meant to satisfy specific design constraints. Rather, we are merely demonstrating, that diamond celled honeycomb and horizontal slit kirigami structure structures can be used to make biodegradable strain sensors. For that reason, the design methodology for the sensor discussed here is not described in this chapter.

The scientific and technical contributions of the work I will discuss in this chapter are:

- 1D analytical modeling of in-plane diamond celled honeycomb mechanics and validation of that model through FEM and experiments
- 1D analytical modeling of in-plane horizontal slit kirigami mechanics and validation of that model through experiments
- A demonstration of how such analytical models can be used to aid in design of a flexible, biodegradable, strain and force sensing structure.

3.2 Diamond Celled Honeycomb vs. Horizontal Slit Kirigami

As discussed in Section 2.2.1, there are a wide variety of honeycomb and kirigami structures used in soft robotics. However, our motivation for investigating, specifically, diamond celled honeycomb and horizontal slit kirigami structures comes from biological inspiration. Ice plants (*Delosperma nakurense* (Engl.) Herre) use a flexible honeycomb micro-structure to unfold and release their seeds. That structure looks very similar to both a diamond celled honeycomb and horizontal slit kirigami structures [49]. Furthermore, both of these structures have been used to make compliant robotic components, which makes them good candidates for this particular application [27, 50]. A comparison of both of these structures with the structure seen in ice plants can be found in Fig. 3.1.

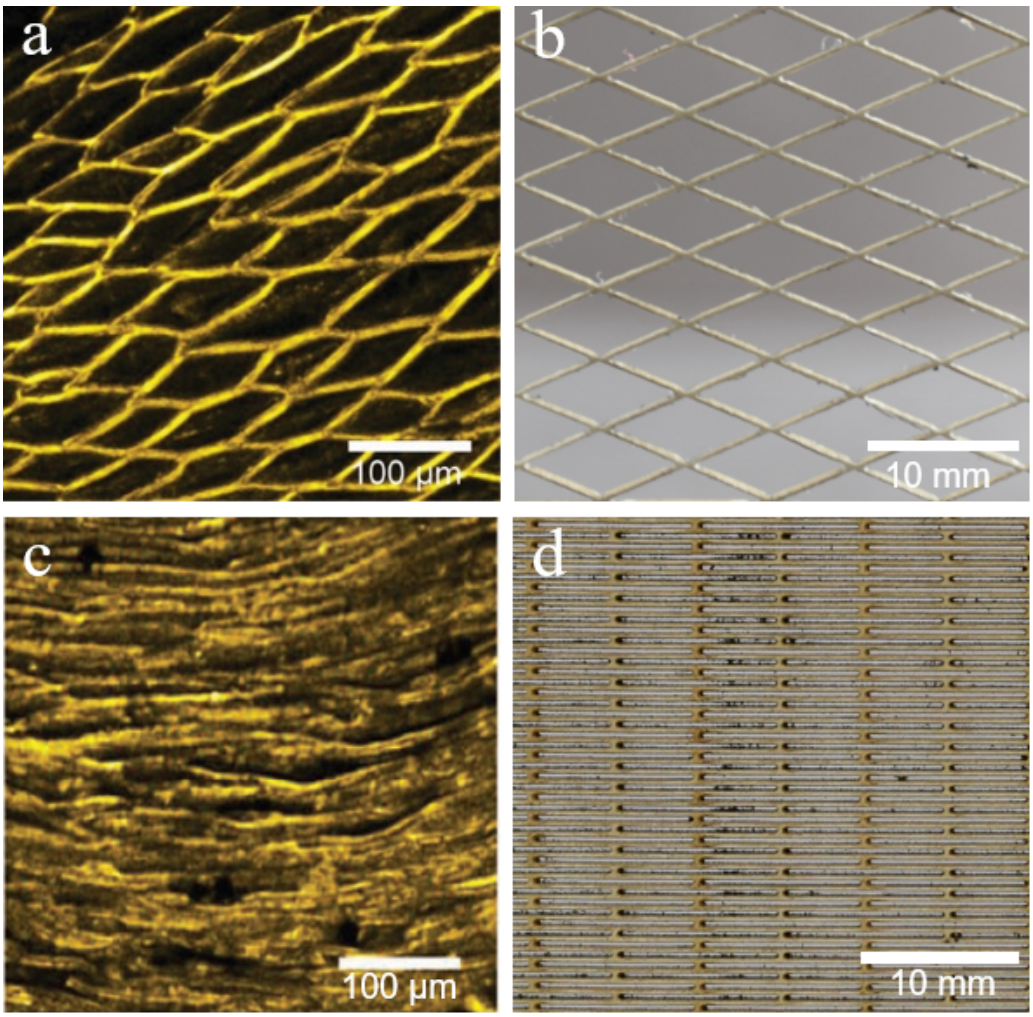

Figure 3.1: **a)** Confocal image of a hydro-actuated seed capsule of an ice seed plant in an opened state taken from [49] ©2021 Springer Nature. **b)** Macro-image of the manufactured compliant cellulose honeycomb structure taken from [37] ©2021 IEEE. **c)** Confocal image of a hydro-actuated seed capsule of an ice seed plant in a closed state taken from [49] ©2021 Springer Nature. **d)** Macro-image of the manufactured compliant cellulose horizontal slit kirigami structure.

In order to evaluate which of these two structures is most useful for aerial-aquatic robots, it is imperative to understand how they differ in terms of both stiffness and weight. When both structures are under the same applied tensile load of 200 g, one can clearly see that the kirigami structure is less stiff. Under the same 200 g load, the horizontal slit kirigami structure deforms by 11 mm while a diamond celled honeycomb with $\theta = 15°$ only deforms by 2 mm. This is demonstrated in Fig. 3.2. Furthermore, as I will prove more rigorously in the subsequent sections, the stiffness of the honeycomb structure increases even further as the angle between the cell walls increases.

While the kirigami structure has the clear benefit of being the more compliant of the two, it is also more dense. In a diamond celled honeycomb, as the angle between the cell walls increases the density

of the structure decreases. This can be demonstrated by the formula $\bar{\rho} = \frac{2t}{lsin(2\theta)}$ given by [51], where $\bar{\rho}$ is the relative density between the honeycomb and the material it is made from and 2θ is the angle between the cell walls. Comparatively, since virtually no material is removed from the kirigami structure, the density of the kirigami is virtually the same as the density of the material it is made from (i.e. $\bar{\rho} \sim 1$). In order to evaluate which of the two materials is best suited for aerial-aquatic robots, given these observations, I develop and validate analytical models for the stiffnesses of these structures so that this trade-off can be considered in a more analytical way.

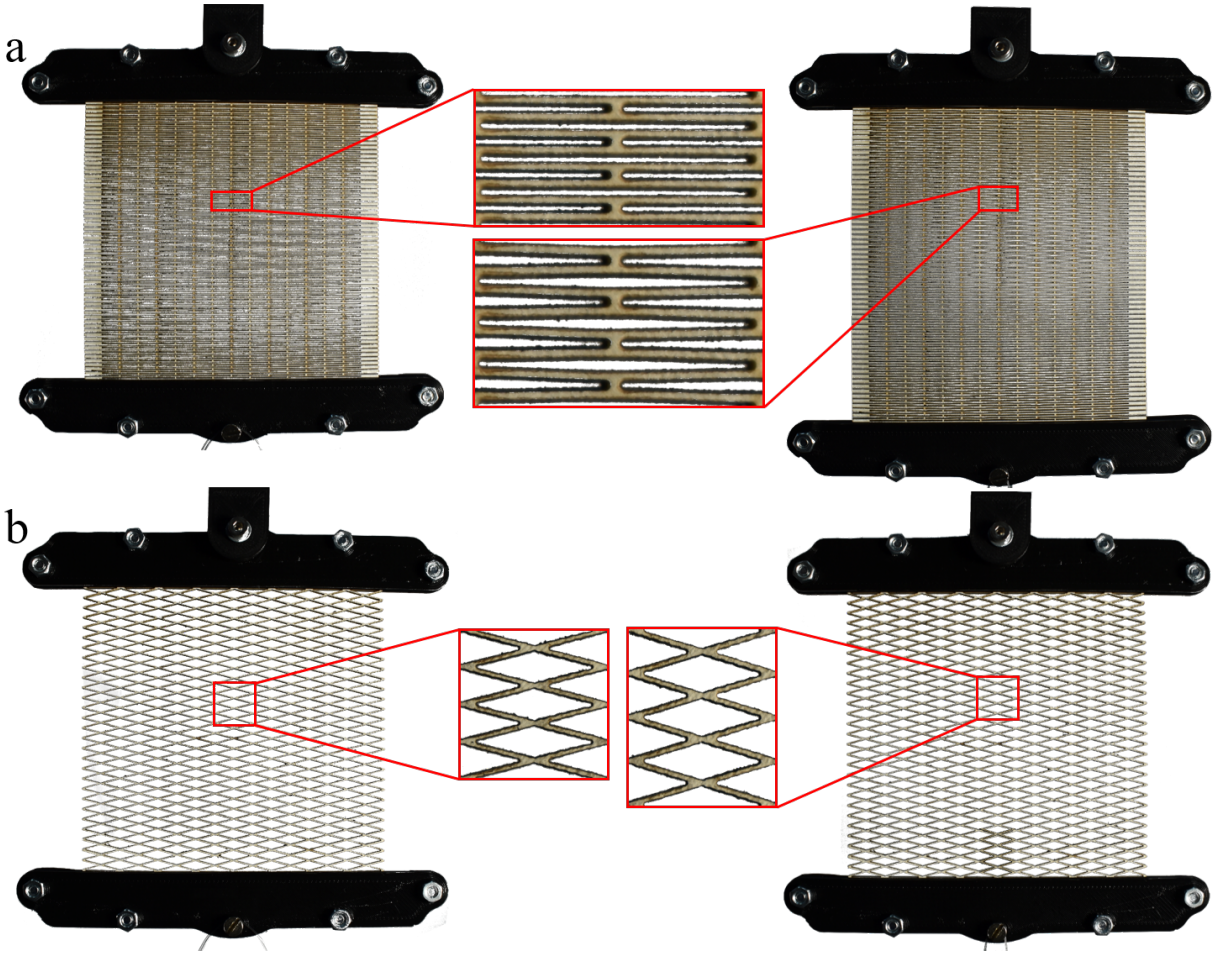

Figure 3.2: Comparison of stiffness between kirigami and a diamond celled honeycomb under a 200 g tensile load. Left column showing the structure unloaded, right column showing the structure loaded taken from [37] ©2021 IEEE. **a)** Kirigami structure with a total displacement of 11 mm. **b)** Honeycomb structure (θ = 15.0 °) with a total displacement of 2 mm.

3.3 Mechanical Modeling

This section details the mechanical modeling of both diamond celled honeycomb and horizontal slit kirigami structures. The purpose of these models is to understand how the stiffnesses of these structures vary with their geometries and the materials they are made from so that I can better assess their suitability for a camber morphing wing. Section 3.3.1 uses the honeycomb theory outlined in Section 2.2 to describe the in-plane mechanics of diamond celled honeycombs and validates that model with FEM. Section 3.3.2 modifies the model presented in Section 3.3.1 such that it is in better agreement with the experimental results shown in Section 3.4. Finally, Section 3.3.3 uses the honeycomb theory outlined in Section 2.2 to describe the in-plane mechanics of horizontal slit kirigami structures.

The model presented in Section 3.3.1 is in agreement with other models in the literature, but has never been validated through experiments or FEM. The primary contribution of this section is the validation of that model. Section 3.3.2 and Section 3.3.3 derive new analytical models that have never before been presented in the literature.

3.3.1 Diamond Celled Honeycomb Homogenization

Using the honeycomb theory developed by Gibson et al. [20], which I outlined in Section 2.2, each of the walls in the diamond cell is approximated as a beam. The structure is then homogenized by calculating the stress and strain on a single diamond cell. Knowing this stress, and corresponding strain, allows me to then treat the diamond celled honeycomb as a new material with a young's modulus E_h^*.

When an entire diamond celled honeycomb lattice is loaded uniaxially, each cell experiences a far field stress which I denote as σ_∞. This stress state, depicted in Fig. 3.3**a**, causes the internal forces and moments shown inFig. 3.3**b**. On a single cell wall, σ_∞ causes an internal force P and acts over the area $lbcos(\theta)$. This is the area that σ_∞ would act on were this honeycomb a solid block of material. Given that the purpose of this analysis is to develop material constants so that we can treat it as such, σ_∞ can be expressed per Eq. (3.1).

$$\sigma_\infty = \frac{P}{lbcos(\theta)} \tag{3.1}$$

The amount that a single cell wall contributes to the overall length of a diamond-cell in the direction that σ_∞ is applied is $lsin(\theta)$. Once that far-field stress, σ_∞, is applied, the cell wall deflects by an amount δ. This means that the length of the cell changes by $\delta cos(\theta)$, resulting in an ε given by Eq. (3.2).

$$\varepsilon = \frac{\delta cos(\theta)}{lsin(\theta)} \tag{3.2}$$

Using, Euler-Bernoulli beam theory, one finds that δ is given by Eq. (3.3).

$$\delta = \frac{Pcos(\theta)l^3}{12E_sI} \tag{3.3}$$

where E_s is the Young's modulus of the bulk material, and I is the area moment of the cell wall, $bt^3/12$. If we treat the diamond celled honeycomb as a linear-elastic material with constitutive relation $\sigma = E_h^*\varepsilon$, we get Eq. (3.4).

$$\bar{E}_h = \frac{E_h^*}{E_s} = \left(\frac{t}{l}\right)^3 \frac{sin(\theta)}{cos^3(\theta)} \tag{3.4}$$

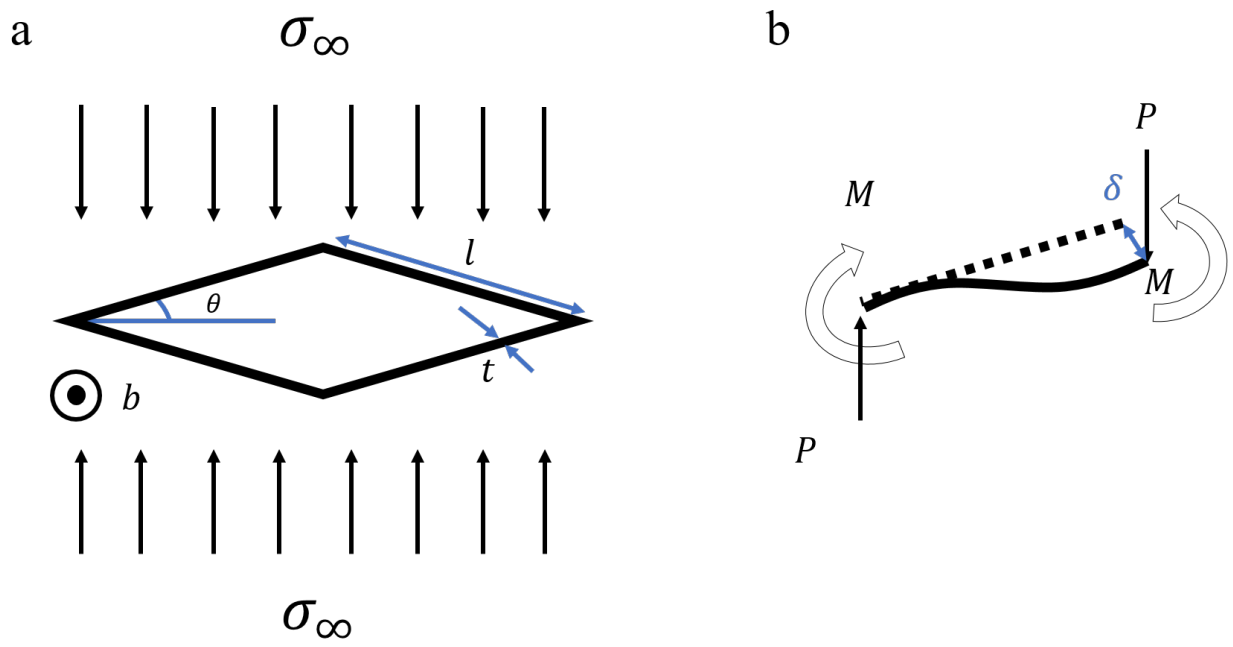

Figure 3.3: Loading condition and geometric constants for derivation of (Eq. (3.4)) taken from [37] ©2021 IEEE. **a)** a single cell loaded with far field stress σ_∞. **b)** Free body diagram of a single cell wall.

Similar forms of this expression have been documented for bi-modulus diamond-celled structures [52] and diagonally loaded square celled honeycombs [53]. However, this exact formulation could

not be found, so I validated it with, a series of FEM simulations conducted in Abaqus 2019. Each of the cells were modeled with shell elements using the mesh shown in Fig. 3.4**a**. The honeycomb was constrained at one end in y, z, and rotations about all axes while a concentrated force was applied at each node along the edges at the opposite end of sample. The honeycomb was not constrained in x so as to neglect edge effects. Honeycomb theory assumes that the honeycomb has infinitely many cells in order to be properly homogenized. Allowing the cells to translate in the x direction at the boundary provides the same affect as the honeycomb being infinitely long in the direction it is being loaded, but dramatically reduces computation time. A comparison of the FEM and analytical models is shown graphically in Fig. 3.4b.

In these simulations, angles greater than 45 ° were not investigated. The model should still be valid at angles larger than 45 °, but as this chapter intends to investigate the trade-offs between stiffness and weight of diamond celled honeycomb and horizontal slit kirigami structures, such larger angles are not relevant. In the case of $\theta > 45$ °, a structure of the same weight could be rotated by 90 ° and have a lower stiffness. Therefore, when comparing these structures to horizontal slit kirigami structures, one would never consider using a diamond celled honeycomb with $\theta > 45$ ° for an aerial-aquatic robot.

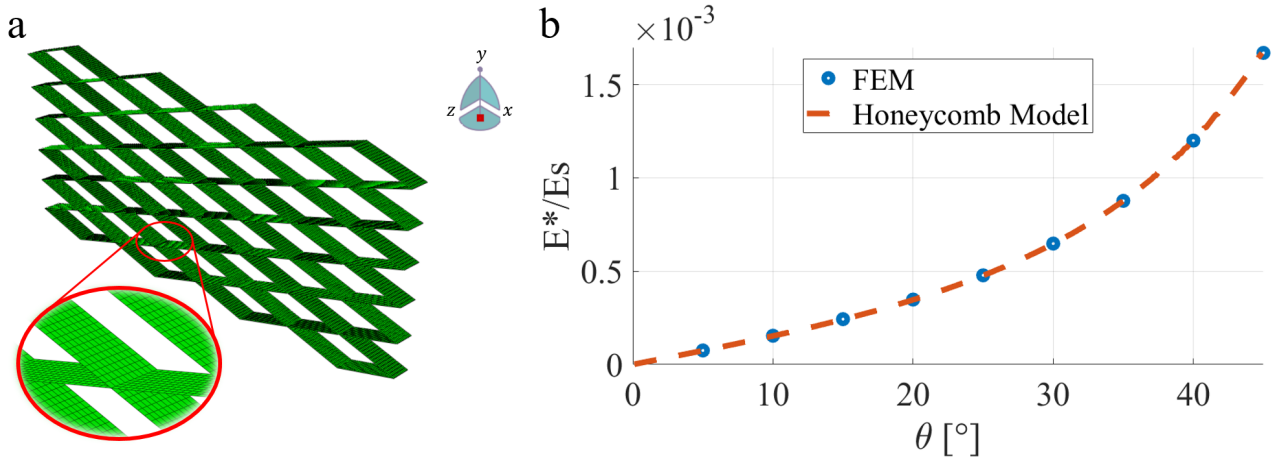

Figure 3.4: FEM simulation mesh and comparison of FEM results with (Eq. (3.4)). **a)** FEM simulation mesh. Each cell wall is modeled with shell elements and has 20 elements along its length and 10 along its depth. **b)** Plot showing both the stiffness ratios of the honeycomb model described in (Eq. (3.4)) and the FEM simulations.

3.3.2 Extension of Diamond Celled Honeycomb Homogenization

According to Eq. (3.4), as $\theta \rightarrow 0$ °, so does the young's modulus of the honeycomb, which is a physical impossibility. This is because the affect of the thickness of each cell wall on the geometry is neglected. From a geometric point of view, each of the beams in the cell wall is represented as a line in Section 3.3.1. Since each of these lines represents a beam with some thickness, those beams form an overlapping region which is shown in dark gray in Fig. 3.5. In Section 3.3.1, this overlapping region is not only double counted towards the length of each cell wall, but as this region is almost like a block of material with beams extending from it, it's deformation is very small relative to the deformation of each of the beams. This can be seen in Fig. 3.5**a**. This FEM simulation was only used in to visualize the stress-strain state of each of the beams in the honeycomb structure. It was run in Fusion 360 using a dense 3D element adaptive mesh refinement that converged on a value of maximum displacement after three iterations.

a b

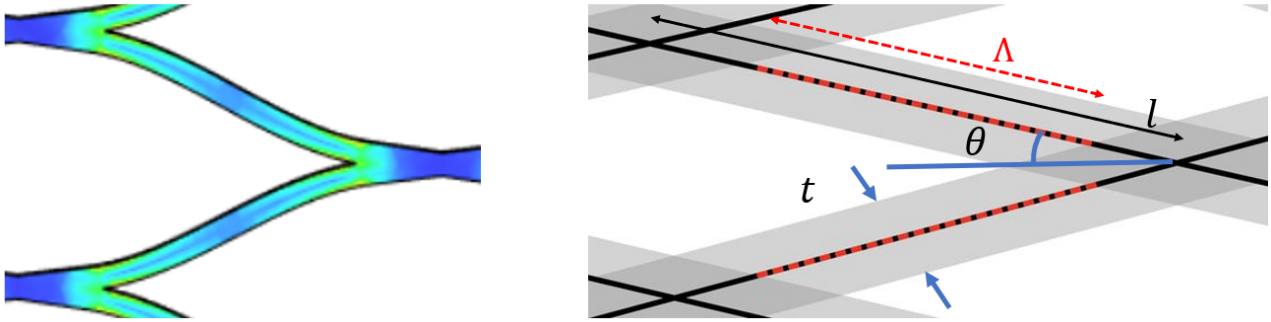

Figure 3.5: FEM used to extend preliminary model and geometry that corresponds to that model. **a)** FEM simulation run in Fusion 360 using a dense 3D element adaptive mesh refinement that converged on a value of maximum displacement after three iterations. The blue regions represent regions with the lowest amounts of stress while the green/yellow represent regions with the highest amounts of stress. **b)** Geometry corresponding to (Eq. (3.5)) taken from [37] ©2021 IEEE. The black lines represent the diamond with lines of length l, the gray represents the actual structure with thickness t, where the darker gray sections are where the cell walls overlap. The dashed red line is the midline of the beam of length Λ.

As such, Eq. (3.4) is modified to the following formulation

$$\bar{E}_h = \frac{E_h^*}{E_s} = \left(\frac{t}{\Lambda}\right)^3 \frac{sin(\theta)}{cos^3(\theta)} \qquad \text{where,} \qquad \Lambda = l - \frac{t}{sin(2\theta)} \tag{3.5}$$

In Eq. (3.5), the diamond cell with walls of length l is composed of beams of length Λ. In this model,

I assume that the regions where four of the cell walls overlap do not deform at all. This definition is in much better agreement with our experimental results shown in Fig. 3.7.

The overlapping region is nearly negligible for large values of θ, but as θ decreases, this region becomes larger. As such, this model becomes less and less accurate as $\frac{\partial \bar{E}_h}{\partial \theta} \to 0$. Since the regions of overlapping material are modeled as undeformable, at very small angles, $\bar{E}_h$ begins to increase as the majority of the structure consists of sections with essentially infinite young's modulus. This causes $\frac{\bar{E}_h}{\partial \theta} < 0$ at very small angles. While this does present limitations on the validity of this model at small θ, it is also much harder to manufacture diamond celled honeycombs with angles that are small enough for this to become relevant. Furthermore, as discussed previously, horizontal slit kirigami structures are much less stiff than diamond celled honeycombs and as $\theta \to 0$, $\bar{\rho}_h \to \bar{\rho}_k$. For these reasons, when comparing a diamond celled honeycomb to a kirigami structure, one would never consider a diamond celled honeycomb with such a small angle for an aerial-aquatic robot. This means that while the model is less accurate at smaller angles, it is sufficient for the purposes of comparing these two structures for use in aerial-aquatic robots.

3.3.3 Horizontal Slit Kirigami Homogenization

The same modeling techniques used for diamond celled honeycombs can also be used for kirigami structures. Investigations into how the stiffness of these structures changes with geometric parameters has been shown [33], but an explicit homogenization of the horizontal slit kirigami structure, that allows us to treat it as a new material with young's modulus, E_k^*, has not been demonstrated. In this case, each cell wall has a length $2l$, where each of the cell walls in the kirigami structure are twice as long as the cell walls in an analogous diamond celled honeycomb. If the same far field stress, σ_∞, is applied to a sheet of material with the horizontal slit kirigami pattern, the resulting forces and moments acting on each beam are shown in Fig. 3.6. Using the same process discussed in Section 3.3.1, one finds that,

$$\sigma_\infty = \frac{P}{2lb}, \quad \varepsilon = \frac{\delta}{t/2}, \quad \delta = \frac{Pl^3}{24E_sI}$$

This leads to the final expression,

$$\bar{E}_k = \frac{E_k^*}{E_s} = \frac{1}{2}\left(\frac{t}{l}\right)^4 \tag{3.6}$$

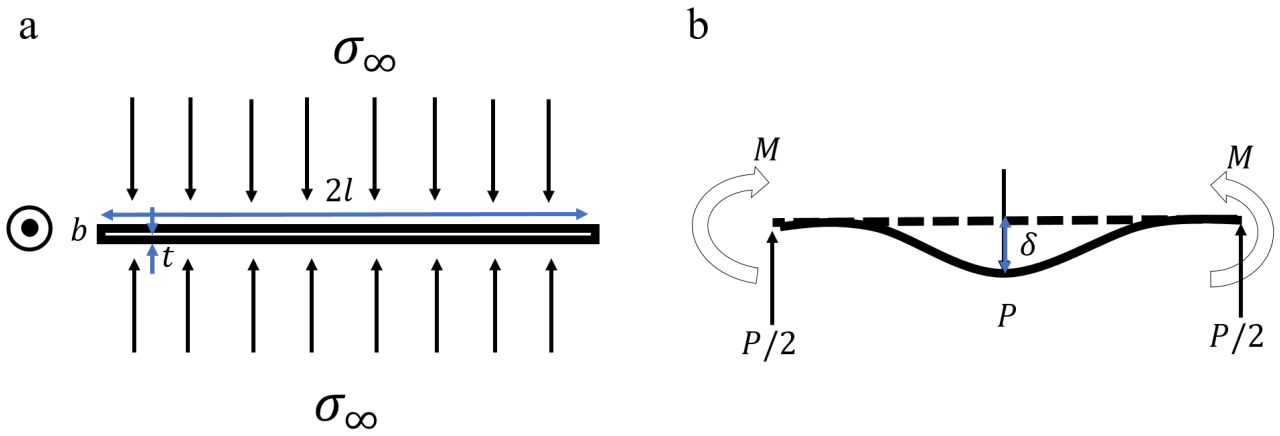

Figure 3.6: Loading condition and geometric constants for derivation of (Eq. (3.6)) taken from [37] ©2021 IEEE. **a)** a single cell loaded with far field stress σ_∞. **b)** Free body diagram of a single cell wall.

3.3.4 Unified Model

Each of the specimens tested in Section 3.4 was manufactured from 100 mm x 100 mm MFC plates. Once these plates were manufactured, using the method described in [37], the various diamond celled honeycomb and kirigami patterns were laser-cut from those plates. In testing various geometries, values of $t = 0.50\,mm$ and $l = 5.3\,mm$ mm were chosen in order to minimize the ratio of t/l within the constraints of our $100\,mm$ x $100\,mm$ plates and the tolerances of the laser cutter. Once this was decided, it was soon discovered that honeycomb structures with $\theta < 15.0\,^\circ$ could also not be accurately manufactured by the laser cutter. For this reason, and the reasons discussed in Section 3.3.2, using a kirigami structure instead of a honeycomb with $\theta < 15.0\,^\circ$ is far more reasonable. This results in the model shown in Eq. (3.7).

$$\frac{E^*}{E_s} = \begin{cases} \left(\frac{t}{\Lambda}\right)^3 \frac{sin(\theta)}{cos^3(\theta)}, \text{ if } 15^\circ \leq \theta \leq 45^\circ \\ \frac{1}{2}\left(\frac{t}{l}\right)^4, \text{ otherwise} \end{cases} \tag{3.7}$$

This unified model is only given to demonstrate that diamond celled honeycombs with $15.0\ ^\circ < \theta < 45.0\ ^\circ$ were considered since honeycombs with smaller θs could not be manufactured. This is not intended to suggest that the Eq. (3.5) converges to Eq. (3.6) as $\theta \to 0^\circ$ or that $15.0\ ^\circ$ is the point at which $\frac{\partial \bar{E}_h}{\partial \theta} = 0$. This unified model only represents the point at which is becomes most practical to consider kirigami structures instead of diamond celled honeycombs given what is discussed at the end of Section 3.3.2.

3.4 Results and Discussion

To validate the accuracy of the developed unified model, tensile tests were performed to determine the Young's modulus E^*. By doing so, diamond celled honeycombs with different angles, θ, were cut out from MFC plates and tested using a mechanical testing machine (Z010 RetroLine, ZwickRoell GmbH & Co. KG, Ulm, Germany) and a 20 N load-cell. Each specimen was subjected to the same tensile load five times. Fig. 3.7 shows the measured $\frac{E^*}{E_s}$ ratios for the angles $15.0\ ^\circ$, $22.5\ ^\circ$, $30.0\ ^\circ$, $37.5\ ^\circ$, $45.0\ ^\circ$, and the kirigami geometry (shown as $0\ ^\circ$). Compared to the stiffness predicted by the unified model. The error bars in shown in Fig. 3.7 are 95% confidence intervals for each of the measurements. In order to calculate the young's modulus of each MFC plate, several tensile specimens in different locations on the same plate were tested. These confidence intervals account for the different values of E_s measured at different locations on the plate and the different values of E^* that were measured with the same specimen. The measured young's moduli of the MFC plates tested are given in Table 3.1. In that table, the $15.0\ ^\circ$, $22.5\ ^\circ$, and $30.0\ ^\circ$ honeycombs tested were made from plates 1 and 4. The $37.5\ ^\circ$ honeycombs were made from plates 2 and 3, and the $45.0\ ^\circ$ honeycombs were made from plates 1 and 2. The kirigami plates tested were made from plates 2 and 4.

Table 3.1: Mechanical properties of the investigated MFC specimens.

Plate	Number of Specimens	$E_s[MPa]$
1	4	2.281 ± 0.20
2	4	2.276 ± 0.57
3	4	2.410 ± 0.90
4	3	2.291 ± 0.33

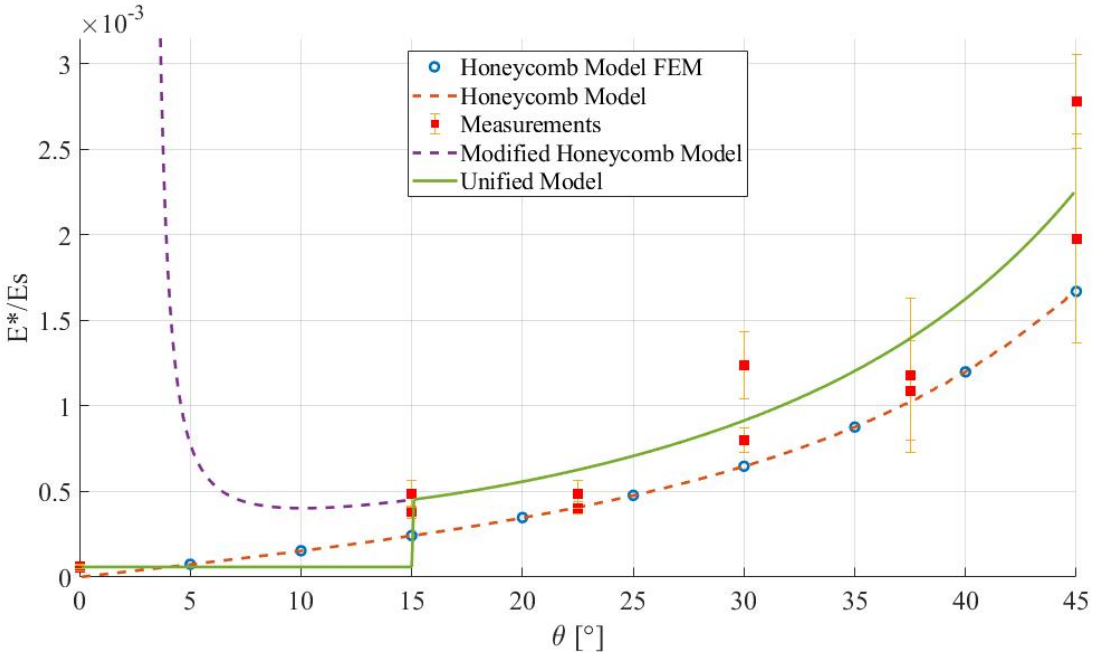

Figure 3.7: Plot of the ratios determined using FEM on honeycomb structures with various angles of θ, the actual measured ratios and their 95% confidence intervals, which are denoted as uncertainties, the initial honeycomb model shown in (3.4), the modified honeycomb model shown in Eq. (3.5), and the unified model shown in (3.7) taken from [37] ©2021 IEEE.

From this experiment, we noted that the young's modulus of the MFC plate was reduced by a factor ranging from 19000 for the kirigami structure to 360 for the honeycomb structure with $\theta = 45°$. The root mean square error (RMSE) between the unified model and the measured data is $2.4x10^{-4}$. As the unified model is simply the honeycomb model at angles $15.0° < \theta < 45.0°$ and the kirigami model for $\theta < 15.0°$, it also makes sense to report the RMSE for each of these models separately. The RMSE for the honeycomb model Eq. (3.4) is $2.6x10^{-4}$ while the RMSE for the kirigami model Eq. (3.6) is $4.8x10^{-6}$. The calculation of the RMSE values does not account for measurement uncertainty.

To demonstrate the usefulness of these structures in a practical way, we decided to manufacture a self-sensing with $\theta = 19.3°$ based on the desired stiffness and density properties for a camber morphing wing (the concept for this particular morphing wing is discussed in more detail in our publication [37]). The structure was coated in a carbon-conductive ink and was connected to a Wheatstone bridge in order to measure changes in resistance of the structure when loads were applied. The self-sensing structure was fabricated and tested with both step-wise and cyclic loading by Fabian Wiesemüller. The plots showing its performance as a sensor are reproduced in Fig. 3.8 to reinforce that these structures are not just flexible, but that they can also be functionalized for specific applications, which highlights

the final technical contribution listed in Section 3.1. For details on how the MFC was functionalized with self-sensing capabilities, please see [37].

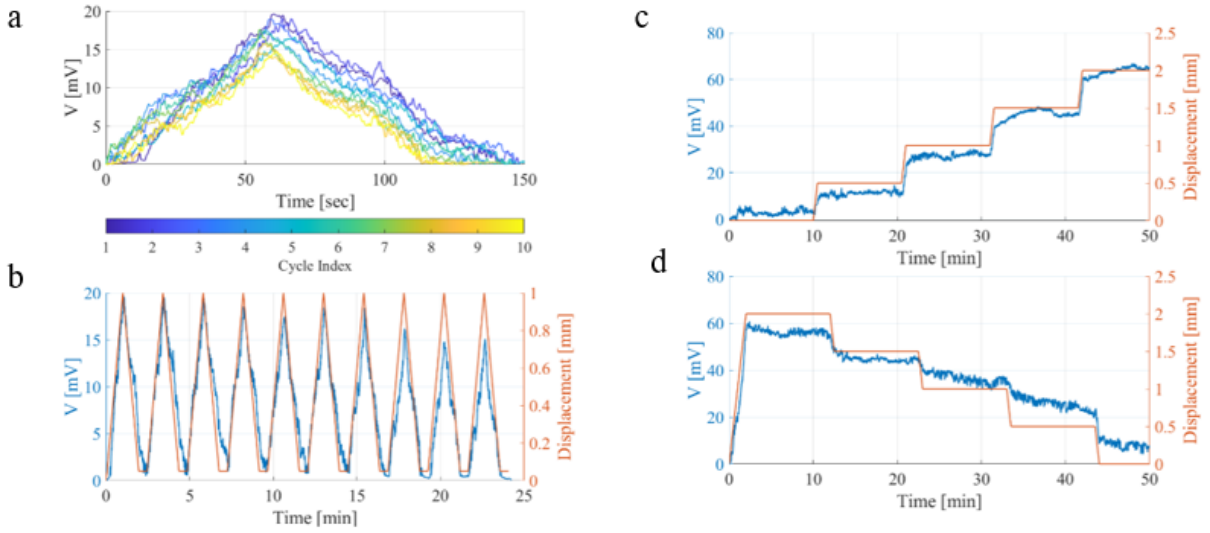

Figure 3.8: The measured bridge voltage during step-wise and cyclic loading and unloading taken from [37] ©2021 IEEE. **a)** Bridge voltage response during ten cycles. **b)** Bridge voltage response and applied displacement. **c)** Bridge voltage response during step wise increase of applied displacement. **d)** Bridge voltage response during step wise decrease of applied displacement.

3.5 Kirigami vs Honeycomb Comparison

In order to evaluate the trade-off between stiffness and weight in a nondescript aerial-aquatic structure, I use a modified version of the material selection indices presented by Ashby [54]. This material selection method was initially created to provide a framework for selecting a material, given a specific constraint. Details of how these indices are derived can be found here [54], but the basic premise is as follows. Given a certain loading condition, select a design constraint such as maximizing strength or minimizing stiffness. Then, select an objective, such as minimizing the mass. Finally, establish which geometric variables are "free" or within the control of the designer, and rearrange the equation for your constraint such that you eliminate the free variable. Using the relative densities and young's moduli derived earlier in this chapter and aiming to minimize both mass and stiffness while leaving the structure's cross-sectional area as the free variable, one arrives at the material selection indices given by equations Eq. (3.8) and Eq. (3.9). The material with the largest value of M will be the

material with the lowest mass and stiffness in the given loading conditions.

$$M_{uniaxial} = \frac{1}{\bar{E}\bar{\rho}} \tag{3.8}$$

$$M_{bending} = \frac{1}{\bar{E}^{1/2}\bar{\rho}} \tag{3.9}$$

Using these indices, one finds that for the vast majority of geometries, loaded uniaxially, horizontal slit kirigami structures are preferable while in bending, the vast majority of diamond celled honeycombs structures are preferable when both stiffness and weight are to be minimized. This is shown in Fig. 3.9. Only ratios of $t/l < 0.2$ are shown because all honeycomb theory based models break down for larger ratios of t/l. This is because the cell walls can no longer be approximated well as beams for larger ratios.

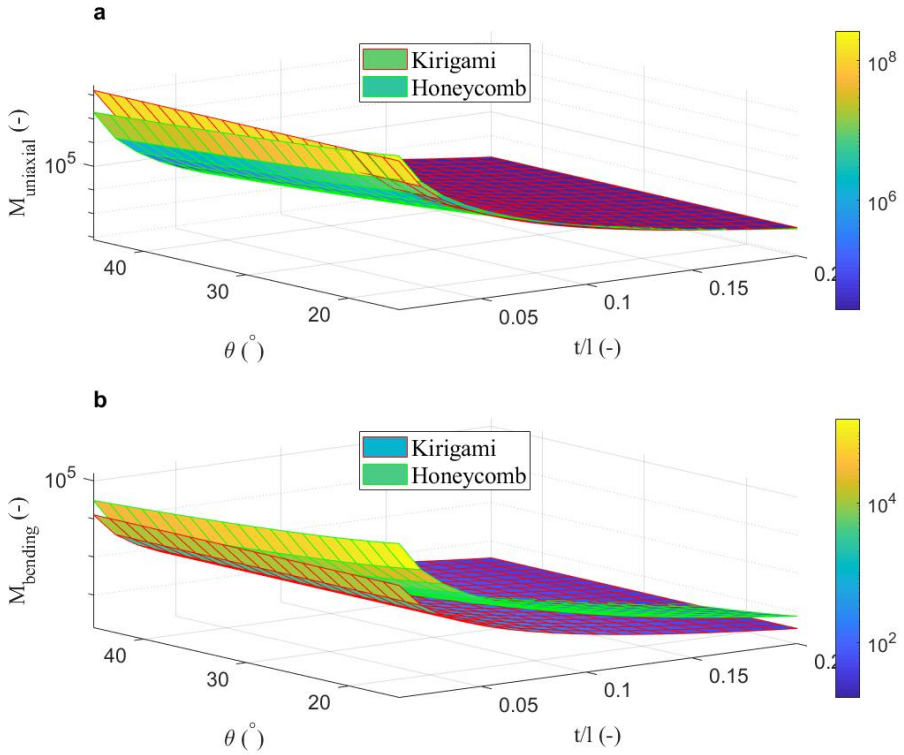

Figure 3.9: Plots showing values for Ms for diamond celled honeycombs and horizontal slit kirigami structures. The axes for θ and t/l are linear while the axes for the Ms are on a log scale.**a)** Values of $M_{uniaxial}$ for different values of θ and t/l. **b)**Values of $M_{bending}$ for different values of θ and t/l.

3.5.1 Conclusion

In this chapter I presented 1D analytical modeling and mechanical testing of diamond celled honeycomb and horizontal slit kirigami structures made from microfibrillated cellulose (MFC). These structures were then used in a strain sensing structure intended to provide feedback for control of a camber-morphing wing. In our strain sensor, we reduced the stiffness of the proposed structure by a factor of up to 19000. I then compared the properties of diamond celled honeycomb and horizontal slit kirigami structure in both bending and uniaxial loading in order to determine when one may be more suitable than the other for a particular flexible aerial-aquatic structure. This modeling ultimately informs the choice of structure used in Chapter 4.

3.5.2 Future Work

This work leads to two future avenues of research. Fabian Wiesemuller is interested in using these structures for biodegradable aerial robots and will continue to evaluate their usefulness for both sensing and actuation tasks within that context. I use the work from this chapter to design a camber morphing wing that is intended to be used for both flying and sailing in a vehicle similar to the SailMAV, a robot which I discussed briefly in Chapter 1. Chapter 4 will draw on the homogenization and kirigami vs. honeycomb comparison work that I have done in this chapter in order to design and model a flexible and shape-locking camber morphing wing.

Chapter 4

Shape-locking, Bidirectional, Bending, Structures with Diamond Celled Honeycombs

4.1 Introduction

In this chapter, I present a process for designing and manufacturing light-weight, shape-locking, bidirectional, bending and structures (SLBBS) that can be used for aerial-aquatic robots as well as a wide variety of other soft robotics applications. As discussed in Chapter 3, diamond celled honeycombs are better than horizontal slit kirigami structures for bending applications where the designer wants to minimize both weight and stiffness. As the primary focus of my research is structures for aerial-aquatic robots, for which reduction of weight is an essential design parameter, the structures I discuss here utilize diamond celled honeycombs. However, similar analysis techniques could be used to design a structure which uses horizontal slit kirigami structures in place of diamond celled honeycombs, should other design criteria be more relevant.

In this chapter, I first extend the work discussed in Chapter 3, by developing a 3D analytical model for diamond celled honeycombs which allows us to fully homogenize the mechanical properties of the structure and describe it as a new material with linear elastic material constants. I then use that model, in conjunction with existing laminar jamming models, to design the internal structure of a bidi-

rectional camber morphing wing intended to be used for both flying and sailing. It acts as an example of a SLBBS that I then use to explain the design and manufacturing methods for such structures. This wing concept could be used for aerial locomotion, as a means of providing lift and controlling the orientation of an aerial vehicle, but it can also be used for aquatic locomotion, acting as a morphing sail that allows the vehicle to travel at the water's surface. This is illustrated in Fig. 2.1, where such a wing is used by both an aerial and aerial-aquatic robot for maneuvers and efficient flight, and by an aerial-aquatic robot for sailing.

The scientific and technological contributions presented in this chapter are as follows:

- 3D homogenization of diamond celled honeycombs and validation of that model through experiments and FEM
- Analytical and FEM composite models that demonstrate the mechanics of stacked honeycomb and laminar jamming structures [1]
- Design of honeycomb and laminar jamming structures for bidirectional, tendon-driven, shape-locking, bending structures
- Manufacturing methods for bidirectional, bending, and shape-locking honeycomb based structures

4.2 Design, Analysis, and Manufacturing

In this section, I describe the design and manufacturing process for SLBBS. This process for designing an SLBBS is outlined in Fig. 4.1. The process is broken up into three main steps: problem definition, design, and manufacturing. Each of the sub-steps is designated by a yellow box, and the text in red within those boxes summarizes how this process was used to design the camber morphing wing designed in this chapter. This section is structured in order to walk the reader through this design process, while also providing details on the relevant theory and modeling techniques used in the design of these structures.

[1] It is worth noting that the analytical composite models derived here are an application of existing plate theory. A solution to variable thickness composite plates could not be found in the literature, but the solution presented here is more of a technical contribution than a scientific one as it does not involve the presentation of new theory.

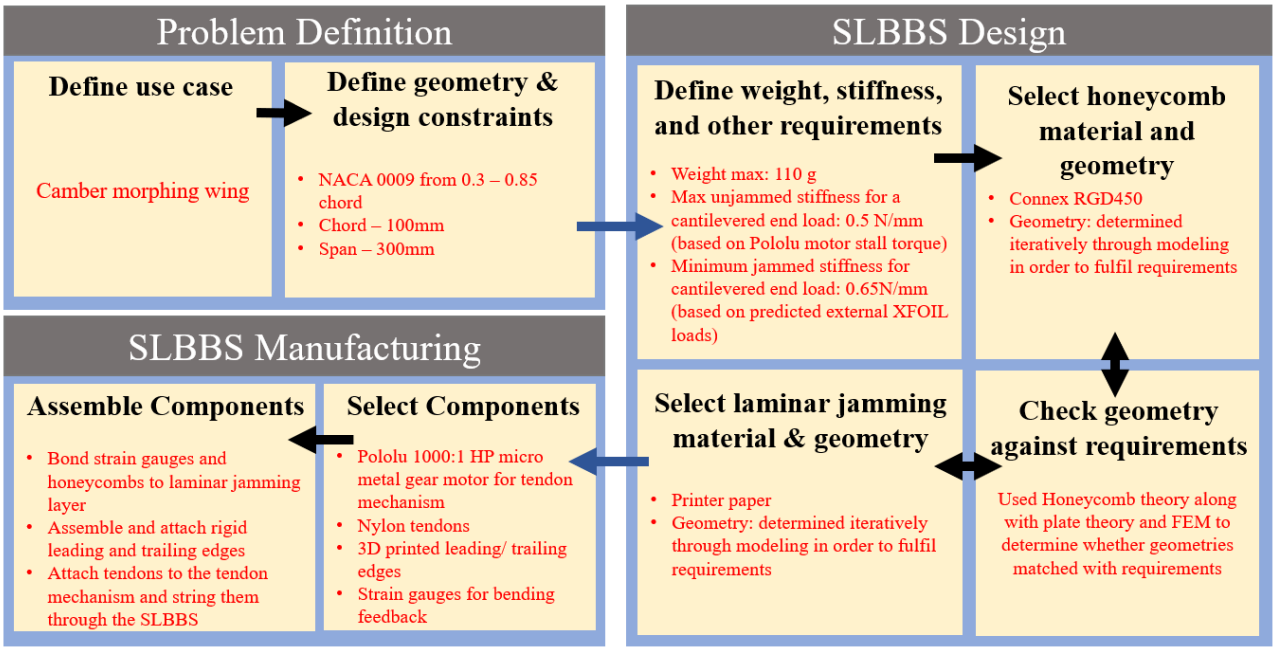

Figure 4.1: SLBBS design methodology. The blue and gray blocks outline the three high-level design phases. The black titles within the yellow boxes outline the sub-steps of those high-level design phases. The red text explains how the SLBBS used in the morphing wing described in this chapter was designed, built, and tested using this methodology.

4.2.1 Structure Geometry and Components

These structures consist of four main components: two diamond celled honeycombs, a laminar jamming layer, a tendon mechanism, and a vacuum pump. The laminar jamming layer is sandwiched between both diamond celled honeycombs and acts as a strain limiter which forces the entire structure to bend when the diamond celled honeycombs are loaded in either tension or compression. The bending motion is controlled through a tendon-driving mechanism. Each diamond celled honeycomb has a series of tendons running through it, which are all connected to a single shaft. When that shaft is rotated, one diamond celled honeycomb is loaded in tension, while the other is loaded in compression, and, with the strain limiting properties of the laminar jamming layer, the entire structure bends. In addition to acting as a strain limiter, the laminar jamming layer also allows the structure to lock itself into particular configurations and is driven by the on-board vacuum pump. This capability is particularly useful for a morphing wing, as certain airfoil shapes may be desirable for long periods of time during flight. By using laminar jamming, the shape of the structure can be locked in a matter of seconds, and by using a valve to hold that vacuum pressure, the structure can remain in that shape with minimal effort from the on-board actuators. While this does require the additional weight of

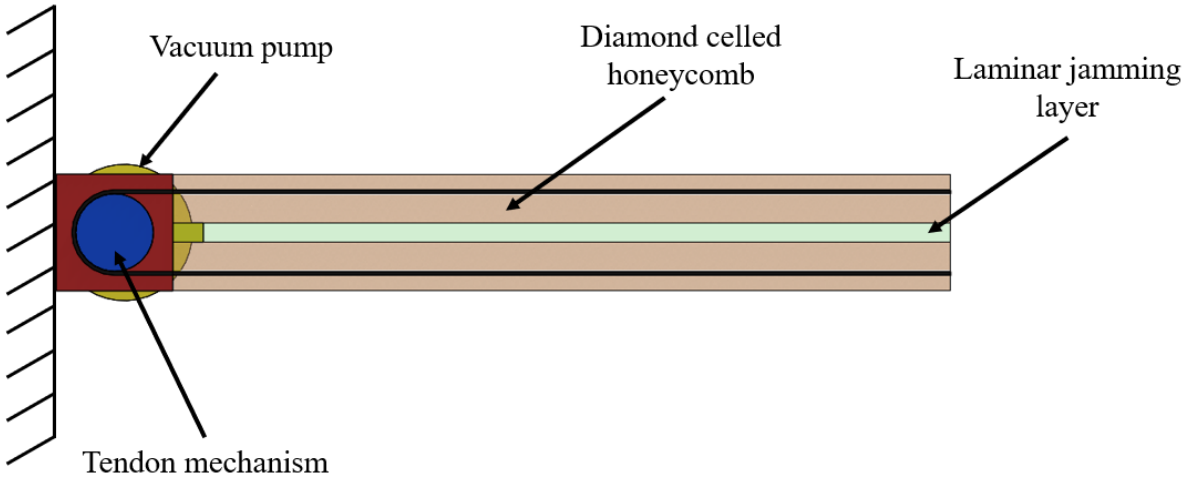

Figure 4.2: SLBBS component diagram.

an on-board pump, the pump used here (KNF NMP 03) only adds 11 g to each wing. If two such wings were added to the current SailMAV, it would require less than 1 W of additional power to fly the vehicle with that added mass. However, operating the tendon mechanism continuously in both wings would require between 2 W - 4 W, depending on the desired camber, making the added weight of the pump worth the overall decrease in energy expenditure during flight.

An overview of the various components can be found in Fig. 4.2. In this figure, the vacuum pump and motor driving the tendon mechanism are attached to the side of the wing. In a fully integrated system, these components would be housed in the robot's fuselage to prevent additional drag. In the wind tunnel testing described in Section 4.3.2, these components are outside the wind tunnel and separated from the model by the splitter plates for this reason.

For this particular morphing wing application, I use a SLBBS as the wing's midsection. The tendon-driving mechanism is held in place by a rigid leading edge and each of the tendons are tied to a rigid trailing edge. The tube that connects the laminar jamming section to the pump also runs through the leading edge. In the neutral position, the wing has a NACA 0009 profile, its chord is 100 mm, its span is 300 mm, and the entire wing, including the motor driving the tendon mechanism and the pump weighs 104 g. In order to be integrated into the next iteration of the SailMAV, the wing needed not exceed a weight of 110 g. The SLBBS covers the entire span of the wing, and thus has a width of 300 mm, but it only covers 55% of the chord, starting at 30% chord and ending at 85% chord, and

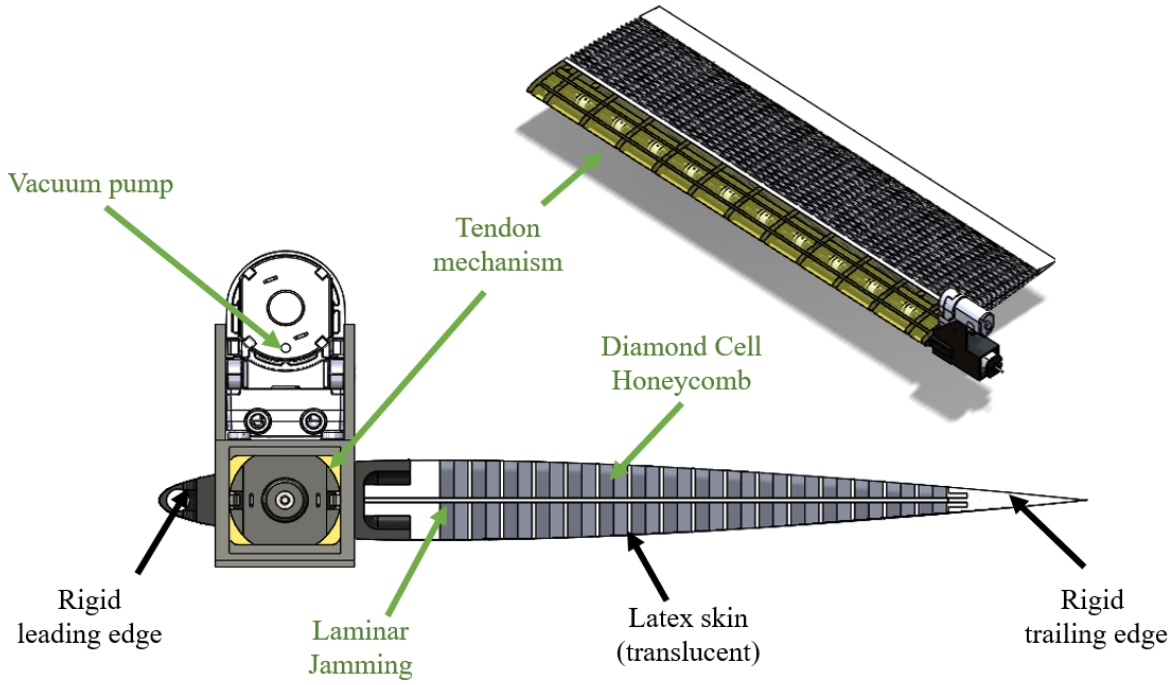

Figure 4.3: Camber morphing component diagram. The portions of the SLBBS are labeled in green. The remaining parts of the wing are labeled in black.

thus has a length of 55 *mm*. As the wing's midsection must also be a smooth aerodynamic surface, I covered the SLBBS in a thin layer of pre-tensioned latex. Fig. 4.3 is a schematic of the wing.

Table 4.1: Morphing Wing Properties

Property	Value
Chord	100 *mm*
Span	300 *mm*
Latex skin thickness	0.15 *mm*
Neutral profile	NACA 0009
Weight	104 *g*

The latex sheet is 0.15 *mm* thick which is thin relative to the thickness of the SLBBS. This is done so that the hyperelastic mechanical properties of the material have a very small affect on the overall behavior of the SLBBS. As such, the mechanical behavior of the latex is neglected in the analytical model presented here and the effectiveness of that model in accurately describing the SLBBS with a latex skin attached is discussed in Section 4.3.

4.2.2 3D Diamond Cell Honeycomb Homogenization

The primary goal in modeling the honeycomb structure is to homogenize it such that it can be treated as a block of material with certain mechanical properties rather than modeling the behavior of each cell of the structure individually. Almost all honeycomb structures can be modeled as orthotropic materials using the following constitutive relations.

$$\begin{bmatrix} \sigma_{11} \\ \sigma_{22} \\ \sigma_{33} \\ \sigma_{23} \\ \sigma_{31} \\ \sigma_{12} \end{bmatrix} = \begin{bmatrix} C_{1111} & C_{1122} & C_{1133} & 0 & 0 & 0 \\ C_{2211} & C_{2222} & C_{2233} & 0 & 0 & 0 \\ C_{3311} & C_{3322} & C_{3333} & 0 & 0 & 0 \\ 0 & 0 & 0 & C_{2323} & 0 & 0 \\ 0 & 0 & 0 & 0 & C_{3131} & 0 \\ 0 & 0 & 0 & 0 & 0 & C_{1212} \end{bmatrix} \begin{bmatrix} \varepsilon_{11} \\ \varepsilon_{22} \\ \varepsilon_{33} \\ \varepsilon_{23} \\ \varepsilon_{31} \\ \varepsilon_{12} \end{bmatrix} \tag{4.1}$$

For any material, the matrix $\mathbb{C}$ can also be written in terms of the matrix $\mathbb{S}$ where

$$\mathbb{S}^{-1} = \mathbb{C}. \tag{4.2}$$

Generally, it is much easier to calculate $\mathbb{S}$, than it is to calculate $\mathbb{C}$, so $\mathbb{C}$ will be found from the following formula for $\mathbb{S}$ for an orthotropic material.

$$\begin{bmatrix} S_{1111} & S_{1122} & S_{1133} & 0 & 0 & 0 \\ S_{2211} & S_{2222} & S_{2233} & 0 & 0 & 0 \\ S_{3311} & S_{3322} & S_{3333} & 0 & 0 & 0 \\ 0 & 0 & 0 & S_{2323} & 0 & 0 \\ 0 & 0 & 0 & 0 & S_{3131} & 0 \\ 0 & 0 & 0 & 0 & 0 & S_{1212} \end{bmatrix} = \begin{bmatrix} \frac{1}{E_1} & -\frac{\nu_{21}}{E_2} & -\frac{\nu_{31}}{E_3} & 0 & 0 & 0 \\ -\frac{\nu_{12}}{E_1} & \frac{1}{E_2} & -\frac{\nu_{32}}{E_3} & 0 & 0 & 0 \\ -\frac{\nu_{13}}{E_1} & -\frac{\nu_{23}}{E_3} & \frac{1}{E_3} & 0 & 0 & 0 \\ 0 & 0 & 0 & \frac{1}{G_{23}} & 0 & 0 \\ 0 & 0 & 0 & 0 & \frac{1}{G_{31}} & 0 \\ 0 & 0 & 0 & 0 & 0 & \frac{1}{G_{12}} \end{bmatrix} \tag{4.3}$$

In order to determine each of the values of $\mathbb{S}$, the material constants for the honeycomb must be written in terms of the material properties of the solid from which the honeycomb is made.

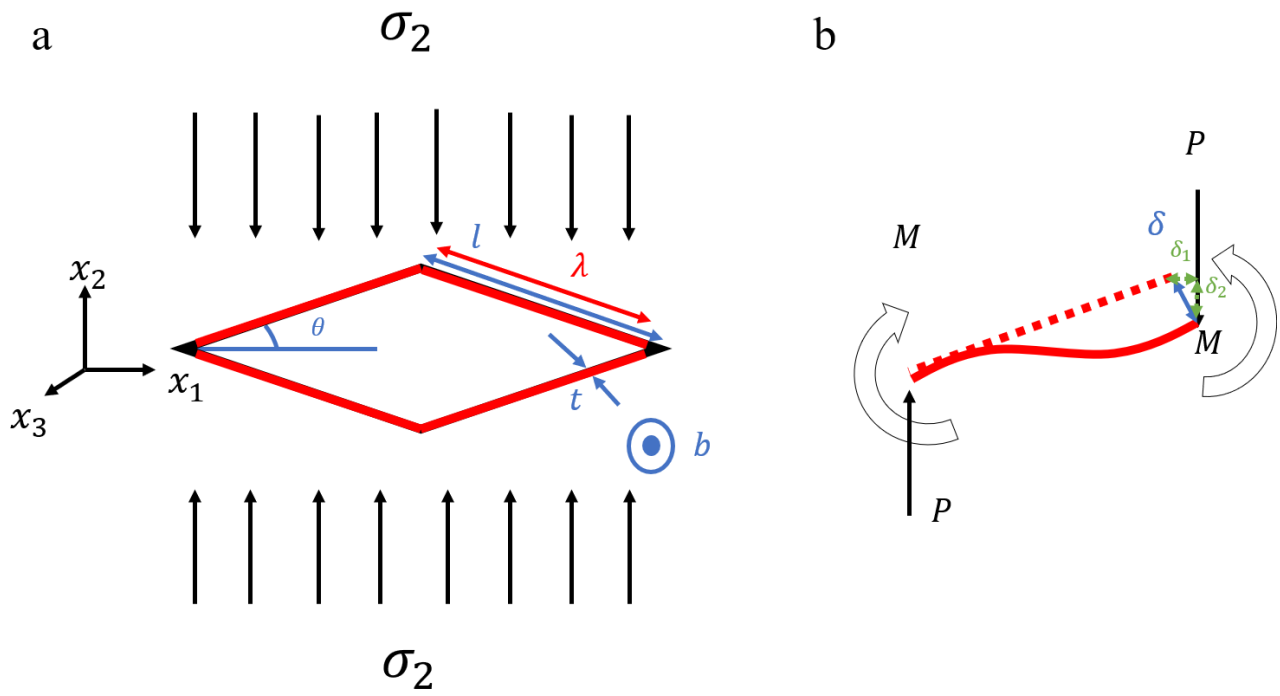

Figure 4.4: Modified version of Fig. 3.3. Here the diamond-cell is outlined in black, with beams of length Λ superimposed on top of that in red adapted from [37] ©2021 IEEE. The far field stress σ_∞ is now replaced with σ_2 per the coordinate system also shown in the figure. **a)** Loading condition. **b)** A single cell wall of length Λ under internal loads caused by far field stress σ_2.

In Plane Material Properties

This homogenization of the in-plane material properties presents a slightly modified version of the model I derived in Section 3.3.2. Here, I use the same honeycomb theory process on beams of length Λ, but I use the equations from Timoshenko beam theory rather than Euler-Bernoulli beam theory to calculate δ. This is because the original formulation will result in a singularity in the $\mathbb{S}$ matrix. Using Timoshenko beam theory adds an additional term which has almost no affect on the numerical values of E_1^* and E_2^*, but makes it so that $\nu_{12} \neq 1$ and $\nu_{21} \neq 1$, which makes $\mathbb{C}$ calculable. I depict a modified version of Fig. 3.3 here in Fig. 4.4 which shows the beam of length Λ superimposed on the diamond-celled honeycomb structure and the 3D coordinate system that I use for the remainder of this chapter.

Similar to the derivation in Chapter 3, the far field stress σ_∞ is replaced with σ_2 per the coordinate systems shown in Fig. 4.4. This far field stress is given by

$$\sigma_2 = \frac{P}{\Lambda b cos(\theta)} \tag{4.4}$$

and causes strains of

$$\varepsilon_{11} = \frac{\delta_1}{\Lambda cos(\theta)} \tag{4.5}$$

and

$$\varepsilon_{22} = \frac{\delta_2}{\Lambda sin(\theta)} \tag{4.6}$$

where δ_1 is the component of the beam deflection, δ, in the x_1 direction and δ_2 is the component in the x_2 direction. Summing the portions of the deflection that come from Timoshenko beam bending and axial deformation gives

$$\delta_1 = \frac{Psin(\theta)cos(\theta)\Lambda^3}{12E_sI}\left(1 + (1.4 + 1.5\nu_s))\frac{t^2}{\Lambda^2}\right) \tag{4.7}$$

and

$$\delta_2 = \frac{Pcos^2(\theta)\Lambda^3}{12E_sI}\left(1 + (2.4 + 1.5\nu_s + tan^2(\theta))\frac{t^2}{\Lambda^2}\right) \tag{4.8}$$

Plugging equation Eq. (4.8) into equation Eq. (4.6) and assuming a linear elastic material,

$$E_2^* = E_s\left(\frac{t}{\Lambda}\right)^3 \frac{sin(\theta)}{cos^3(\theta)}\left(\frac{1}{1 + (2.4 + 1.5\nu_s + tan^2(\theta))\frac{t^2}{\Lambda^2}}\right) \tag{4.9}$$

This also allows me to solve for the Poisson's ratio ν_{21}^*

$$\nu_{21}^* = -\frac{\varepsilon_{11}}{\varepsilon_{22}} = \frac{sin^2(\theta)}{cos^2(\theta)}\left(\frac{1 + (1.4 + 1.5\nu_s)\frac{t^2}{\Lambda^2}}{1 + (2.4 + 1.5\nu_s + tan^2(\theta))\frac{t^2}{\Lambda^2}}\right) \tag{4.10}$$

Going through this same process with applying a far field stress in the x_1 direction gives

$$E_1^* = E_s\left(\frac{t}{\Lambda}\right)^3 \frac{cos(\theta)}{sin^3(\theta)}\left(\frac{1}{1 + (2.4 + 1.5\nu_s + cot^2(\theta))\frac{t^2}{\Lambda^2}}\right) \tag{4.11}$$

and

$$\nu_{12}^* = \frac{cos^2(\theta)}{sin^2(\theta)}\left(\frac{1 + (1.4 + 1.5\nu_s)\frac{t^2}{\Lambda^2}}{1 + (2.4 + 1.5\nu_s + cot^2(\theta))\frac{t^2}{\Lambda^2}}\right) \tag{4.12}$$

When the structure is loaded in shear, there is no net deflection of the structure due to bending. The

formula for the shear modulus G^*_{12}, Eq. (4.13), is taken from Côté et al. who model each of the cell walls as beams in tension and compression. The reader is referred to [55] for details of the derivation.

$$G^*_{12} = \frac{E_s}{1 - {\nu_s}^2}\left(1 - \frac{1}{W/L} tan(\theta)\bar{\rho} sin^4(\theta)\right) \tag{4.13}$$

In, Eq. (4.13) W and L are the length and width of the actuator respectively,as depicted in Fig. 4.6. $\bar{\rho}$ is the relative density of the honeycomb given by $\bar{\rho} = \frac{2t}{lsin(2\theta)}$ as discussed in Section 3.2.

Out of Plane Properties

When loaded out of plane, the Young's modulus E^*_3 is simply the solid modulus E_s scaled by the area of the diamond which bears the load, and the Poisson's ratios ν^*_{31} and ν^*_{32} are the same as that of the solid ν_s.

$$E^*_3 = E_s \frac{1}{sin(\theta)cos(\theta)} \frac{t}{l} \tag{4.14}$$

$$\nu^*_{31} = \nu^*_{32} = \nu^*_s \tag{4.15}$$

The Poisson's ratios ν^*_{13} and ν^*_{23} can be found from the known reciprocal relations for orthotropic materials given by Gibson et al [21].

$$\nu^*_{13} = \frac{E^*_1}{E^*_3}\nu_s, \ \nu^*_{23} = \frac{E^*_2}{E^*_3}\nu_s \tag{4.16}$$

The out of plane shear moduli can be found through use of the theorems of minimum potential and complementary energy given by Sokolinkoff and McClintock et al [56, 57]. The minimum potential energy theorem can be used to find a lower bound for the shear moduli while the complementary energy can be used to find the shear moduli's upper bounds. However, for this geometry, both theorems give the same result, given in Eq. (4.17) and Eq. (4.18).

$$G^*_{13} = G_s tan(\theta) \frac{t}{l} \tag{4.17}$$

$$G_{23}^{*} = G_s cot(\theta)\frac{t}{l} \tag{4.18}$$

These equations are also in agreement with the material constants for hexagonal honeycomb with $h = 0$ [21] (where h is the length of the vertical cell wall in a hexagonal honeycomb). The reader is referred to Gibson et al. for details regarding the application of these energy theorems to honeycomb structures [21].

4.2.3 Laminar Jamming Modeling

As discussed in Section 2.3, a laminar jamming structure consists of a stack of sheets of material, with young's modulus E_l, which is compliant before the vacuum is applied and stiff after the vacuum is applied. The stiffness of that stack of material is increased by n^2 once the vacuum is applied, where n is the number of sheets of materials [44]. This is because the stack behaves like individual sheets of material layered on top of one another before pressure is applied and then behaves like a block of material after pressure is applied. This is explained graphically in Fig. 4.5. In order to replace the sheets of material with a block that has one young's modulus when it is jammed and another when it is unjammed, the jammed modulus will be n^2 times larger than the unjammed stiffness. Given this phenomenon, I describe the laminar jamming layer as a linear elastic material with Young's Modulus E_{lj} according to Eq. (4.19).

$$E_{lj} = \begin{cases} E_l, \text{ if jammed} \\ \frac{E_l}{n^2}, \text{ if unjammed} \end{cases} \tag{4.19}$$

where E_l is the young's modulus of a single sheet of laminar jamming material and n is the number of sheets of material.

4.2.4 Static Composite Model

In order to understand the mechanics of the SLBBS as a whole, I provide an analytical model which describes the SLBBS as a cantilevered plate of variable thickness made from a laminar jamming layer

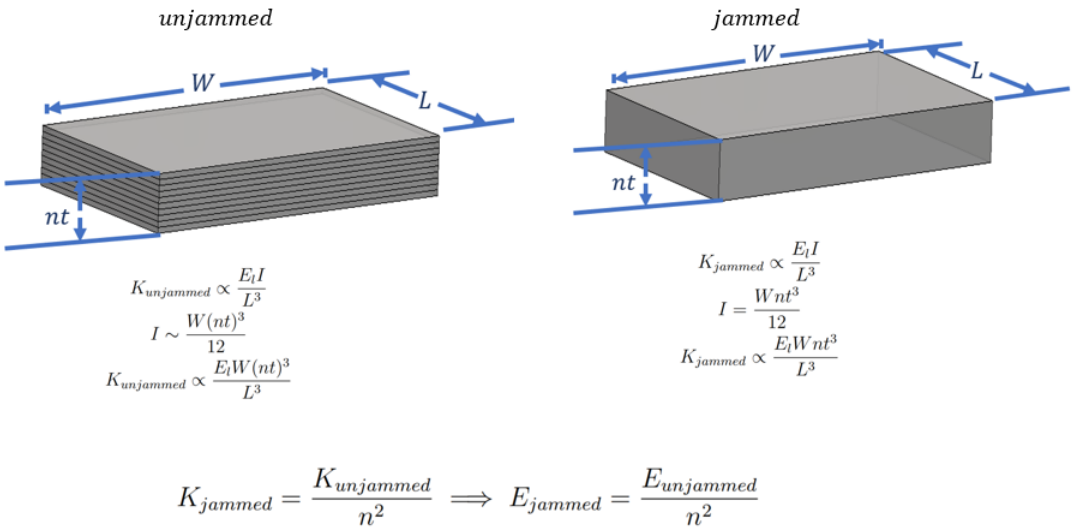

Figure 4.5: Laminar jamming working principle

sandwiched between two diamond celled honeycombs. I consider the plate to have a constant distributed load applied along its farthest edge, that is constrained such that the deflection of the plate does not vary along its width. In the actual SLBBS I construct, I impose this constraint on the deflection by reinforcing the rigid trailing edge with carbon fiber, so that variation of the deflection along the span of the wing is minimal. I also do this in the experimental setup discussed in Section 4.3.1 so that I can compare this model to how the physical system performs. This loading condition is depicted in Fig. 4.6.

While this is not the exact loading case that the SLBBS is under when actuated by the tendons, it does provide a loading case that can be easily tested with a mechanical testing machine. It also allows the designer to calculate a total bending moment that must be applied to the structure for a given deflection and then translate that into a torque requirement for the motor which drives the tendons.

Since the SLBBS example discussed in this chapter is part of a morphing wing, both its width and length are large relative to one another and relative to the SLBBS thickness, so a plate is the geometry that best simplifies this structure. However, if one were to construct a SLBBS with only one relevant dimension, it could be treated as a beam, which would yield a much simpler analytical model. In this section, I only consider deflections of up to 4 *mm*. This is because plate theory (and beam theory) is only considered to provide accurate linear approximations for small deflections [58]. According to the FEM simulations, the stiffnesses observed here do appear to remain the same for deflections far

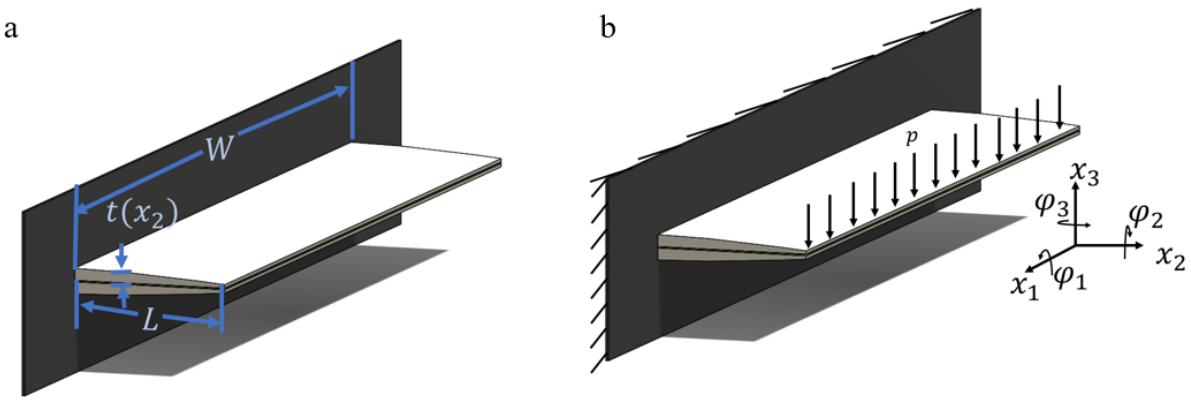

Figure 4.6: Composite model geometry, loading condition, and coordinate system. **a)** labeled geometry. **b)** loading condition and coordinate system.

outside that range, but this was not something that I investigated in detail through FEM or experiments as plate theory is only intended for modeling small deformations.

for a plate of variable thickness under a static, transverse load p,

$$D\nabla^2\nabla^2 x_3 = -p \tag{4.20}$$

describes the relationship between the load and the plate's deflection, where D is defined per equation Eq. (4.23) [58].

By applying Mindlin-Reissner Plate theory to our particular geomtery and loading condition, Eq. (4.20) can be solved with the following equations [59],

$$\mathcal{M}(x_2) = D_{22}(x_2)\frac{d\varphi_1}{dx_2} \tag{4.21}$$

and

$$-p = \frac{5}{6}A_{44}(x_2)(-\varphi_1 + \frac{dx_3}{dx_2}) \tag{4.22}$$

where,

$$D_{\alpha\beta}(x_2) = \int_{-t(x_2)}^{t(x_2)} C_{\alpha\alpha\beta\beta}(x_3)x_3^2 dx_3 \tag{4.23}$$

and

$$A_{\alpha\beta}(x_2) = \int_{-t(x_2)}^{t(x_2)} C_{\alpha\alpha\beta\beta}(x_3)dx_3 \tag{4.24}$$

.

$\mathcal{M}$ is the internal moment caused by the external distributed load p, which is

$$\mathcal{M}(x_2) = -p(L - x_2) \tag{4.25}$$

in this particular case. $t(x_3)$ is the SLBBS thickness, which is determined by the NACA 0009 profile. In both Eq. (4.23) and Eq. (4.24), $C_{\alpha\alpha\beta\beta}$ refers to material compliance. For values of x_3 that correspond to the honeycomb structure $C_{\alpha\alpha\beta\beta}$ is a term in matrix $\mathbb{C}$ per Eq. (4.1), Eq. (4.2) and Eq. (4.3). For values of x_3 that correspond to the laminar jamming layer $C_{\alpha\alpha\beta\beta} = E_{lj}$ per Eq. (4.19).

I solved this system of ODEs was numerically in MATLAB for various honeycomb geometries until I found one that was light enough to allow the wing to be integrated into an existing robot for future experiments and compliant enough to be deflected by a micro DC motor.

I then compared the analytical model to a FEM simulation in Abaqus/CAE 2020. There, I modeled the honeycomb structure as an orthotropic material with stiffness matrix $\mathbb{C}$ and modeled the laminar jamming layer as a sheet with young's modulus E_{lj}.I modeled the diamond celled honeycomb with hex elements. The mesh had 301 elements along the the SLBBS dimension L and 18 elements along W and 10 elements along $t(x_3)$. I modeled the laminar jamming layer as a midsurface shell with 101 elements along L and 172 elements along W. This mesh can be seen in Fig. 4.7.

A comparison of this analytical model with FEM is shown in Fig. 4.8. As shown in the plot, both the analytical and FEM models produce linear data with correlations of $r^2 = 1$. The slopes of these lines are given in Table 4.2.

Table 4.2: Analytical and FEM model stiffnesses

	Jammed stiffness (N/mm)	Unjammed Stiffness (N/mm)
Analytical model	0.6952	0.4445
FEM simulation	0.7367	0.4956

In order to select the proper motor, I estimated the loads that the structure should experience during flight so that I could determine the maximum amount of torque the motor would need to exert to change the wing's camber in flight. To do this, I ran a series of 2D simulations in XFOIL for the

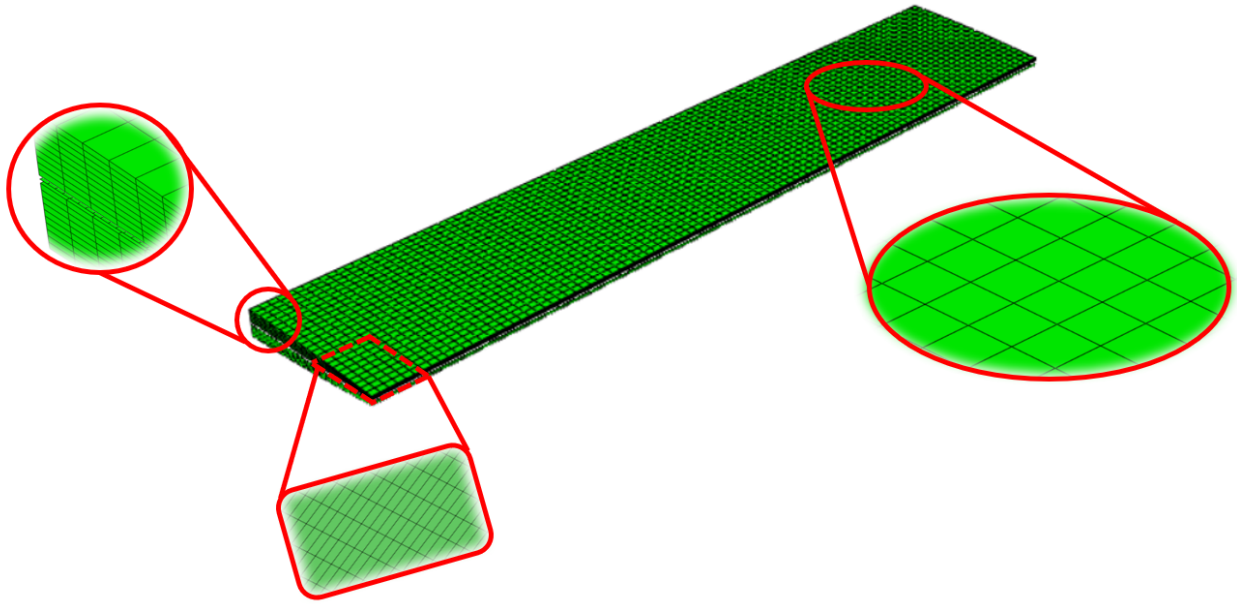

Figure 4.7: Mesh used for FEM model of SLBBS structure. The diamond celled honeycombs were modeled with Standard hex elements of quadratic order. That mesh had 301 elements along the the SLBBS dimension L and 18 elements along W and 10 elements along $t(x_3)$. The laminar jamming layer was modeled with shell elements. It was a midsurface with thickness $0.512\,mm$ that has 101 elements along it L and 172 elements along W.

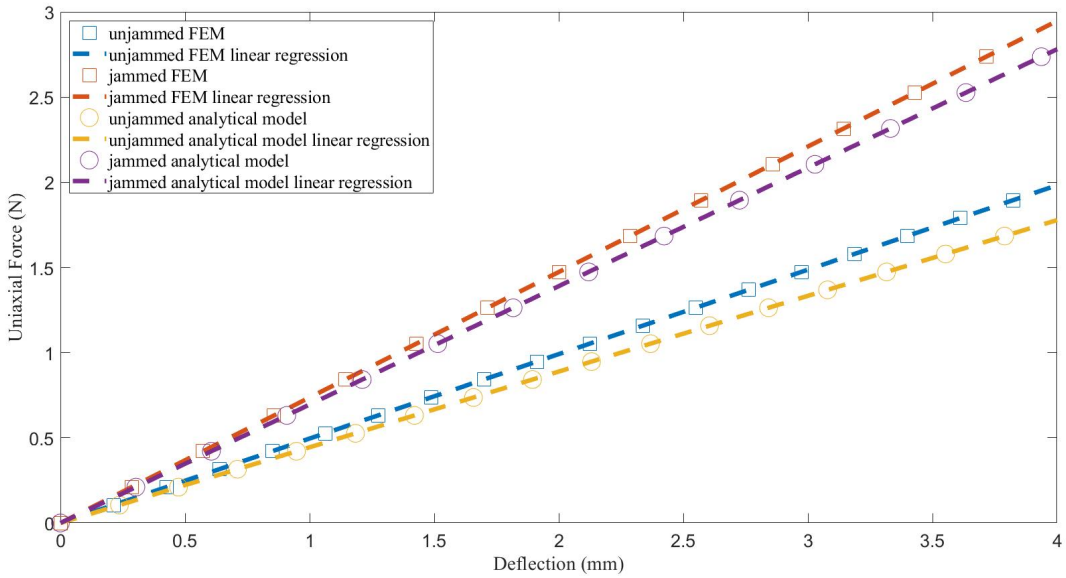

Figure 4.8: plate theory model plot with fem

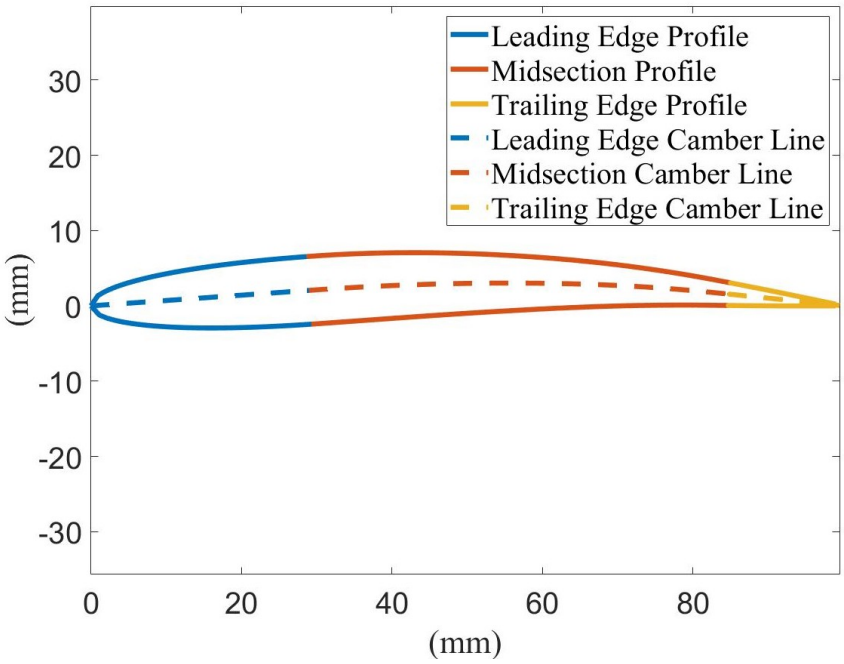

Figure 4.9: A predicted airfoil shape under a distributed load of $2N$ with no laminar jamming vacuum and a corresponding deflection of $4.5\,mm$.

various airfoil shapes that the wing is predicted to take on, and integrated the maximum pressure distribution over the width of the SLBBS to estimate the total additional force that the tendon mechanism may need to compensate for. I determined these airfoil shapes by solving the ODEs above for the total deflection of the SLBBS along its length. I then used that deflection curve, along with straight lines for the leading ad trailing edges, in order to construct the camber line for the wing. I then used the NACA airfoil shape formula to estimate the final airfoil shape that would result from such a camber line. A plot of one of these predicted airfoil shapes in shown in Fig. 4.9.

I also determined the number of sheets of laminar jamming material from these XFOIL simulations. I solved the same ODEs in MATLAB, with a definition of p that provided an equivalent load to what was predicted in XFOIL. The number of sheets of material was chosen such that the deflection of the trailing edge deflection would not exceed 0.5% chord when the laminar jamming vacuum was applied. This allows for minimal changes in the aerodynamic properties of the wing once the vacuum is turned on. Using this analysis, I arrived at a SLBBS with properties summarized in Table 4.3.

Table 4.3: SLBBS Properties

Property	Variable Name	Value
Length	L	$55\,mm$
Width	W	$300\,mm$
Thickness	$t(x_2)$	NACA 0009 profile from 0.3 chord to 0.85 chord
Diamond celled honeycomb cell wall angle	θ	15.4°
Diamond celled honeycomb cell wall thickness	t	$0.4\,mm$
Diamond celled honeycomb cell wall length	l	$6.5\,mm$
Diamond celled honeycomb base material E	E_s	$1.5\,GPa$
Laminar jamming base material E	E_l	$3.0\,GPa$
Number of laminar jamming sheets	n	5

4.2.5 Dynamic Modeling and Control

With the geometry of the wing now set, I then developed a dynamic model for the system in order to control wing tip deflection within the wind tunnel. A freely vibrating plate can be described by

$$D\nabla^2\nabla^2 x_3 + 2\rho t(x_2)\ddot{x}_3 = 0 \text{ [58]} \tag{4.26}$$

where ρ is the density of the SLBBS.

Defining the cantilevered bending stiffness derived in the previous sections as $\mathcal{K}$ and accounting for the width of the plate, Eq. (4.26) can be rewritten as

$$\mathcal{K}x_3 + 2\rho LWt(x_2)\ddot{x}_3 = 0 \tag{4.27}$$

which is essentially a model for a mass-spring system.

The flexible midsection of the wing is actuated by a tendon driven mechanism, as described in Section 4.2.1. Given that this mass-spring system is driven by a brushed DC motor connected to a shaft that drives a series of tendons running through the structure, friction within the bearings of this mechanism and between the tendons and the honeycomb structure cannot be ignored. As such, the entire

system is modelled as a mass spring damper system of the form

$$M\ddot{x_3} + b\dot{x_3} + \mathcal{K}x_3 = 0 \tag{4.28}$$

where M accounts for the mass properties of the SLBBS, the rigid trailing edge, and the motor's inertia, $\mathcal{K}$ is the same cantilevered bending stiffness used in Eq. (4.26) and Eq. (4.27), and b is a viscous friction term accounting for friction in the bearings and between the tendons and honeycomb structure.

Since the system was already fully designed and manufactured at this point in the analysis, a system identification experiment was performed to determine the constants in Eq. (4.28). A series of 10 6 V signals were sent to the motor driving the tendon mechanism and the step response was measured using the strain gauges embedded within the SLBBS. From there, deflection of the SLBBS was estimated from the strain measured by the strain gauges, and plots similar to the one shown in Fig. 4.10 were generated. The step response data was then fit to a curve matching the solution to Eq. (4.28) for each trial. The fit parameters were then averaged and used to determine constants in Eq. (4.28). From there, I designed a Proportional Integral Derivative Control (PID) controller using MATLAB control system designer to ensure a stable, closed loop, step response.

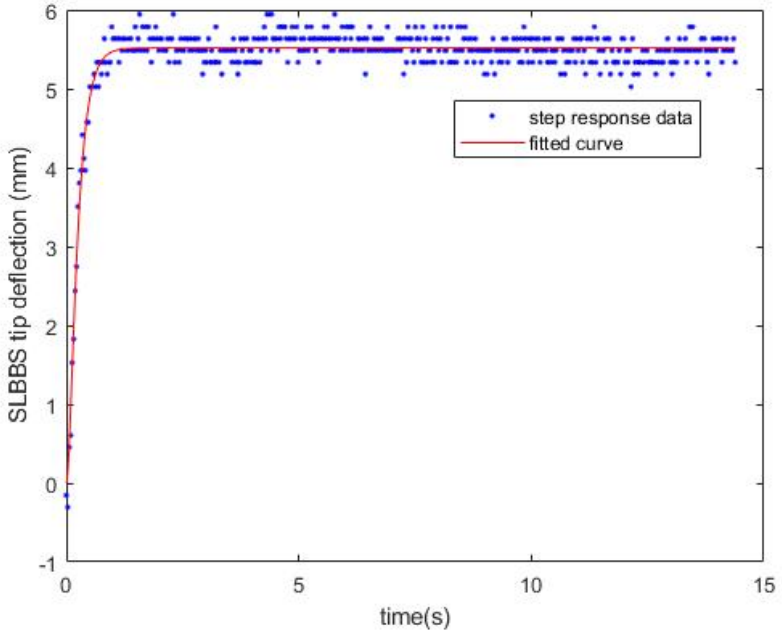

Figure 4.10: System identification example plot.

4.2.6 Manufacturing

As discussed in Section 4.2.1, the SLBBS consists of two diamond-celled honeycombs, a laminar jamming layer, a pump, and a tendon driving mechanism. The diamond-celled honeycomb, laminar jamming layers, and tendon driving mechanism are each manufactured independently, then the entire SLBBS is assembled.

The diamond-celled honeycomb was 3D printed with holes in it that allowed the tendons to be inserted. The SLBBS used in this morphing wing was printed from RGD450 on a Stratasys Connex 3 Objet 350. Once the honeycombs were printed, I bonded two strain gauges to the underside of each honeycomb with epoxy (Araldite Heavy Duty Epoxy Adhesive) so that the total bending strain could be measured.

The laminar jamming layer consisted of several sheets of paper which I cut to a fit the geometry of the SLBBS using a paper cutter. I then used an impulse sealer to make a vacuum bag which surrounded the paper on all sides, except for a small opening that allowed a silicone tube to be inserted. Once I inserted the silicone tube, that entrance was sealed using a heat gun and PTFE tape. Finally, I covered the laminar jamming structure in a double-sided adhesive film (3M 467 (7952) Double Linered Laminating Adhesive) and then applied a thin coat of epoxy (Araldite Heavy Duty Epoxy Adhesive) on top of that adhesive film.

I then placed the diamond celled honeycombson either side of the laminar jamming layer, clamped the entire stack together and allowed it to cure for $8\,hrs$. Once that section cured, I attached it to the rigid leading edge which holds the tendon driving mechanism. The geometry and manufacturing method for this rigid structure are entirely application dependent and are up to the designer. This piece simply must be designed such that it remains relatively undeformed under the loads applied to it by the tendon driving mechanism.

That tendon mechanism consisted of a series of pulleys mounted to a shaft which is then attached to a DC motor. I then used a needle and thread to run each tendon from the trailing edge end to the leading edge end of the top honeycomb. I then pulled the tendon through a hole in the corresponding pulley and then it threaded back through the honeycomb on the opposite side (from leading edge end to trailing edge end). Finally, I tied the tendons to the trailing edge side of both honeycombs and then

secured them with a small amount of epoxy.

With the SLBBS assembled, I then epoxied the carbon-fiber reinforced trailing edge to the end of the honeycombs. I then laser cut 0.15 mm thick sheets of natural latex rubber w and epoxied them in tension to both the leading and trailing edge of the wing, but did not bond them to the SLBBS itself. I designed the leading edge such that the laminar jamming vacuum tube, and the cables for reading the strain gauges all ran through the wing's leading edge to the rest of a robot. The vacuum pump, DC motor, and strain gauges were all connected to a uC. The entire system was controlled by the PID controller designed using the model developed in Section 4.2.5 which runs on the uC and uses the strain gauge data as feedback.

4.3 Results and Discussion

This section is divided into three parts. Section 4.3.1 describes an Instron experiment that was used to validate the mechanical model discussed in Section 4.2.4. Section 4.3.2 discusses the performance of the performance of the morphing wing as a whole in order to validate that the SLBBS discussed in this chapter functions for its particular application. Finally, Section 4.3.3 discusses design considerations for SLBBS used in hydrofoils. While the focus of this chapter is on the design of a SLBBS for a camber morphing airfoil, a camber morphing hydrofoil would also be a useful control surface for aerial-aquatic locomotion that could be designed using a similar process. As such, I discuss that case here for completeness.

4.3.1 Validation of Mechanical Model

The SLBBS was tested on an Instron 5969 Universal Testing Machine with a 50 kN load cell using the setup shown in Fig. 4.11. The entire system was pulled at a rate of 2 $\frac{mm}{min}$. I performed three different bending tests. The first test was with the latex skin bonded to the backboard and handle of the setup in tension and the laminar jamming layer turned off. The subsequent two tests were performed with the latex removed. One test was performed with the vacuum off and the other at 60 KPa of vacuum pressure.

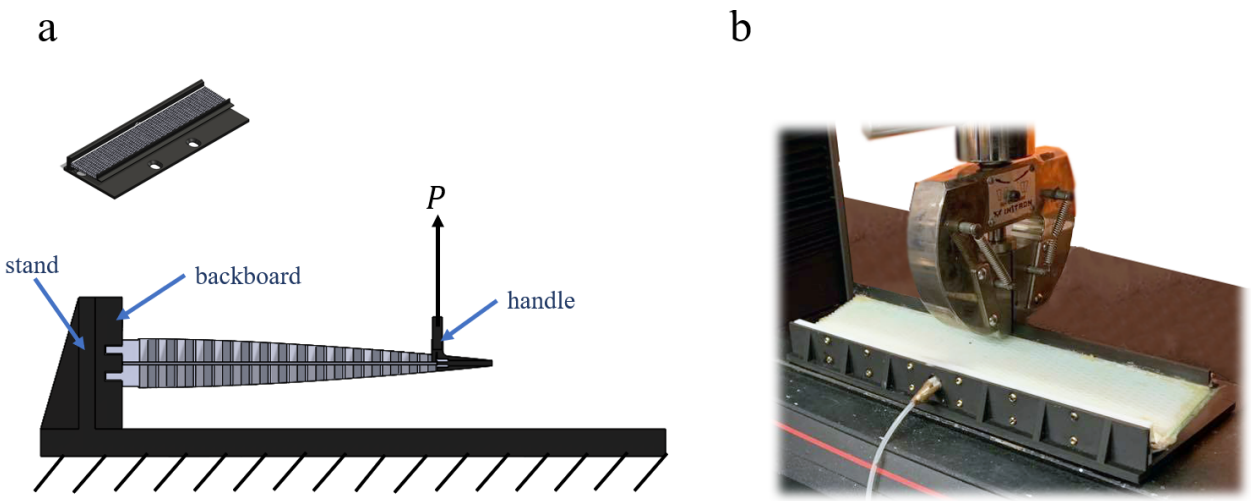

Figure 4.11: Instron test experimental setup design. **a)** Instron test setup schematic. The load P is applied by the Instron machine. An isotropic image of the setup is in the upper left corner. **b)** Photo of the actual SLBBS being tested in the Instron.

As shown in Fig. 4.12, both the FEM and analytical models are in good agreement with experimental data. By comparing Fig. 4.12a and Fig. 4.12b, one can also see that the latex skin appears to have very little impact on the overall stiffness of the structure. An instron test with vacuum applied and latex skin attached was not performed as the test with no vacuum applied and latex skin attached already indicates that the latex skin has little to no impact on the overall stiffness of the structure. In order to confirm this, I performed a t-test and concluded, with 95% confidence, that there was no statistically significant difference between the data produced by the bending tests conducted with and without the latex skin. This means that the models discussed in Section 4.2.4 can still be used for design purposes, so long as the hyperelastic skin used is thin relative to the thickness of the SLBBS. The measured stiffnesses from the three tests are given in Table 4.4, and are very similar to the stiffnesses predicted by the FEM and analytical models. This is shown graphically in Fig. 4.12 and in Table 4.4 where the largest percent difference in stiffness between the measured value and either the analytical or FEM models is 8.5%.

4.3.2 Wind Tunnel Testing

The purpose of this experiment is to show that the SLBBS discussed in this chapter functions as the flexible midsection of a camber morphing wing. The SLBBS is capable of deflecting from $\pm 10\,mm$. However, I only ran the experiment from $0\,mm$ - $10\,mm$ of defection because the remainder of the

Table 4.4: Bending test data from Instron experiments. **a)** bending test conducted under no vacuum with no latex skin. **b)** bending test conducted under no vacuum with latex skin. **c)** bending test conducted under 60KPa vacuum pressure with no latex.

Conditions	Stiffness (N/mm)	r^2	Analytical Model % difference	FEM Simulation % difference
No vacuum no latex	0.4595	0.9965	3.4%	-7.3%
No vacuum with latex	0.4821	0.9947	8.5%	-2.7%
60 KPa vacuum no latex	0.6809	0.9943	-2.6%	-7.6%

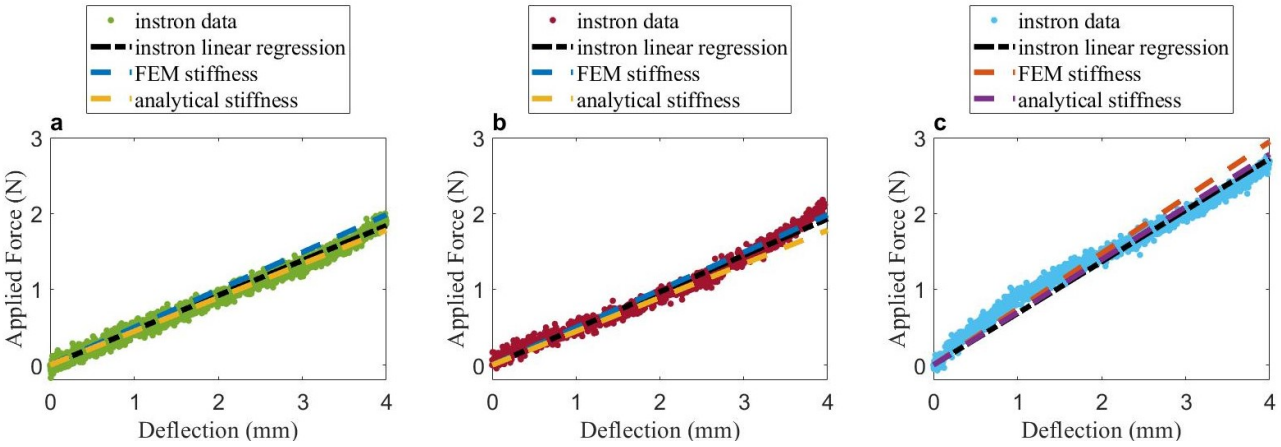

Figure 4.12: Instron test data compared to analytical and FEM models

deflection range should produce symmetrical results.

Fig. 4.13 shows the setup used for this experiment. The wing was mounted between two splitter plates, the bottom of which was flush with the wind tunnel floor. The disk was mounted directly to the top of a load cell (ATI IP68 SI-130-10). The bottom of that load cell was mounted to a disk that was free to rotate on a bottom plate which was connected directly back to the floor of the wind tunnel. The wind tunnel was run at 7 m/s (which corresponds to a Re of 47600) and forces were recorded as the wing deflected from 0 mm - 10 mm at AoA ranging from -12° - 12° at 1° increments.

I then used this data collected from the wind tunnel experiment to produce the plots shown in Fig. 4.14. After the test was completed, I removed the wing from the setup so that the lift and drag contributions of the splitter plates and splitter plate supports could be measured separately and subtracted from the data.

As shown in Fig. 4.14b, there is a small increase in C_D at very small angles of attack. This is in agreement with many other wind tunnel experiments conducted at low Re, and is likely caused by a

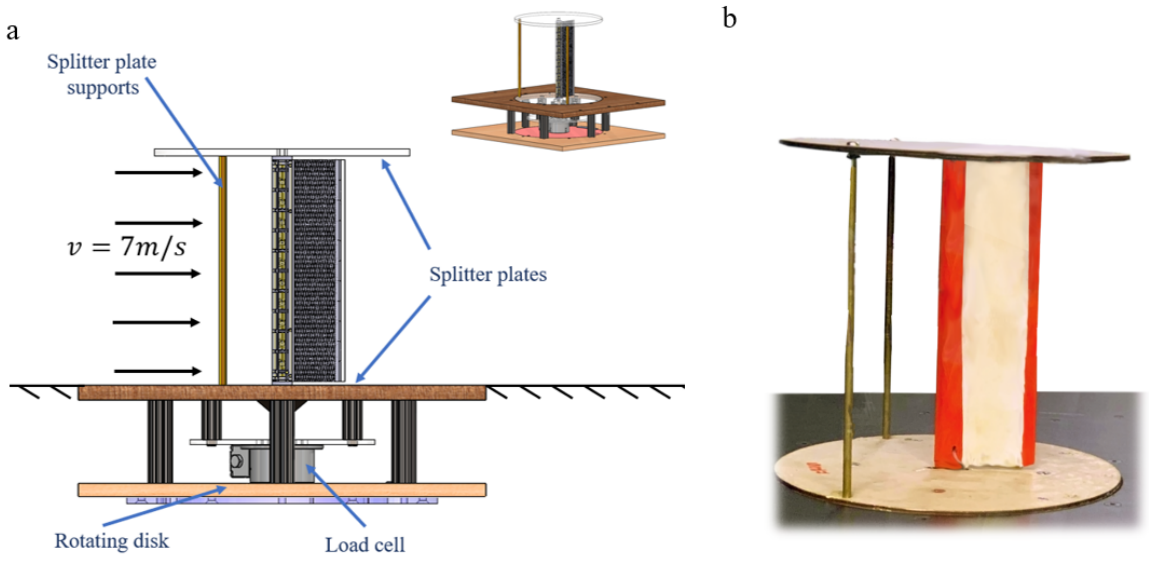

Figure 4.13: Wind tunnel experiment setup diagram. **a)** Wind tunnel setup schematic. The image in the upper right corner is an isotropic view of the entire setup. **b)** Photo of the actual wing being tested in the wind tunnel.

separation bubble which separates laminar and turbulent flows at the leading edge of the wing [60]. In order to determine how the wing performs at higher *Re* and at a larger range of AoA, more wind tunnel tests must be conducted.

For comparison, I conducted a series of simulations in XFOIL for a NACA 0009 airfoil with a trailing edge flap at the same *Re* as the wind tunnel experiments (*Re* = 47600). The flap takes up 25% of the wing's chord which is within typical sizes for a flap on a traditional fixed wing vehicle [19]. In simulation, I varied the AoA from 12^o to -12^o in 1^o increments and varied the deflection of the flap from 0 mm - 10 mm in 1 mm increments. The efficiency of the SLBBS morphing wing has a higher aerodynamic efficiency than the traditional flap design in 68% of configurations. In its most efficient configuration, it also produces more than 1.25× as much lift as the traditional flap in its most efficient configuration.

4.3.3 Use of Shape Locking Bidirectional Bending Structures for Hydrofoils

As discussed in Section 4.1, the morphing wing described in this chapter is an airfoil designed to be used for flying and sailing on a vehicle similar to the SailMAV. This allows the vehicle to perform

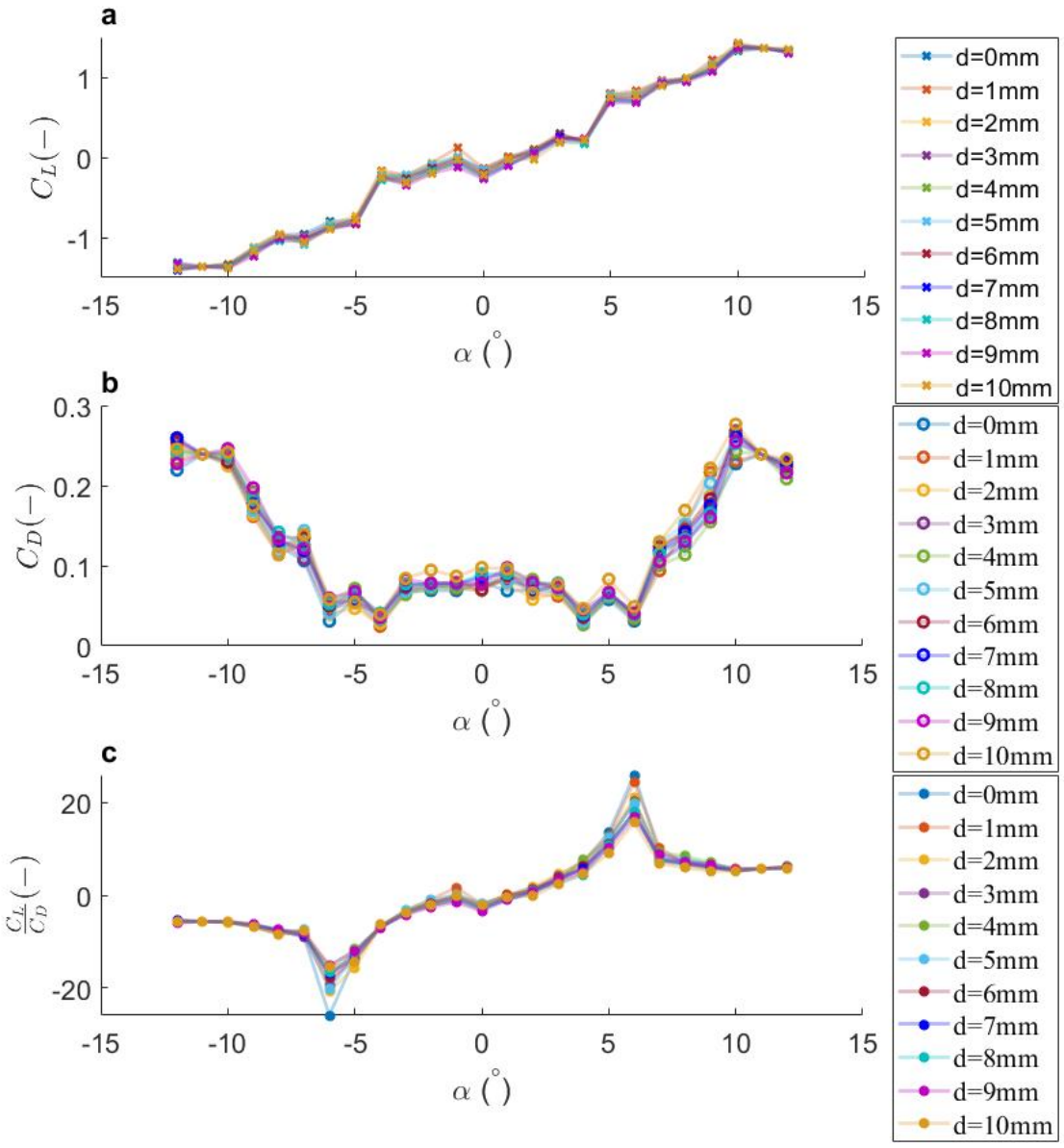

Figure 4.14: Morphing wing performance plots. **a)** Lift coefficient vs. AoA. **b)** Drag coefficient vs. AoA. **c)** Aerodynamic Efficiency (Lift/Drag coefficients vs. AoA).

aerial-aquatic locomotion by both flying and sailing on the water's surface, but does not require that the wing ever enter the water. However, the same general principle of using a SLBBS as the flexible midsection of a camber morphing wing could be applied for design of a hydrofoil as well. Given that it is certainly possible for a different type of aerial-aquatic robot to require morphing hydrofoils as part of its locomotion strategy, I will discuss here some of the differences in loading conditions between travel in air and water and the subsequent design considerations that must be made in order to account for that.

As mentioned in Chapter 1, one of the biggest differences between a robot moving through air and water is differences in *Re* between the two fluids. Given the differences in density and viscosity between air and water, if you were to have the same wing moving at the same speed in either fluid, the *Re* would differ by more than an order of magnitude. As a result, the pressures that the wing experiences varies greatly depending on the fluid.

To illustrate this point, Fig. 4.15 shows CFD of a NACA 0009 (the profile of the wing described here with no change in camber) in both air and water at $7\,m/s$. In order to design a hydrofoil meant to function under these conditions, the same general design process and modeling could be conducted, especially given that the XFOIL simulations used to calculate the required stiffness of the structure could be run for either air or water. However, the geometry of the honeycomb and number of sheets of laminar jamming material required to sustain these loads would vary greatly.

If the hydrofoil were only intended for aquatic locomotion, this would not be of much concern, as the weight of a submerisble vehicle can be orders of magnitude larger than the weight of an aerial vehicle of the same size. Submerisbles typically also require much smaller hydrofoils relative to their total size because they do not need to generate such large lifting forces. However, if the wing were intended for aerial-aquatic locomotion, it would need to be of a similar weight to the wing designed in this chapter. In order to do that, the size of the SLBBS could be dramatically reduced, such that more of the wing can be made from a rigid and lightweight material like foam or wood. The SLBBS would instead be much closer to the trailing edge of the wing as illustrated by the dashed yellow lines in Fig. 4.15c. Moving the SLBBS to this region would also greatly reduce the pressures acting on the SLBBS and reduce the required stiffness.

In the case of the airfoil, the pressures acting on the SLBBS are on the order of 1 *Pa* - 5 *Pa*. However,

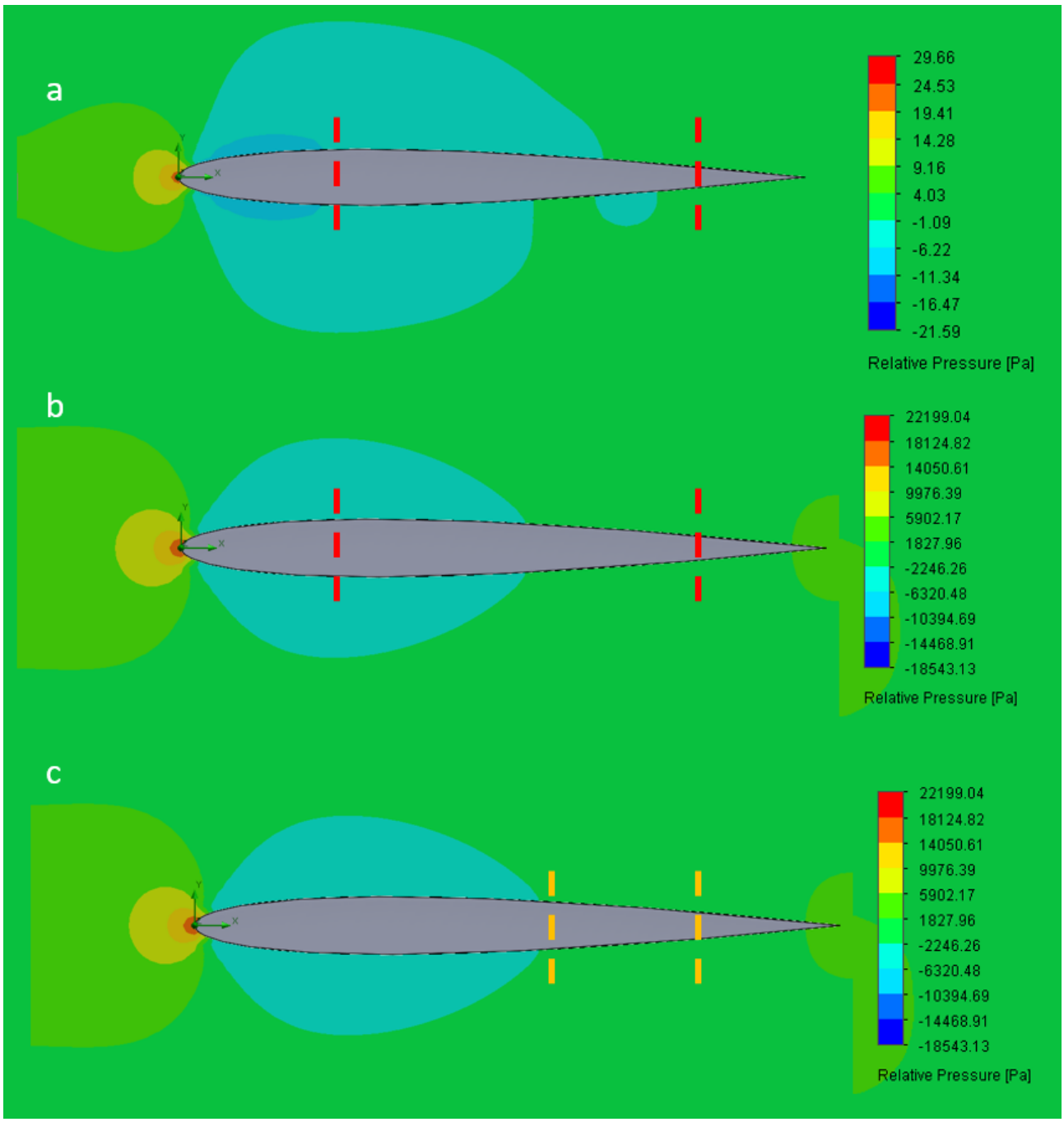

Figure 4.15: CFD run for a NACA 0009 airfoil traveling at 7 m/s in both air and water showing the fluid pressure around the wing. The values for pressure reported are relative to atmospheric pressure. **a)** CFD in air. The dashed red lines represent the beginning and end of the SLBBS. The relative pressures range from 30 Pa to -22 Pa. **b)** CFD in water. The dashed red lines represent the beginning and end of the SLBBS. The relative pressures range from 22 kPa to -19 kPa.The dashed red lines represent the beginning and end of the SLBBS. **c)** a duplicate of the study shown in b with a new suggested region for the SLBBS denoted with yellow dashed lines.

when placed under water, these pressures increase to a range of 100 Pa − 500 Pa. Consequently, deformation of the honeycomb in the x_3 direction is also of concern once the wing is placed under water, while this was not an important consideration when the SLBBS was in air. In designing a

hydrofoil, the engineer would use the out of plane material constants derived in Section 4.2.2 and validate that the pressures acting along the SLBBS do not cause the honeycomb to fail.

One other thing to note, which was not considered in the design of the airfoil described here, is varying the geometry of the honeycomb along the chord of the wing. While this would be much more difficult to model analytically, as the material constants would also vary as a function of x_2, one could also investigate varying the cell dimensions to minimize weight and vary the stiffness along the wing's chord to account for the much larger variations in external pressure. This could be done by trying different geometries in FEM simulations.

Finally, the last design consideration would be in choice of materials. Not only would the rigid leading edge be much larger and likely made from wood or a foam and carbon fiber composite, but the honeycomb itself should be printed from a different material. The RGD450 material used to create the honeycombs for the airfoil described in this chapter has a tendency to warp and even degrade after extend periods of exposure to water. A different plastic, like ABS, PLA, or another resin based 3D printing material with similar properties should be used in its stead.

4.4 Conclusion

In this chapter, I demonstrated how a diamond celled honeycomb based structure could be used as a morphing wing for an aerial-aquatic robot. Beyond that, I also presented the general idea of a SLBBS, which could have applications in soft robotics outside of aerial-aquatic robots. Overall, the analytical and FEM models presented in this chapter provide useful design tools for modeling these structures. The Instron tests serve to validate these models, and the wind tunnel experiments serve to show that a SLBBS can function as a flexible structure in an aerial-aquatic robotic component. Ultimately, the main conclusion that can be drawn from this work which addresses my primary research question is that diamond-celled honeycomb structures can provide a good light-weight structural option for flexible aerial-aquatic structures.

4.4.1 Future Work

For this particular project, the next major step would be integrating this wing into the next iteration of the SailMAV. This would serve to further validate whether or not a SLBBS can actually function as part of an aerial-aquatic robot. This would also answer larger questions about potential advantages to using camber morphing wings for sailing, as this is a sailing strategy observed in nature [15, 61], but has never been implemented in an aerial-aquatic robot. In addition to that, more wind tunnel testing could be conducted at higher wind speeds and at a larger range of AoAs so that it can be better characterized for higher flight speeds and for wind angles outside -12° - 12° which may be experienced during sailing.

Chapter 5

Conclusion

5.1 Summary of Achievements

As summarized in Table 1.1, I present several scientific and technical contributions ranging from analytical modeling to manufacturing techniques for flexible structures in this thesis. In Chapter 3, I derive 1D analytical models for diamond celled honeycomb and horizontal slit kirigami structures. I then validate those models with FEM and/or experiments and then provide a methodology for deciding between diamond celled honeycomb or horizontal slit kirigami structures depending on the application and loading condition. Using that methodology, in Chapter 4, I build a SLBBS using a diamond celled honeycomb and laminar jamming structures in a camber morphing wing intended for both flying and sailing. In doing this, I demonstrate that these structures can be used for aerial-aquatic robots and provide FEM and 3D analytical models to describe the mechanics of these SLBBS.

5.2 Applications

Aerial-aquatic robotics has become a relatively new and exciting area of research because tasks like water sampling and underwater surveying currently require lots of manual labor, and these tasks could be done more safely and efficiently with the aid of robots that function in both air and water. Unfortunately, most aerial-aquatic robots are not capable of completing an entire mission on their own. This is in part because many of them employ bio-inspired actuation strategies using rigid materials and

mechanisms, while their animal counterparts use flexible structures. By designing and modeling flexible honeycomb and kirigami structures for bio-inspired aerial-aquatic robots, my research begins to close that gap. Specifically, the bio-degradable, self-sensing structure discussed in Chapter 3 will be used in a bio-degradable camber morphing wing for an aerial-aquatic robot. Similarly, the structure discussed in both Chapter 3 and Chapter 4 was used to build a camber morphing wing that intended for both flying and sailing and can be integrated into the next iteration of SailMAV

In addition to having a wide variety of potential uses for aerial-aquatic robots, the work I discuss in Chapter 3 and Chapter 4 also provides a potential lightweight alternative for flexible structures needed in other soft robotics applications. For example, there are many hyperelastic actuators used in soft robotics for exoskeletons [62, 63], robotic jellyfish [64], and crawling robots[34]. Diamond celled honeycomb, horizontal slit kirigami structure, and SLBBS structures could all provide light weight alternatives for developing actuators for these applications, while also allowing researchers to take advantage of easily automated manufacturing techniques such as laser cutting and 3D printing.

5.3 Future Work

The work in this thesis demonstrates the efficacy of diamond celled honeycombs and horizontal slit kirigami structures structures for flexible components in aerial-aquatic robots. The most immediate next step would be development of a series of aerial-aquatic robots that use these structures for bio-inspired locomotion in order to determine the limitations of these structures for aerial-aquatic applications. Furthermore, an investigation into other honeycomb and kirigami structures may provide additional options outside of the ones used and modeled in this thesis. Fabian Wiesemüller will continue the work on self-sensing cellulose structures and will likely continue to extend the work on using diamond celled honeycombs for this application in camber morphing wings. Dr. Pham Huy Nguyen is a new postdoc in the lab who working on soft actuation and flexible structures for aerial-aquatic robots and may also continue some of this future work.

Bibliography

[1] R. Zufferey, "Aquatic Escape for Micro-Aerial Vehicles," Ph.D. Imperial College London, 2019.

[2] H. Alzu'bi, I. Mansour, and O. Rawashdeh, "Loon Copter: Implementation of a hybrid unmanned aquatic–aerial quadcopter with active buoyancy control," *Journal of Field Robotics*, vol. 35, no. 5, pp. 764–778, 2017, ISSN: 15564967. DOI: 10.1002/rob.21777.

[3] Y. H. Tan and B. M. Chen, "A Morphable Aerial-Aquatic Quadrotor with Coupled Symmetric Thrust Vectoring," in *Proceedings - IEEE International Conference on Robotics and Automation*, Institute of Electrical and Electronics Engineers Inc., May 2020, pp. 2223–2229, ISBN: 9781728173955. DOI: 10.1109/ICRA40945.2020.9196687.

[4] D. Mercado, M. Maia, and F. J. Diez, "Aerial-Underwater Systems, a New Paradigm in Unmanned Vehicles," *Journal of Intelligent and Robotic Systems: Theory and Applications*, vol. 95, no. 1, pp. 229–238, Jul. 2019, ISSN: 15730409. DOI: 10.1007/s10846-018-0820-x. [Online]. Available: https://doi.org/10.1007/s10846-018-0820-x.

[5] Y. Chen, H. Wang, E. Farrell Helbling, N. T. N. Jafferis, R. Zufferey, A. Ong, K. Ma, N. Gravish, P. Chirarattananon, M. Kovac, R. J. R. Wood, E. F. Helbling, N. T. N. Jafferis, R. Zufferey, A. Ong, K. Ma, N. Gravish, P. Chirarattananon, M. Kovac, and R. J. R. Wood, "A biologically inspired, flapping-wing, hybrid aerial-aquatic microrobot," *Science Robotics*, vol. 2, no. 11, pp. 1–12, 2017, ISSN: 2470-9476. DOI: 10.1126/scirobotics.aao5619. [Online]. Available: http://robotics.sciencemag.org/content/2/11/eaao5619%20http://robotics.sciencemag.org/.

[6] R. Siddall and M. Kovač, "Launching the AquaMAV: Bioinspired design for aerial-aquatic robotic platforms," *Bioinspiration and Biomimetics*, vol. 9, no. 3, p. 31 001, 2014, ISSN: 17483190. DOI: 10.1088/1748-3182/9/3/031001. [Online]. Available: http://iopscience.iop.org/1748-3190/9/3/031001.

[7] R. Zufferey, A. Ortega Ancel, A. Farinha, R. Siddall, S. F. Armanini, M. Nasr, R. V. Brahmal, G. Kennedy, and M. Kovac, "Consecutive aquatic jump-gliding with water-reactive fuel," *Science Robotics*, vol. 4, no. 34, p. 7330, Sep. 2019, ISSN: 24709476. DOI: 10.1126/scirobotics.aax7330. [Online]. Available: http://robotics.sciencemag.org/.

[8] R. Zufferey, A. O. Ancel, C. Raposo, S. F. Armanini, A. Farinha, R. Sidall, I. Berasaluce, H. Zhu, and M. Kovac, "SailMAV: Design and Implementation of a Novel Multi-Modal Flying Sailing Robo," *Robotics and Automation Letters*, vol. 3, no. 4, pp. 2894–2901, 2019. [Online]. Available: https://ieeexplore.ieee.org/stamp/stamp.jsp?tp=&arnumber=8733846.

[9] R. Siddall, G. Kennedy, and M. Kovac, "Explosive Propulsion Strategies for Aquatic Take off in Robotics," *2015 International Symposium on Robotics Research (ISRR)*, 2015.

[10] R. Zufferey, A. Ortega Ancel, C. Raposo, S. F. Armanini, A. Farinha, R. Siddall, I. Berasaluce, H. Zhu, and M. Kovac, "SailMAV: design and implementation of a novel multi-modal flying sailing robot," *IEEE Robotics and Automation Letters*, vol. 4, no. 3, pp. 1–1, 2019, ISSN: 23773766. DOI: 10.1109/lra.2019.2921507.

[11] R. Siddall and M. Kova£, "Launching the AquaMAV: Bioinspired design for aerial-aquatic robotic platforms," Tech. Rep.

[12] R. Zufferey, A. Ortega Ancel, A. Farinha, R. Siddall, S. F. Armanini, M. Nasr, R. V. Brahmal, G. Kennedy, and M. Kovac, "Consecutive aquatic jump-gliding with water-reactive fuel," *Science Robotics*, vol. 4, no. 34, p. 7330, Sep. 2019, ISSN: 24709476. DOI: 10.1126/scirobotics.aax7330. [Online]. Available: http://robotics.sciencemag.org/.

[13] O. T. Source, T. W. Journal, P. By, T. Wilson, and O. Society, "Windsurfing in Mute Swans (Cygnus olor) Author : Olle Terenius Windsurfing in Mute Swans (Cygnus olor)," vol. 128, no. 3, pp. 628–631, 2019.

[14] J. Yuan and S. K. Cho, "Bio-inspired micro/mini propulsion at air-water interface: A review †," *Journal of Mechanical Science and Technology*, vol. 26, no. 12, pp. 3761–3768, 2012. DOI: 10.1007/s12206-012-1002-6. [Online]. Available: www.springerlink.com/content/1738-494x.

[15] G. Iosilevskii and D. Weihs, "Hydrodynamics of sailing of the Portuguese man-of-war Physalia physalis," *Journal of the Royal Society Interface*, vol. 6, no. 36, pp. 613–626, 2009, ISSN: 17425662. DOI: 10.1098/rsif.2008.0457.

[16] M. Moreno, M. Parth, and S. F. Javier Diez-Garias, "Demonstration of an Aerial and Submersible Vehicle Capable of Flight and Underwater Navigation with Seamless Air-Water Transition," Tech. Rep.

[17] C. Munro, Z. Vue, R. R. Behringer, and C. W. Dunn, "Morphology and development of the Portuguese man of war, Physalia physalis," *Scientific Reports*, vol. 9, no. 1, pp. 10–20, 2019, ISSN: 20452322. DOI: 10.1038/s41598-019-51842-1.

[18] J. C. Gomez and E. Garcia, "Morphing unmanned aerial vehicles," *Smart Materials and Structures*, vol. 20, no. 10, 2011, ISSN: 09641726. DOI: 10.1088/0964-1726/20/10/103001.

[19] J. H. Fincham and M. I. Friswell, "Aerodynamic optimisation of a camber morphing aerofoil," *Aerospace Science and Technology*, vol. 43, pp. 245–255, Jun. 2015, ISSN: 1270-9638. DOI: 10.1016/J.AST.2015.02.023.

[20] L. J. Gibson, M. F. A. Sh, and J. G. S. Schajerj, "The mechanics of two-dimensional cellular materials," Tech. Rep., 1982, pp. 25–42.

[21] L. Gibson and M. Ashby, "The mechanics of honeycombs," in *Cellular Solids: Structure and Properties*, 2nd ed., Cambridge: Cambridge University Press, 1997, pp. 93–174. DOI: 10.1017/CBO9781139878326.006. [Online]. Available: https://doi.org/10.1017/CBO9781139878326.006.

[22] A. E. Rivero, S. Fournier, P. M. Weaver, J. E. Cooper, and B. K. S. Woods, "Manufacturing and characterisation of a composite FishBAC morphing wind tunnel model," *ICAST 2018: 29th International Conference on Adaptive Structures and Technologies*, no. October, pp. 1–14, 2018.

[23] S. Barbarino, O. Bilgen, R. M. Ajaj, M. I. Friswell, and D. J. Inman, "A Review of Morphing Aircraft," *Journal of Intelligent Material Systems and Structures*, vol. 22, no. 9, pp. 823–877, Jun. 2011, ISSN: 1045-389X. DOI: 10.1177/1045389X11414084. [Online]. Available: http://journals.sagepub.com/doi/10.1177/1045389X11414084%20http://jim.sagepub.com.

[24] M. Naghavi Zadeh, I. Dayyani, and M. Yasaee, "Fish Cells, a new zero Poisson's ratio metamaterial—Part I: Design and experiment," *Journal of Intelligent Material Systems and Structures*, vol. 31, no. 13, pp. 1617–1637, Aug. 2020, ISSN: 1045-389X. DOI: 10.1177/1045389X20930079. [Online]. Available: http://journals.sagepub.com/doi/10.1177/1045389X20930079.

[25] K. R. Olympio and F. Gandhi, "Zero Poisson's Ratio Cellular Honeycombs for Flex Skins Undergoing One-Dimensional Morphing," *Journal of Intelligent Material Systems and Structures*, vol. 21, no. 17, pp. 1737–1753, Nov. 2010, ISSN: 1045-389X. DOI: 10.1177/1045389X09355664. [Online]. Available: http://journals.sagepub.com/doi/10.1177/1045389X09355664.

[26] J. Rong and L. Zhou, "Study of a zero Poisson's ratio honeycomb used for flexible skin," *Materials Research Express*, vol. 4, no. 4, p. 045 701, Apr. 2017, ISSN: 20531591. DOI: 10.1088/2053-1591/aa6762. [Online]. Available: https://doi.org/10.1088/2053-1591/aa6762.

[27] L. Guiducci, K. Razghandi, L. Bertinetti, S. Turcaud, M. Rüggeberg, J. C. Weaver, P. Fratzl, I. Burgert, and J. W. Dunlop, "Honeycomb actuators inspired by the unfolding of ice plant seed capsules," *PLoS ONE*, vol. 11, no. 11, Nov. 2016, ISSN: 19326203. DOI: 10.1371/journal.pone.0163506. [Online]. Available: /pmc/articles/PMC5091791/?report=abstract%20https://www.ncbi.nlm.nih.gov/pmc/articles/PMC5091791/.

[28] L. Guiducci, P. Fratzl, Y. J. M. Bréchet, and J. W. C. Dunlop, "Pressurized honeycombs as soft-actuators: a theoretical study," *Journal of The Royal Society Interface*, vol. 11, no. 98, p. 20 140 458, Sep. 2014, ISSN: 1742-5689. DOI: 10.1098/rsif.2014.0458. [Online]. Available: https://royalsocietypublishing.org/doi/10.1098/rsif.2014.0458.

[29] S. Yang, I. S. Choi, and R. D. Kamien, "Design of super-conformable, foldable materials via fractal cuts and lattice kirigami," *MRS Bulletin*, vol. 41, no. 2, pp. 130–137, 2016, ISSN: 08837694. DOI: 10.1557/mrs.2016.5.

[30] L. Jing, Z. Wang, H. Wang, Y. Yang, L. Shen, W. Yin, E. Li, and H. Chen, "Kirigami metamaterials for reconfigurable toroidal circular dichroism," *NPG Asia Materials*, vol. 10, pp. 888–898, 2018. DOI: 10.1038/s41427-018-0082-x.

[31] J. Y. T. Designed Research; Y, J. Y. T. Performed Research; Y, and J. Y. Pnas |, "Programmable active kirigami metasheets with more freedom of actuation," vol. 116, no. 52, pp. 26 407–26 413, 2019. DOI: 10.1073/pnas.1906435116/-/DCSupplemental.

[32] G. P. Choi, L. H. Dudte, and L. Mahadevan, "Programming shape using kirigami tessellations," *Nature Materials*, vol. 18, no. 9, pp. 999–1004, 2019, ISSN: 14764660. DOI: 10.1038/s41563-019-0452-y. [Online]. Available: http://dx.doi.org/10.1038/s41563-019-0452-y.

[33] D.-G. Hwang and M. D. Bartlett, "Tunable Mechanical Metamaterials through Hybrid Kirigami Structures OPEN," vol. 8, p. 3378, 2018. DOI: 10.1038/s41598-018-21479-7. [Online]. Available: www.nature.com/scientificreports/.

[34] A. Rafsanjani, Y. Zhang, B. Liu, S. M. Rubinstein, and K. Bertoldi, "Kirigami skins make a simple soft actuator crawl," *Science Robotics*, vol. 3, no. 15, Feb. 2018, ISSN: 24709476. DOI: 10.1126/scirobotics.aar7555. [Online]. Available: http://robotics.sciencemag.org/.

[35] K. Xu, Y. Lu, S. Honda, T. Arie, S. Akita, and K. Takei, "Highly stable kirigami-structured stretchable strain sensors for perdurable wearable electronics," *Journal of Materials Chemistry C*, vol. 7, no. 31, pp. 9609–9617, 2019, ISSN: 20507526. DOI: 10.1039/c9tc01874c.

[36] R. Sun, B. Zhang, L. Yang, W. Zhang, I. Farrow, F. Scarpa, and J. Rossiter, "Kirigami stretchable strain sensors with enhanced piezoelectricity induced by topological electrodes," *Applied Physics Letters*, vol. 112, no. 25, p. 251 904, Jun. 2018, ISSN: 00036951. DOI: 10.1063/1.5025025. [Online]. Available: http://aip.scitation.org/doi/10.1063/1.5025025.

[37] F. Wiesemuller, C. Winston, A. Poulin, X. Aeby, A. Miriyev, T. Geiger, G. Nystr, and M. Kovac, "Self-sensing cellulose structures with design-controlled stiffness," *Robotics and Automation Letters*, 2021.

[38] S. Chen, J. Chen, X. Zhang, Z.-Y. Li, and J. Li, "Kirigami/origami: unfolding the new regime of advanced 3D microfabrication/nanofabrication with "folding".," *Light, science & applications*, vol. 9, no. 1, p. 75, Dec. 2020, ISSN: 2047-7538. DOI: 10.1038/s41377-020-0309-9. [Online]. Available: http://www.ncbi.nlm.nih.gov/pubmed/32377337%20http://www.pubmedcentral.nih.gov/articlerender.fcgi?artid=PMC7193558.

[39] A. Lamoureux, K. Lee, M. Shlian, S. R. Forrest, and M. Shtein, "Dynamic kirigami structures for integrated solar tracking," *Nature Communications*, vol. 6, p. 8092, Sep. 2015, ISSN: 20411723. DOI: 10.1038/ncomms9092.

[40] S. Sareh and J. Rossiter, "Kirigami artificial muscles with complex biologically inspired morphologies," *Smart Materials and Structures*, vol. 22, no. 1, p. 014 004, Jan. 2013, ISSN: 09641726. DOI: 10.1088/0964-1726/22/1/014004. [Online]. Available: https://iopscience.iop.org/article/10.1088/0964-1726/22/1/014004%20https://iopscience.iop.org/article/10.1088/0964-1726/22/1/014004/meta.

[41] M. Cartolano, B. Xia, A. Miriyev, and H. Lipson, "Conductive fabric heaters for heat-activated soft actuators," *Actuators*, vol. 8, no. 1, 2019, ISSN: 20760825. DOI: 10.3390/act8010009.

[42] A.-J. Wang and D. L. Mcdowell, "In-Plane Stiffness and Yield Strength of Periodic Metal Honeycombs," 2004. DOI: 10.1115/1.1646165. [Online]. Available: https://asmedigitalcollection.asme.org/materialstechnology/article-pdf/126/2/137/5880433/137_1.pdf.

[43] S. G. Fitzgerald, G. W. Delaney, and D. Howard, "A review of jamming actuation in soft robotics," *Actuators*, vol. 9, no. 4, pp. 1–31, 2020, ISSN: 20760825. DOI: 10.3390/act9040104.

[44] Y. S. Narang, J. J. Vlassak, R. D. Howe, Y. S. Narang, J. J. Vlassak, and R. D. Howe, "Mechanically Versatile Soft Machines through Laminar Jamming," 2018. DOI: 10.1002/adfm.201707136. [Online]. Available: https://doi.org/10.1002/adfm.201707136..

[45] Y. S. Narang, A. Degirmenci, J. J. Vlassak, and R. D. Howe, "Transforming the Dynamic Response of Robotic Structures and Systems Through Laminar Jamming," *IEEE ROBOTICS AND AUTOMATION LETTERS*, vol. 3, no. 2, 2018. DOI: 10.1109/LRA.2017.2779802. [Online]. Available: http://www.ieee.org/publications.

[46] J. Lee, C. Santiago, I. S. Godage, P. Gonthina, and I. D. Walker, "Soft Robots and Kangaroo Tails: Modulating Compliance in Continuum Structures Through Mechanical Layer Jamming," *Soft Robotics*, vol. 3, no. 2, pp. 54–63, 2016. DOI: 10.1089/soro.2015.0021. [Online]. Available: www.liebertpub.com.

[47] Y. Li, Y. Chen, Y. Yang, and Y. Wei, "Passive Particle Jamming and Its Stiffening of Soft Robotic Grippers," *IEEE Transactions on Robotics*, vol. 33, no. 2, pp. 446–455, 2017, ISSN: 15523098. DOI: 10.1109/TRO.2016.2636899.

[48] Y. Wei, Y. Chen, Y. Yang, and Y. Li, "A soft robotic spine with tunable stiffness based on integrated ball joint and particle jamming," *Mechatronics*, vol. 33, pp. 84–92, 2015. DOI: 10.1016/j.mechatronics.2015.11.008. [Online]. Available: http://dx.doi.org/10.1016/j.mechatronics.2015.11.008.

[49] M. J. Harrington, K. Razghandi, F. Ditsch, L. Guiducci, M. Rueggeberg, J. W. Dunlop, P. Fratzl, C. Neinhuis, and I. Burgert, "Origami-like unfolding of hydro-actuated ice plant seed capsules," *Nature Communications*, vol. 2, no. 1, pp. 1–7, Jun. 2011, ISSN: 20411723. DOI: 10.1038/ncomms1336. [Online]. Available: https://www.nature.com/articles/ncomms1336.

[50] D. G. Hwang and M. D. Bartlett, "Tunable Mechanical Metamaterials through Hybrid Kirigami Structures," *Scientific Reports*, vol. 8, no. 1, pp. 1–8, 2018, ISSN: 20452322. DOI: 10.1038/s41598-018-21479-7. [Online]. Available: http://dx.doi.org/10.1038/s41598-018-21479-7.

[51] F. Cote, "The compressive and shear responses of corrugated and diamond lattice materials," *Internationa Journal of Solids and Structures*, 2006.

[52] H. Hatami-Marbini and M. Rohanifar, "Stiffness of bi-modulus hexagonal and diamond honeycombs †," *Journal of Mechanical Science and Technology*, vol. 33, no. 4, pp. 1703–1709,

2019. DOI: 10.1007/s12206-019-0322-1. [Online]. Available: www.springerlink.com/content/1738-494x.

[53] A.-J. Wang, "In-plane stiffness and yield strength of periodic metal honeycombs," *Journal of Engineering Materials and Technology*, 2004.

[54] M. Ashby, "Material Selection - The Basics," in *Material Selection in Mechanical Design*, 4th ed., Cambridge: Elsevier, 2011, pp. 97–123. DOI: 10.1017/CBO9781139878326.006. [Online]. Available: https://doi.org/10.1017/CBO9781139878326.006.

[55] F. Cô Té, V. S. Deshpande, N. A. Fleck, and A. G. Evans, "The compressive and shear responses of corrugated and diamond lattice materials," 2005. DOI: 10.1016/j.ijsolstr.2005.07.045. [Online]. Available: www.elsevier.com/locate/ijsolstr.

[56] I. Sokolinkoff, *Mathematical Theory of Elasticity*, 2nd ed. New York: McGraw-Hill, 1956.

[57] A. A. F.A. McClintock, *Mechanical Behaviour of Materials*. Reading, Massachusetts: Addison Wesley, 1993.

[58] E. Ventsel and T. Krauthammer, *Thin Plates and Shells: Theory, Analysis, and Applications*. New York, NY: Marcel Dekker, Inc., 2001, ISBN: 0-8247-0575-0. [Online]. Available: http://www.dekker.com.

[59] G. Liu and S. Quek, "Chapter 2 - briefing on mechanics for solids and structures," in *The Finite Element Method (Second Edition)*, G. Liu and S. Quek, Eds., Second Edition, Oxford: Butterworth-Heinemann, 2014, pp. 13–41, ISBN: 978-0-08-098356-1. DOI: https://doi.org/10.1016/B978-0-08-098356-1.00002-3. [Online]. Available: https://www.sciencedirect.com/science/article/pii/B9780080983561000023.

[60] C. A. Lyon, A. P. Broeren, P. Giguere, A. Gopalarathnam, and M. S. Selig, *Summary of low-speed airfoil data, Vol. 3*. Department of Aeronautical and Astronautical Engineering University of Illinois at Urbana-Champaign Summary, 1998, vol. 3, p. 418, ISBN: 0964674726. [Online]. Available: http://hdl.handle.net/2060/19930092747.

[61] O. Terenius, " Windsurfing in Mute Swans (Cygnus olor)," *The Wilson Journal of Ornithology*, vol. 128, no. 3, pp. 628–631, 2016, ISSN: 1559-4491. DOI: 10.1676/1559-4491-128.3.628.

[62] "STUDY ON REINFORCED SOFT ACTUATOR FOR EXOSKELETON ACTUATORS by Mohammad Shuqir A Thesis Submitted to the Faculty of The College of Engineering and Computer Science In Partial Fulfillment of the Requirements for the Degree of Master of Science Florida Atla," no. August, 2018.

[63] N. El-Atab, R. B. Mishra, F. Al-Modaf, L. Joharji, A. A. Alsharif, H. Alamoudi, M. Diaz, N. Qaiser, and M. M. Hussain, "Soft Actuators for Soft Robotic Applications: A Review," 2020. DOI: 10.1002/aisy.202000128. [Online]. Available: https://doi.org/10.1002/aisy.202000128..

[64] J. Frame, "SELF-CONTAINED SOFT ROBOTIC JELLYFISH WITH WATER-FILLED BENDING ACTUATORS AND POSITIONAL FEEDBACK CONTROL by Jennifer Frame A Thesis Submitted to the Faculty of The College of Engineering and Computer Science In Partial Fulfillment of the Requirements for," Ph.D. dissertation, Florida Atlantic University, 2016.

[65] A. D. Marchese, R. K. Katzschmann, and D. Rus, "A recipe for soft fluidic elastomer robots," *Soft Robotics*, vol. 2, no. 1, pp. 7–25, Mar. 2015, ISSN: 21695172. DOI: 10.1089/soro.2014.0022. [Online]. Available: /pmc/articles/PMC4997626/?report=abstract%20https://www.ncbi.nlm.nih.gov/pmc/articles/PMC4997626/.

[66] B. Tondu, "Modelling of the McKibben artificial muscle: A review," *Article Journal of Intelligent Material Systems and Structures*, vol. 23, no. 3, pp. 225–253, DOI: 10.1177/1045389X11435435.

[67] E. T. Roche, R. Wohlfarth, J. T. B Overvelde, N. V. Vasilyev, F. A. Pigula, D. J. Mooney, K. Bertoldi, C. J. Walsh, E. T. Roche, J. T. Overvelde, D. J. Mooney, K. Bertoldi, C. J. Walsh, R. Wohlfarth, J. T. B Overvelde, N. V. Vasilyev, and F. A. Pigula, "A Bioinspired Soft Actuated Material," *Advanced Materials*, vol. 26, pp. 1200–1206, 2013. DOI: 10.1002/adma.201304018. [Online]. Available: www.advmat.de.

[68] L. Cappello, K. C. Galloway, S. Sanan, D. A. Wagner, R. Granberry, S. Engelhardt, F. L. Haufe, J. D. Peisner, and C. J. Walsh, "Exploiting Textile Mechanical Anisotropy for Fabric-Based Pneumatic Actuators," *SOFT ROBOTICS*, vol. 5, no. 5, 2018. DOI: 10.1089/soro.2017.0076. [Online]. Available: www.liebertpub.com.

[69] C. D. Onal, X. Chen, G. M. Whitesides, and D. Rus, "Soft mobile robots with on-board chemical pressure generation," *Inter- national Symposium on Robotics Research*, vol. 100, pp. 525–540, 2011, ISSN: 1610742X. DOI: 10.1007/978-3-319-29363-9{_}30.

[70] A. D. Marchese, C. D. Onal, and D. Rus, "Autonomous Soft Robotic Fish Capable of Escape Maneuvers Using Fluidic Elastomer Actuators," *Soft Robotics*, vol. 1, no. 1, pp. 75–87, 2014, ISSN: 21695172. DOI: 10.1089/soro.2013.0009.

[71] S. P. Babu, A. Sadeghi, A. Mondini, and B. Mazzolai, "Antagonistic pneumatic actuators with variable stiffness for soft robotic applications," *RoboSoft 2019 - 2019 IEEE International Conference on Soft Robotics*, pp. 283–288, 2019. DOI: 10.1109/ROBOSOFT.2019.8722803.

[72] J. Wang, Y. Fei, and W. Pang, "Design, Modeling, and Testing of a Soft Pneumatic Glove with Segmented PneuNets Bending Actuators," *IEEE/ASME Transactions on Mechatronics*, vol. 24, no. 3, pp. 990–1001, 2019, ISSN: 10834435. DOI: 10.1109/TMECH.2019.2911992.

[73] P. Polygerinos, Z. Wang, J. T. Overvelde, K. C. Galloway, R. J. Wood, K. Bertoldi, and C. J. Walsh, "Modeling of Soft Fiber-Reinforced Bending Actuators," *IEEE Transactions on RoboticsPolygerinos, Panagiotis*, vol. 31, no. 3, pp. 778–789, 2015, ISSN: 15523098. DOI: 10.1109/TRO.2015.2428504.

[74] A. D. Marchese, R. K. Katzschmann, and D. Rus, "A recipe for soft fluidic elastomer robots," *Soft Robotics*, vol. 2, no. 1, pp. 7–25, Mar. 2015, ISSN: 21695172. DOI: 10.1089/soro.2014.0022. [Online]. Available: /pmc/articles/PMC4997626/?report=abstract%20https://www.ncbi.nlm.nih.gov/pmc/articles/PMC4997626/.

[75] S. Seok, C. D. Onal, R. Wood, D. Rus, and S. Kim, "Peristaltic locomotion with antagonistic actuators in soft robotics," in *Proceedings - IEEE International Conference on Robotics and Automation*, 2010, pp. 1228–1233, ISBN: 9781424450381. DOI: 10.1109/ROBOT.2010.5509542.

[76] M. Cianchetti, A. Licofonte, M. Follador, F. Rogai, and C. Laschi, "Bioinspired Soft Actuation System Using Shape Memory Alloys," *Actuators*, vol. 3, pp. 226–244, 2014, ISSN: 2076-0825. DOI: 10.3390/act3030226. [Online]. Available: www.mdpi.com/journal/actuatorsArticle.

[77] T. Georges, V. Brailovski, E. Morellon, D. Coutu, and P. Terriault, "Design of Shape Memory Alloy Actuators for Morphing Laminar Wing With Flexible Extrados," 2009. DOI: 10.1115/1.3160310. [Online]. Available: https://asmedigitalcollection.asme.org/mechanicaldesign/article-pdf/131/9/091006/5630705/091006_1.pdf.

[78] Y. Dong, Z. Boming, and J. Liang, "A changeable aerofoil actuated by shape memory alloy springs," *Materials Science and Engineering A*, vol. 485, pp. 243–250, 2008. DOI: 10.1016/j.msea.2007.08.061.

[79] V. Brailovski, P. Terriault, T. Georges, and D. Coutu, "3rd International Symposium on Shape Memory Materials for Smart Systems SMA Actuators for Morphing Wings," *Physics Procedia*, no. 10, pp. 197–203, 2010. DOI: 10.1016/j.phpro.2010.11.098. [Online]. Available: www.sciencedirect.comwww.elsevier.com/locate/procedia.

[80] D. Debruyn, R. Zufferey, S. F. Armanini, C. Winston, A. Farinha, Y. Jin, and M. Kovac, "MEDUSA: A Multi-Environment Dual-Robot for Underwater Sample Acquisition," *IEEE Robotics and Automation Letters*, vol. 5, no. 3, pp. 4564–4571, Jun. 2020, ISSN: 2377-3766. DOI: 10.1109/lra.2020.3001534.

[81] J. E. Adkins and R. S. Rivlin, "Large elastic deformations of isotropic materials ix. the deformation of thin shells," *Philosophical Transactions of the Royal Society*, vol. 224, pp. 505–531, 1952.

[82] W. H. Yang and W. W. Feng, "On axisymmetrical deformations of nonlinear membranes," *ASME Journal of Applied Mechanics*, vol. 37, pp. 1002–1011, 1970.

[83] D. D. Washington, "Efficient methods for analyzing thin membranes subjected to transverse pressure and undergoing large deformation," Ph.D. dissertation, 2004.

[84] Y.-Y. Hsu, K. Lucas, D. Davis, B. Elolampi, R. Ghaffari, C. Rafferty, and K. Dowling, "Novel strain relief design for multilayer thin film stretchable interconnects," *IEEE Transactions on Electron Devices*, 2013.

Appendix A

Hyperelastic Materials in Aerial-Aquatic Robots

A.1 Motivation and Contributions

As discussed I will highlight in Section A.2.1, hyperelastic materials are incredibly common in soft robotics. They naturally exhibit strains that are much larger than those exhibited by their linear-elastic counterparts under the same stresses. This makes them naturally good candidates for robotic components that need to undergo large deformations because, when compared to stiffer, linear-elastic materials, hyperelastic materials can be actuated under much smaller forces. This dramatically decreases the amount of energy required to deform a portion of the robot, if that same portion were made from a linear-elastic material. Furthermore, the reduced stiffness of these materials also makes soft robots safer for humans to interact with because if the robot were to malfunction and collide with a human, it would be less likely to cause serious injury.

The goal of this appendix is a preliminary investigation into the degree to which the soft robotic actuation strategies discussed in Section A.2.1 are suitable for aerial-aquatic robots. I will do this by discussing two projects. Section A.3 will discuss an attempt to use both constraint enclosed and constraint embedded actuators in a camber morphing wing, and will draw some preliminary conclusions on the usefulness of these kinds of actuators for aerial-aquatic robots in general. In Section A.4, I then discuss my work modeling a hyperelastic membrane used for buoyancy control on an aerial-aquatic

robot, MEDUSA, which I helped develop along with several other members of my lab. From that work, I will reinforce some of the conclusions drawn in Section A.3 by demonstrating a hyperelastic actuator working on an aerial-aquatic robot.

The scientific and technical contributions of the work I will discuss in this appendix are:

- A preliminary evaluation of the feasibility and limitations of hyperelastic materials for aerial-aquatic robotic actuation
- Modeling of hyperelastic materials for an inflatable membrane used for buoyancy control

A.2 Hyperelastic Materials in Soft Robotics

The following section provides the necessary background information for Chapter A. This chapters discusses the use of hyperelastic materials for aerial-aquatic robots. SubSection A.2.1 presents a review of how hyperelastic materials are used in soft robotic actuators. This section also highlights the research gaps that Chapter A fills. Sub**??** provides background information on mechanics of hyperelastic materials which is necessary to understand the analysis in Chapter A.

A.2.1 A Review of Hyperelastic Materials In Soft Robotic Actuators

Actuators Built from Hyperelastic Materials

Many of the actuators used in soft robotics are made from hyperelastic materials [63]. These actuators are are typically pneumatic, hydraulic, or Shape Memory Alloy (SMA) driven elastomeric bodies used to produce linear, bending, and twisting motions [63, 65]. Here, I divide them into two classes: constraint enclosed actuatorsand constraint embedded actuators. In both of these classes, an elastomeric body is forced to change shape under internal loads caused by either fluid pressure or forces exerted by an SMA. Some type of constraint is designed into the actuator such that these internal loads cause the actuator to bend, extend, or contract. Constraint enclosed actuators consist of an elastomeric body that is then covered in some form of mesh or textile. This textile causes the actuator to undergo the desired deformation. In contrast, constraint embedded actuators are generally elastomer

molded structures that have various materials embedded in them. These embedded materials cause the desired shape change.

Constraint enclosed actuators

The McKibben Actuator is one of the oldest examples of a constraint enclosed actuator [66]. It consists of a long elastomeric bladder that is covered in a woven sheath. When the bladder is inflated, the actuator expands circumferentially and shortens in length [66]. McKibben actuators have been used in a variety of applications ranging from robotic arms, to heart inspired pumps [66, 67].

The knit textile bending actuator has a similar working principle to the McKibben actuator, but it produces a bending motion rather than a linear one. For this actuator, an elastic bladder is enclosed in a fabric sheath. That sheath consists of two different textiles: one isotropic woven textile, and another anisotropic knit textile. In it's most compliant direction, the knit textile is far less stiff than the woven textile. The two textiles are stitched together such that they are on opposite sides of the sheath. When the bladder is inflated, the actuator bends towards the woven textile side, as the knit textile stretches more under the same applied pressure due to its lower stiffness. This actuator has been primarily used in hand exoskeletons [68].

Constraint embedded actuators

The most common type of constraint embedded actuator is the Fluidic Elastomer Actuator (FEA) [65]. It consists of a silicone body with channels or voids that allow a driving fluid to be pumped into the body of the actuator. The shape and positioning of these voids or channels act as a constraint which influences the final geometry of the actuated FEA. In some cases, a strain limiting layer is placed opposite these channels and forces the actuator to bend. Actuators that employ this strain limiting layer have been used in robots that are almost entirely made from elastomers [69, 70]. FEAs have also been used as soft actuators in larger robotic systems containing both rigid and flexible portions. In this case, these FEAs are generally referred to as Pneunets. [44, 64, 71, 72]. In some cases, researchers have embedded fibers into the bodies of FEAs rather than using a strain limiting layer. These fibers constrain the actuator in such a way that they produce either bending or linear motion. These fiber-reinforced FEAs are typically used for the same types of tasks as Pneunets, but tend to be driven at higher pressures and are capable of producing larger forces [62, 71, 73, 74].

In some cases, SMAs are used instead of fluid pressure to move constraint embedded actuators. SMAs have been used as either springs or bending wires that move sections of the actuator. In this case, either strain limiting layers or fibers are used to produce the same sort of constraint seen in FEAs [74–76]. These actuators typically have a much smaller range of motion than FEAs. However, they have the advantage of being much smaller and lighter. Rather than using a pump to drive the actuator, one merely needs to heat the SMA by running a current through it in order to produce the desired motion. Consequently, these actuators have been used in a variety of morphing wings [77–79].

A.3 Hyperelastic Actuators for Aerial-Aquatic Morphing Wings

One of the few existing organisms that sails as its primary means of locomotion is the Portuguese Man-O-War Jellyfish (PMW). Above the water's surface, the PMW has a gas-filled body which provides positive buoyancy and a sail which helps control the animal's heading. Beneath the water's surface, the PMW has three different bodies which help the organism catch food, eat, reproduce, and move through the water [17]. It is believed that the PMW navigates the seas by controlling aerodynamic forces through adjusting the camber of its sail, and controlling hydrodynamic forces through movement of its tentacles [15]. Although morphologically different, this is very similar to the functioning of a sailboat. Instead of using tentacles, a sailboat uses a rudder and keel to control hydrodynamic forces and adjusts sail AoA, camber, or both.

As discussed in Chapter 4, the current SailMAV uses a rudder to control hydrodynamic forces and rotates its wings to control aerodynamic forces, which is fundamentally different from how the PMW sails. While there would be little added benefit to using tentacles instead of a rudder to control hydrodynamic forces, as a rudder is still needed for flight and these tentacles would create increased while in the air, there may be some benefit to using camber-morphing wings instead of wing rotation. It is already known that camber morphing wings allow for more energy efficient flight control as adjusting the wing's camber creates less drag than using hinged control surfaces. However, there is no obvious benefit for using camber-morphing in sailing rather than rotating the robot's wing, given that rotating each of these wings allows us to accurately redirect aerodynamic forces using the small amount of energy required to rotate a servo. This is an odd observation given that there are no animals

that sail by rotating an airfoil rather than adjusting its camber, which begs the question as to whether or not there are energetic or locomotion advantages to this sailing strategy that are not immediately obvious. Answering this question was a long-term research question that the lab is interested in answering, and one of the goals of my work was to provide flexible aerial-aquatic structures that could allow us to eventually attempt to sail using a camber morphing wing. Inspired by current actuation strategies in soft robotics and the PMW, I performed an initial investigation into inflatable morphing wings, as they would also allow for buoyancy control and were most morphologically similar to what is observed in the PMW.

As discussed in Chapter 2 most actuators used in soft robotics can be thought of as either being constraint embedded actuator or constraint enclosed actuator. As such, I will discuss two morphing wing designs that were inspired by these two classes of actuators in the subsequent sections. In those sections, I will briefly introduce each wing design concept, and will then describe the various manufacturing methods that I tried in the Methods subsections and discuss how well these prototypes performed in the Results and Discussion subsections.

A.3.1 Constraint Enclosed Morphing Wing

The wing concept described in this section can be best illustrated through the diagram in Fig. A.1. The flexible portion of the wing consists of a bidirectional knit textile bending actuator, like the ones described in Chapter 2. This bidirectional knit textile bending actuator would take on the shape of a symmetric airfoil when both sides are inflated equally, and then the camber of that airfoil would change based on a difference in inflation pressure between the two halves of the actuator. The pumps for inflating the wing would be contained within the structure of the robot, and the tubes connecting the wing to that pump would run through the rigid leading edge of the wing.

Methods

The main difference between the knit textile bending actuators that have currently been developed [68] and the one needed for this application is geometry. Existing knit textile bending actuators are tube shaped, and are manufactured using a rectangular template and a heat press or impulse sealer.

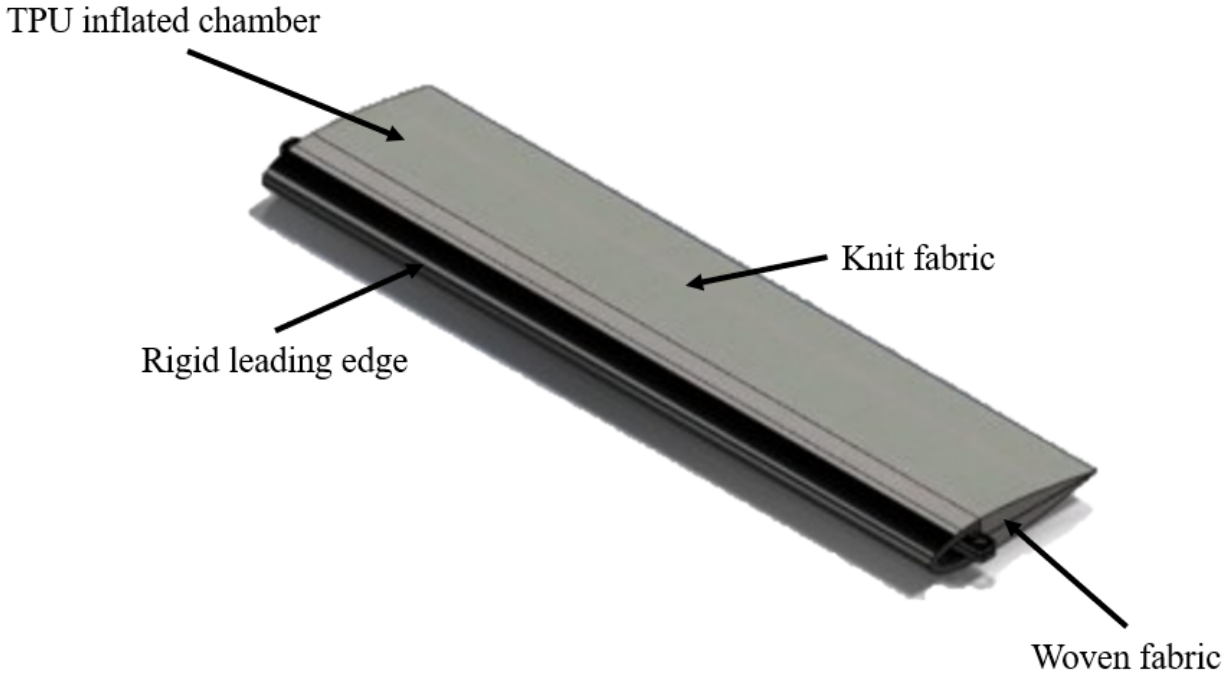

Figure A.1: constraint enclosed actuator based morphing wing concept.

In order to manufacture the actuator described in the previous section, I began taking TPU sheets and using a laser cutter to cut out pieces that could then be bonded together to form one of the inflatable chambers for the wing. An example of one of these cut-outs can be seen in Fig. A.2. This basic idea is similar to the method used to upholster complex shapes or sew together clothes. Each of the tabs at the edge of the cut out are intended to overlap, but rather than be sewn together, they are bonded to one another through the use of a heat gun. Any leaks were then sealed with PTFE thread tape. I then poked a hole in the TPU pouch, inserted a silicone tube which connected it to a pump, and then sealed that connection with PTFE and butyl tapes. I then sewed together a covering using a pattern very similar to the one shown in Fig. A.2. This covering consists of two pouches, the outside of these pouches is made from a 1-way knit textile and they are separated by a stiffer, woven textile.

Results and Discussion

The prototype discussed in the previous section showed some initial promise, as it was capable of bending in both directions. However, it was not possible to achieve curved seams, like the ones shown as curved red lines in Fig. A.2, which would have given it as specific airfoil shape. Consequently, the flexible portion of the wing looked more like a triangular prism than part of an airfoil.

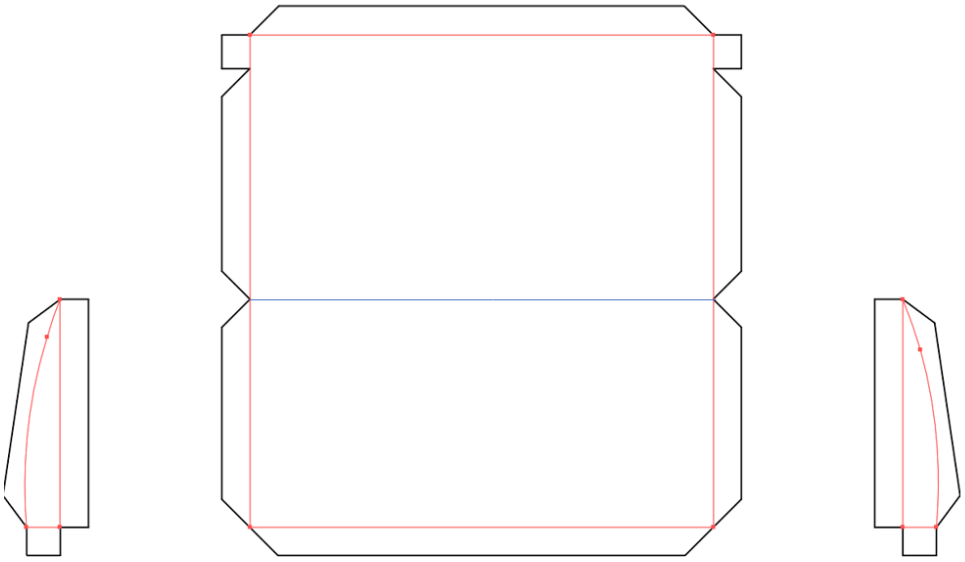

Figure A.2: Cut-out pattern for a knit textile bending actuator based morphing wing. The black lines are the pattern cut from the TPU sheet. The red lines delineate seams created by a heat gun which separate the airfoil shape from the tabs that are bonded together to form the seams.The blue line is a folded seam.

Furthermore, as the actuator bent in one direction, the opposite side wrinkled beneath it, which created an even less desirable airfoil shape. Given the manufacturing equipment available in the Aerial Robotics Laboratory Flight Arena and Student Workshop, I could not develop a new manufacturing method that could create these curved seams or mitigate this wrinkling affect. As a result, I decided to transition towards designing a constraint embedded actuator based morphing wing as I could mold the elastomeric body into a more precise shape.

A.3.2 Constraint Embedded Morphing Wing

The wing concept described in this section can be best illustrated through the diagram in Fig. A.3. The flexible portion of the wing consists of a FEA, like the ones described in Chapter 2. This bidirectional knit textile bending actuator would take on the shape of a symmetric airfoil when both sides are inflated equally, and then the camber of that airfoil would change based on a difference in inflation pressure between the two halves of the actuator. Like in the previous design, the pumps for inflating the wing would be contained within the structure of the robot, and the tubes connecting the wing to that pump would run through the rigid leading edge of the wing. The trailing edge of this wing is

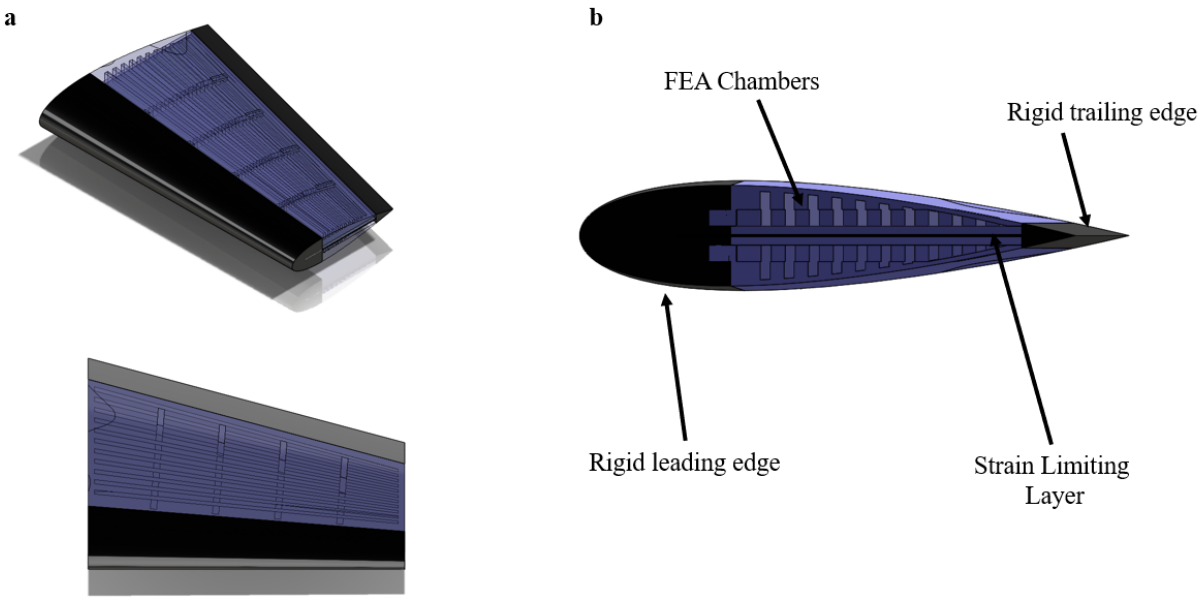

Figure A.3: constraint embedded actuator based morphing wing concept. **a)** 3/4 and side views of the entire wing. **b)** A cross-section of the wing with labeled sections

rigid so that it is less likely to tear or deteriorate with use as a thin layer of silicone would.

Methods

I manufactured this wing using a technique very similar to the one outlined in this paper [74]. The body of the wing was made from two FEAs made from Ecoflex 00-30 silicone. A mold was 3D printed RGD450 using a Stratasys Connex 350 with a matte finish. The mold was then power washed and soaked in an IPA bath for 6 hrs because the silicone would not fully cure if it came into contact with any of the support material or any RGD450 components printed with a glossy finish. The silicone was first measured, mixed, and then left in a vacuum chamber for 10 min at 90 KPa to remove most of the bubbles. The tubes connecting each half of the wing to the pump and the strain limiting layer (a piece of paper in this initial prototype) were then inserted into the mold. The silicone was then poured into the mold around the tubes and strain limiting layer. The silicone was then allowed to cure for 4 hrs.

Results and Discussion

This prototype was capable of demonstrating bi-directional camber morphing while maintaining a much more desirable airfoil shape. However, the precise shapes and aerodynamic performance of this wing were not investigated because the first working prototype was far too heavy to ever be used in a flying robot. Initially, the entire structure was intended to be made from layers of silicone that were $0.5mm$ thick so that the entire wing would be comparable in weight to the ones on the current SailMAV. However, it was not possible to get thin layers of constant thickness with the manufacturing method discussed in the previous section because tiny air bubbles would still get trapped within the silicone. I attempted to mitigate this by allowing the wing to cure within the vacuum chamber, but as the bubbles escaped the mold lots of silicone often came with it and I was only able to produce a partial wing. With that partial wing, I also found that when pressure was applied, the wing would deflect by less than 3% of the chord before popping. Furthermore, even if that were sufficient deflection, such a wing would be unlikely to survive outdoor conditions for very long without soon developing a leak. Consequently, a prototype with thicker walls was developed and prototyped to demonstrate the feasibility of the concept, but as this wing was 4× heavier than the current SailMAV wings, this concept was abandoned in favor of the wing described in Chapter 4

A.3.3 Conclusion

Ultimately, this investigation into constraint enclosed actuator and constraint embedded actuator based morphing wings did not yield any prototypes that could be used in an aerial-aquatic robot. This is because I was unable to produce a constraint embedded actuator based morphing wing using the manufacturing methods currently used to create knit textile bending actuators and the manufacturing equipment available to me. Furthermore, while the FEA based morphing wing was capable of maintaining an airfoil shape, it required far too much silicone to do so without popping. This increased the weight of the structure to the point where it could possibly function as a camber morphing sail, but it was far too heavy to also be used for flight. However, it is worth noting that there may be other designs, which I did not have the opportunity to test that may have been able to make better use of these hyper-elastic materials. One example of this would be a TPU bag with inflatable

pockets along its chord that allowed the wing to change camber when pressurized. Such a wing could potentially be manufactured entirely through laser cutting, as the TPU pockets could together rather than cut all the way through by changing settings on the laser cutter. Unfortunately, due to closure of manufacturing facilities during COVID-19, this was never implemented.

Based on this investigation, I concluded that building soft actuators made from hyperelastic materials which are intended to take on complex shapes and/ or encompass large portions of the robot are incredibly difficult to achieve for aerial-aquatic robots given the existing manufacturing methods for these kinds of actuators. The constraint embedded actuator morphing wing did show lots of promise for applications where the shape of the actuator is not as critical, as the entire structure was fairly lightweight. However, forming precise and complex shapes from TPU sheets is certainly an area of manufacturing research that needs further exploration. Furthermore, the constraint embedded actuator wing, did demonstrate much more precise shape control, but it was far too heavy to be used as a large portion of any flying robot. This type of actuator could, however, be used as a much smaller portion of an aerial-aquatic robot, where it could be treated more like a small payload that the robot must carry rather than a large part of the robot's structure.

These conclusions are ultimately what led me to pursue the morphing wing design discussed in Chapter 4 rather than continuing to investigate morphing wings made from hyperelastic materials. However, Section A.4 will demonstrate a successful implementation of hyperelastic materials in an aerial-aquatic robot by showing the modeling and performance of a silicone-based inflatable membrane used for buoyancy control.

A.4 MEDUSA: A Demonstration of Hyperelastic Materials in Aerial-Aquatic Robots

MEDUSA, a Multi-Environment Dual-Robot for Underwater Sample Acquisition, is a symbiotic aerial-aquatic robotic system consisting of two robots. These two robots work in tandem to complete a single aerial-aquatic mission, similar to how various animals form symbiotic relationships to complete tasks in the natural world. An image of this system can be seen in Fig. A.4. The system con-

sists of a quadrotor which manages the aerial portion of the mission by flying to and from an aquatic location. That quadrotor also carries a submerisble, which is deployed beneath the water's surface and records video footage as it moves underwater. This mission profile is is outlined in Fig. A.4. This entire system was built by Diego Debruyn, with significant help from Raphael Zufferey, Andre Farinha, and Sophie Armanini. My primary contribution to this project was in the modeling of a hyperelastic membrane used for depth control on the submersible pod, so that work is what I will discuss in this chapter. That membrane is an example of successful application of a hyperelastic material in an aerial-aquatic robot, so I discuss it here as it informs the conclusions I draw at the end of this chapter about uses of hyperelastic materials in aerial-aquatic robots as a whole. For more details on this project, please see our publication [80] and video.

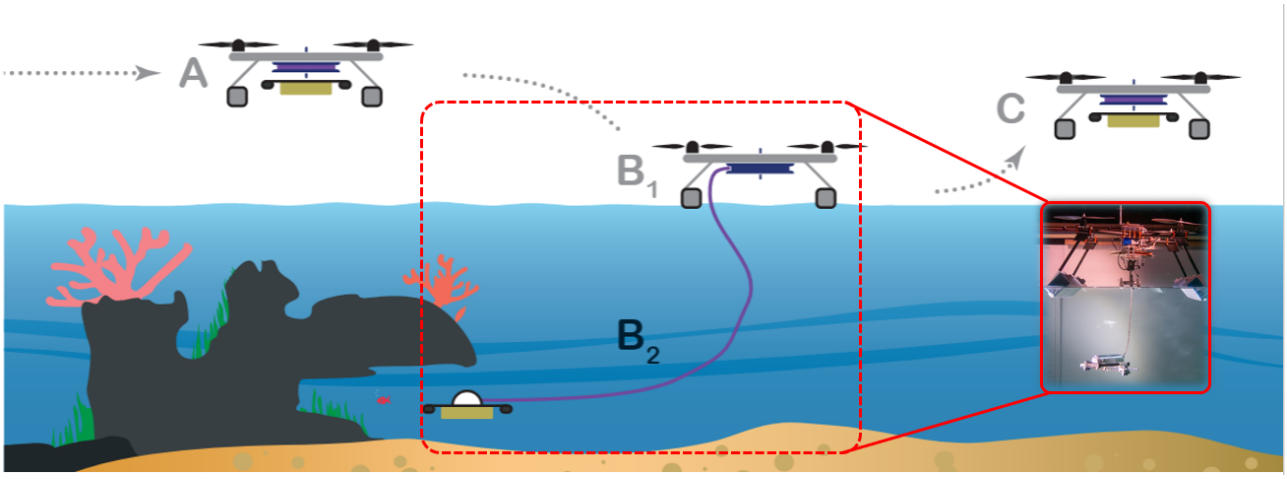

Figure A.4: Schematic of the operation principle of the dual system adapted from [80]. **A.** The quadrotor carries the submersible pod (yellow) to an aquatic location. **B1.** The quadrotor lands and floats on the water's surface. **B2.** The coiling mechanism (blue) releases a tether and the submersible pod moves vertically, through buoyancy control, and horizontally, using its jets, to reach the target underwater location. Live video is transmitted. A real image of the robot in this state is boxed in red. **C.** The tether is coiled again and the drone flies back to the user.

A.4.1 Modeling of Hyperelastic Membrane

The submersible pod, shown in Fig. A.4, controls its depth through the inflation of a hyperelastic membrane. This method of depth control is inspired by fish, who generally control their depth by inflating or deflating a soft bladder inside their body, thus changing their buoyancy.

In order to understand the behaviour of the membrane on MEDUSA, I modelled it as a thin, hyperelas-

tic, incompressible shell using the formulation developed by Adkins and Rivlin [81]. The membrane is described using a cylindrical coordinate system (R, Θ, Z), where each particle on the surface of the membrane exists at a point (r, θ, η). The stretch ratios in the meridional and circumferential directions are λ_1 and λ_2, respectively.

$$\lambda_1 = \sqrt{\frac{\left(\frac{\partial r}{dr}\right)^2 + \left(\frac{\partial \eta}{\partial r}\right)^2}{1 + \left(\frac{\partial Z}{\partial r}\right)^2}} \tag{A.1}$$

$$\lambda_2 = \frac{r}{R} \tag{A.2}$$

The equilibrium equations of the deformed membrane yield

$$\frac{\partial T_1}{\partial r} + \frac{1}{r}(T_1 - T_2) = P_t \tag{A.3}$$

$$K_1 T_1 + K_2 T_2 = P_n \tag{A.4}$$

where T_1 and T_2 represent the meridional and circumferential stress resultants, K_1 and K_2 represent the principal curvatures, P_n represents the stresses normal to the membrane surface and P_t represents pressure in the transverse direction. For this problem $P_t = 0$. Finally, using the Mooney-Rivlin constitutive relation given by **??** and the stress-strain relationship given by **??**, I get

$$T_1 = 2C_1 h \left(\frac{\lambda_1}{\lambda_2} - \frac{1}{\lambda_1^3 \lambda_2^3}\right)(1 + \alpha \lambda_2^2) \tag{A.5}$$

$$T_2 = 2C_1 h \left(\frac{\lambda_2}{\lambda_1} - \frac{1}{\lambda_1^3 \lambda_2^3}\right)(1 + \alpha \lambda_1^2) \tag{A.6}$$

where C_1 and α are constants that come from the constitutive relationship.

The above equations were simplified into three first-order Ordinary Differential Equations (ODEs) using the method described by Yang and Feng [82] and then solved using a Runge-Kutta algorithm, implemented as in [83].

Solving these ODEs yields the height of the inflated membrane, which can then be used to calculate

the volume using equation Eq. (A.7). This equation assumes the membrane takes on the shape of a spherical cap. The base width of the cap is $2a$ and maximum height is h.

$$V = \frac{1}{6}\pi h(3a^2 + h^2). \tag{A.7}$$

A.4.2 Results and Discussion

In order to validate the model described in Section A.4.1, Diego Debruyn inflated the membrane under different pressures, and measured the height of the membrane at those pressures. This was recorded on video, and the height of the membrane was measured in video editing software by Raphael Zufferey. Using, equation Eq. (A.7), I then converted that membrane height into a volume and produced the plot shown in Fig. A.5 using the model discussed in Section A.4.1.

The values used to describe the geometry of the membrane and the corresponding material constants that came from fitting the model to the data are given in table Table A.1. The material properties, C_1 and α, could not be found for our particular material (Ecoflex 00-20), so values for a similar material were chosen as a starting point, and they were then adjusted to fit our data [84].

Table A.1: Model parameter values.

$C_1[MPa]$	α	Membrane Thickness [mm]	a [mm]
0.0039	0.1	1.1	20

A.4.3 Conclusion

As discussed in Section A.3, I was unable to build morphing wings using the manufacturing techniques already established for knit textile bending actuators and FEAs. From this, I concluded that knit textile bending actuator could be used for aerial-aquatic robots, but not in applications where they need to take on a specific aerodynamic shape. I also concluded that, FEAs, could be used in aerial-aquatic robots, but only as small payloads because silicone is too dense to be used for large aerial-aquatic structures.

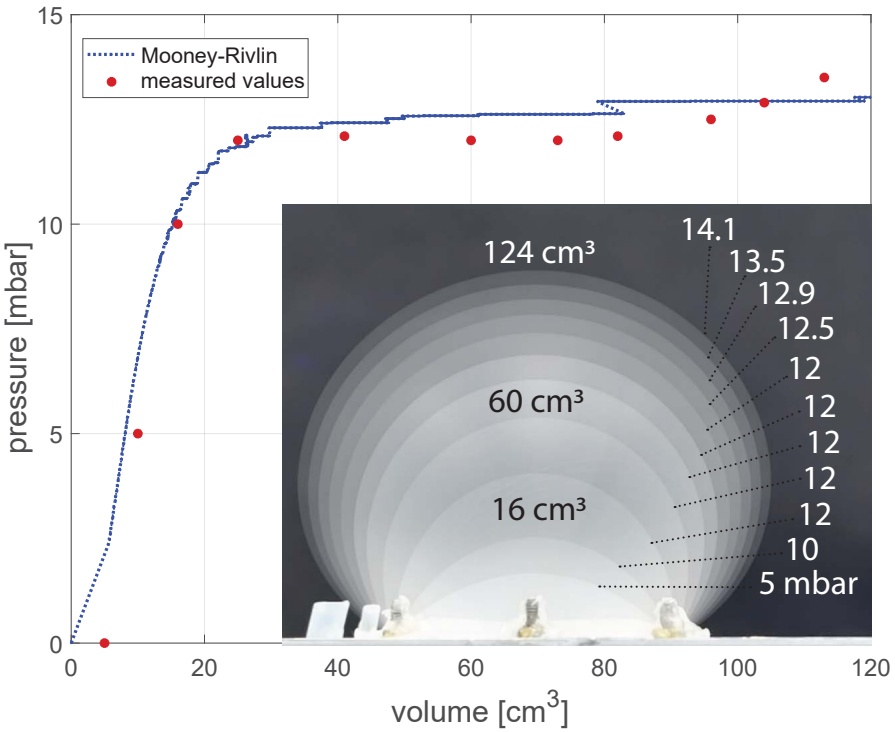

Figure A.5: Membrane volume versus pressure: model-predicted and tracking data-reconstructed results taken from [80] ©2020 IEEE.

The hyperelastic membrane used in MEDUSA serves to further reinforce that last conclusion. In this particular case, the hyperelastic membrane is a small FEA, with a very simple geometry that was successfully used to control the depth of a submersible pod. Because the membrane is very small relative to the size of the entire robot, the use of a hyperelastic material for a bio-inspired aerial-aquatic structure is feasible because it can be treated as a payload that MEDUSA can carry. These kinds of simple FEAs could be utilized for buoyancy modulation on a wide variety of aerial-aquatic robots and can be modeled as shown in Section A.4.1.

Appendix B

Permission to Reproduce Content

B.1 Permission to Reproduce Content from Robotics and Automation Letters

Chapter 3, Chapter 4, and Chapter A all have some figures that have either been adapted or reproduced from my publications in the Robotics and Automation Letters. This has been done in accordance with their copyright policies as follows:

> The IEEE does not require individuals working on a thesis to obtain a formal reuse license, however, you must follow the requirements listed below: Textual Material Using short quotes or referring to the work within these papers) users must give full credit to the original source (author, paper, publication) followed by the IEEE copyright line © 2011 IEEE. In the case of illustrations or tabular material, we require that the copyright line © [Year of original publication] IEEE appear prominently with each reprinted figure and/or table. If a substantial portion of the original paper is to be used, and if you are not the senior author, also obtain the senior author's approval. Full-Text Article If you are using the entire IEEE copyright owned article, the following IEEE copyright/ credit notice should be placed prominently in the references: © [year of original publication] IEEE. Reprinted, with permission, from [author names, paper title, IEEE publication title, and month/year of publication] Only the accepted version of an IEEE copyrighted paper

can be used when posting the paper or your thesis on-line. In placing the thesis on the author's university website, please display the following message in a prominent place on the website: In reference to IEEE copyrighted material which is used with permission in this thesis, the IEEE does not endorse any of [university/educational entity's name goes here]'s products or services. Internal or personal use of this material is permitted. If interested in reprinting/republishing IEEE copyrighted material for advertising or promotional purposes or for creating new collective works for resale or redistribution, please go to `http://www.ieee.org/publications_standards/publications/rights/rights_link.html` to learn how to obtain a License from RightsLink. If applicable, University Microfilms and/or ProQuest Library, or the Archives of Canada may supply single copies of the dissertation.

B.2 Permission to Reproduce Content from Nature Communications

Chapter 3, has a figure which uses images from a publication in Springer Nature. I have followed their process in order to get permission to reuse this image, and that process is detailed below:

Springer Nature is partnered with the Copyright Clearance Center to meet our customers' licensing and permissions needs.

Copyright Clearance Center's RightsLink® service makes it faster and easier to secure permission for the reuse of Springer Nature content.

Simply visit SpringerLink or www.nature.com and locate the desired content; Once you have opened the article or book chapter click on the "Rights and Permissions" button. This can either be found under the article title, at the bottom of the page or in the tools menu.

1. Select the way you would like to reuse the content
2. Create an account if you haven't already

3. Accept the terms and conditions and you're done!

For questions about using the RightsLink service, please contact Customer Support at Copyright Clearance Center via phone +1-855-239-3415 or +1-978-646-2777 or email customercare@copyright.com.